

[Insert NESC Document Number
NESC logo inserted *after* NRB approval]

NASA Engineering and Safety Center Technical Assessment Report

Lunar Meteoroid Ejecta Model Review

Include NRB presentation date

Restricted distribution to NESC and designated team members until approved by the NRB.

Report Approval and Revision History

| | | |
|-----------|---------------|------|
| Approved: | NESC Director | Date |
|-----------|---------------|------|

| Version | Description of Revision | Office of Primary Responsibility | Effective Date |
|---------|-------------------------|----------------------------------|-----------------------------|
| 1.0 | Initial Release | Joe Minow | NRB Presentation Date |

Restricted distribution to NESC and designated team members until approved by the NRB.

Table of Contents

Technical Assessment Report

| | | |
|-------------|---|------------------------------|
| 1.0 | Notification and Authorization..... | 9 |
| 2.0 | Signature Page..... | 10 |
| 3.0 | Team List..... | 11 |
| 3.1 | Acknowledgments | 11 |
| 4.0 | Executive Summary..... | 12 |
| 5.0 | Introduction and Assessment Plan..... | 13 |
| 6.0 | Problem Description..... | 13 |
| 6.1 | Prior Work | 13 |
| 6.2 | Summary of MeMoSeE model | 16 |
| 6.2.1 | Input models | 16 |
| 6.2.2 | Cratering relations | 17 |
| 6.2.3 | Assumptions | Error! Bookmark not defined. |
| 6.2.4 | Model name and acronym | Error! Bookmark not defined. |
| 6.3 | Model use..... | 19 |
| 6.3.1 | DSNE inputs | 21 |
| 6.3.2 | Bumper integration..... | Error! Bookmark not defined. |
| 7.0 | Section 1 - Primary impact flux..... | 21 |
| 7.1 | Meteoroids | 22 |
| 7.2 | Near-Earth objects | 22 |
| 7.2.1 | Flux | 22 |
| 7.2.2 | Speed distribution..... | 23 |
| 7.2.3 | Directionality of larger objects | 23 |
| 8.0 | Section 2 - Ejection process..... | 25 |
| 8.1 | LADEE Comparison..... | 25 |
| 8.1.1 | Size distribution..... | 25 |
| 8.1.2 | Ejecta Yield | 26 |
| 8.1.3 | Angular distribution..... | 27 |
| 8.1.4 | Velocity Distribution | 28 |
| 8.1.5 | Ejected mass | 29 |
| 8.2 | LROC Comparison | 25 |
| 9.0 | Section 3 – Propagation of the ejecta to the asset..... | 36 |
| 9.1 | Monte Carlo approach | 36 |
| 9.2 | Stochastic Behavior of Primaries..... | 43 |
| 10.0 | 5. Risk Model Sensitivity | 46 |
| 10.1 | Variability in Time and Space | 46 |
| 10.2 | Relative Contribution of Large versus Small Impactors to the Ejecta Flux | 47 |
| 10.3 | Sporadic Versus Shower Meteoroid Contribution to the Ejecta Flux..... | 51 |
| 10.4 | Effect of Depth of Excavation on the Soil Size Distribution Ejected from the Crater | 52 |
| 10.4.1 | Lunar regolith size distribution..... | 53 |
| 10.4.2 | Effect of lunar regolith size distribution on the ejecta flux | 55 |
| 10.4.3 | Crater dimension scaling | 56 |
| 10.4.4 | Contribution to the ejecta flux from impacts excavating to depths larger than 10-m.. | 58 |
| 10.5 | Ejecta Impact Risk Versus Sporadic Meteoroid Impact Risk..... | 63 |
| 10.5.1 | Overview of prior results and consequences for MeMoSeE | 64 |
| 10.5.2 | Application of MeMoSeE to the HLS Sortie Mission..... | 66 |
| 10.5.3 | The Lunar Ejecta Penetration Risk and the HLS at the Artemis Base Camp | 74 |
| 10.5.4 | The xEMU Lunar Ejecta Penetration Risk | 74 |

Restricted distribution to NESC and designated team members until approved by the NRB.

| | | |
|-------------|---|-----------|
| 10.6 | Number of MeMoSeE Speed Bins Required for Converged Calculations of Mean Number of Failures | 74 |
| 11.0 | Findings, Observations, and NESC Recommendations..... | 78 |
| 11.1 | Findings | 78 |
| 11.2 | Observations | 81 |
| 11.3 | NESC Recommendations | 81 |
| 12.0 | Alternative Viewpoint(s) | 83 |
| 13.0 | Other Deliverables | 83 |
| 14.0 | Lessons Learned..... | 83 |
| 15.0 | Recommendations for NASA Standards and Specifications..... | 83 |
| 16.0 | Definition of Terms..... | 83 |
| 17.0 | Acronyms and Nomenclature | 84 |
| 18.0 | References..... | 85 |

Restricted distribution to NESC and designated team members until approved by the NRB.

List of Figures

| | | |
|---|-------------------------------------|-------------------------------------|
| Figure | | Error! Bookmark not defined. |
| Figure 1 - Zenith angle distribution of NEAs impacting the lunar surface for three locations: a point near the lunar equator (top left), a point near 45° S (top right), and a point near the lunar south pole (bottom left). In each case, we compare the NEA zenith angle distribution with that of the high-density and low-density populations from the Meteoroid Engineering Model (MEM). At bottom right, we compare the speed distribution of NEAs impacting the lunar surface, averaged over all locations, with that derived from CNEOS data (Moorhead 2020b). The NEA-MEM speed distribution appears faster than that derived from the CNEOS data; this may be due to detection biases..... | 24 | |
| Figure 2 - Directionality of NEAs relative to an object orbiting the Sun at 1 au, modeled using the framework of the Meteoroid Engineering Model (MEM). Angular coordinates are in a Sun-centered ecliptic frame, in which the center of the plot (270°, 0°) points in the direction of the reference object's orbital motion (i.e., "ram")..... | 24 | |
| Report Figure 1. Slope of the charge and mass distributions. The exponent of the power-law distributions fitted to LDEX measurements as functions of altitude (15 km bins) and time (10 day bins). The color indicates the value of the differential mass distribution index ($1+\alpha$), and the size of a circle is inversely proportional to its absolute uncertainty. The inset shows the impact charge distribution for all heights for the entire mission, resulting in a χ^2 minimizing fit of $\alpha = 0.910 \pm 0.003$. From Horanyi et al. (2015)...... | Error! Bookmark not defined. | |
| Report Figure 2. Left: Assumed plume parameters for simulation to compare to LADEE/LDEX plume observations. Right: Histogram of fitted outer plume angles. Plumes with outer angle $8^\circ \pm 3^\circ$ were consistent with LADEE/LDEX observations. From Bernardoni et al. (2019)...... | Error! Bookmark not defined. | |
| Report Figure 3. Left. The dust density distribution about the Moon, calculated using $\sim 140,000$ impacts averaged over LADEE's 6 months of operations in lunar orbit. White regions indicate locations either LADEE did not visit or that LDEX could not take measurements due to sun pointing constraints. Altitude bands are not to scale. Right. The inferred surface ejecta velocity distribution from the altitude density fit. The dotted line indicates the maximum altitude explored by LADEE, above which the distribution function is an extrapolation. From Szalay et al. (2018)..... | Error! Bookmark not defined. | |
| Report Figure 4. (a) Ejecta density n_0 at the surface in a Mollweide projection for the various sources individually (above) and combined (below) in a "windshield" view looking from the center of the Moon outward. Latitude/longitude lines are shown every 30°. (b) Total upgoing ejecta flux as a function of LT over all latitudes. The inset shows polar stereographic projection of n_0 in the northern hemisphere, also in the same windshield view as (a), but with a viewpoint looking north. HE = helion; AH = antihelion; AP = apex; NT = northern toroidal; ST = southern toroidal. From Szalay et al. (2019)..... | Error! Bookmark not defined. | |
| Figure 1: (a) Temporal ratio (after M1129645568L/before M183689789L) blue outline shows outer extent of DLRZ, red line delimits outer boundary of DHRZ, orange polygon defines the outer limit of the PLRZ, the PHRZ extends from the crater rim out to the green boundary. (b) Enlargement of top panel centered on the 17 March crater. The actual boundaries between zones are not as sharp as the lines imply, north is up in both panels. From Robinson et al. (2015)...... | 32 | |
| Figure 2: Secondary splotches (highlighted with white arrows) observed in temporal ratio images (After image/before image; M1129645568/M183689789) around the 17 March 2013 | | |

Restricted distribution to NESC and designated team members until approved by the NRB.

| | |
|---|----|
| impact site. The black arrow points back to the primart crater seen in Figure 1. Each panel is 198 m wide. From Robinson et al. (2015)..... | 33 |
| Figure 3: a, Temporal ratio image showing rays of a DHRZ from a 19.5-m crater (ratio of NAC frames M1132496422R/M1101866147R). b, Temporal ratio image displaying a DLRZ extending 150D from a 12-m impact crater (ratio of NAC frames M1105837846R/M1121160416R). c, Temporal ratio image showing the distinct boundary between the two proximal and distal zones around an 11-m crater (ratio of NAC frames M1113630818R/M1098309025L). The red dots in a–c mark the location of the crater. d, Enlarged version of b showing ‘shadows’ in the DLRZ caused by a small crater. e, NAC frame M1132496422R highlighting the DLRZ shadow shown in d with an arrow pointing to parent impact. f, WAC temporal ratio image created with hundred of before and after images showing a DLRZ extending 100 km away from a newly formed 70 m crater. Adapted from Speyerer et al. (2016). | 34 |
| Figure 3-1 – for the Monte Carlo flux calculations, a virtual sphere of known radius is placed on the surface of the Moon. Flux is computed from the number of ejecta that penetrate the sphere..... | 37 |
| Figure 3-2 – There are two general cases of objects that hit the sphere. Case A is from a primary impact some distance away, where the particle has passed apoapsis and is started to descend, and has an impact zenith angle γ between 0° and 90° . Case B is from a primary impact nearby, and the particle is still ascending when it hits the sphere. Its impact zenith angle γ will be between 90° and 180° | 37 |
| Figure 3-3 – The distribution in zenith angle of simulated ejecta hitting the 500 m sphere using the Case A direction distribution looks similar to an isotropic distribution (from a total of 2×10^{11} total ejecta particles created). Note that a significant number – roughly half - of impacts hit the sphere with zenith angles $>90^\circ$, indicating they hit while “ascending” from the lunar surface..... | 39 |
| Figure 3-4 – A scatter plot of the relationship of the zenith angle to the range shows that most of the impacts “from above” with zenith angles $<90^\circ$ come from distant impacts (a few from the antipode of the Moon or that complete more than half a revolution before hitting the 500 m sphere). The majority of the “ascending” case with zenith angles $>90^\circ$ come from nearby – within a few km, and a significant number from from “beneath” the sphere..... | 40 |
| Figure 3-5 – The normalized cumulative distribution of the distance to the primary impact location shows that ~15% of the total ejecta striking the sphere originate from primary impacts “beneath” the sphere, and ~70% originate from within a 10 km radius. Of the population that strike the target sphere “from below”, virtually all are from primary impacts very close to the target sphere (the simulation shows <10 km, but that precise distance is probably a function of the size of the 500 m radius sphere). Of the population that strike the target sphere “from above”, 40% come from the near field (< 10 km), and most ($>85\%$) are from distances within 100 km. Only a small fraction come from distant parts of the Moon..... | 40 |
| Figure 3-6 – The distribution in zenith angle of simulated ejecta hitting the 500 m sphere using the Case B60 direction distribution shows similar “above/below” symmetry as in Case A... | 41 |
| Figure 3-7 – The distribution in zenith angle of simulated ejecta hitting the 500 m sphere using the Case B45 direction distribution shows similar “above/below” symmetry as in Case A and Case B60..... | 42 |
| Figure 3-8 – The range in possible flux values for N random impacts over the surface of the Moon chosen from the Poisson expectation value of 10.0. Most of the cases have fluxes lower than the average, but about 3% of the cases have primary impacts near the asset, | |

Restricted distribution to NESC and designated team members until approved by the NRB.

| | |
|--|----|
| and have higher-than-average flux, in some cases higher than average by several orders of magnitude. | 44 |
| Figure 3-9 – The range in possible flux values for N random impacts over the surface of the Moon chosen from the Poisson expectation value of 100.0. Most of the cases have fluxes lower than the average, but about 6% of the cases have primary impacts near the asset, and have higher-than-average flux, in some cases higher than average by several orders of magnitude. | 45 |
| Figure 3-10 – The range in possible flux values for N random impacts over the surface of the Moon chosen from the Poisson expectation value of 1000.0. Most of the cases have fluxes lower than the average, but about 10% of the cases have primary impacts near the asset, and have higher-than-average flux, in some cases higher than average by several orders of magnitude. | 46 |
| Figure 1 – The flux of particles of a given mass or larger onto the Moon, as a function of that limiting mass. The solid blue curve presents the meteoroid flux obtained using MEM, while the dashed orange curve is the NEO flux derived from Brown et al. (2002). | 48 |
| Figure 2 - Mass flux onto the lunar surface from meteoroid (solid blue) and NEO (dashed orange) impacts. The mass shown is that of impacting objects that are between 10 g and the mass limit depicted on the ordinate axis. The nominal limits used by MeMoSeE are marked with solid black circles. The mass of a particle that hits the lunar surface once per year (on average) is marked with an open circle, and the mass of a particle that cannot produce ejecta larger than 5 mm in diameter is marked with an open triangle.... | 48 |
| Figure 3 – The mass of particles ejected from the lunar surface due to meteoroid (solid blue) and NEO (dashed orange) impacts. The mass shown is that produced by impacting objects that are between 10 g and the mass limit depicted on the ordinate axis. The nominal limits used by MeMoSeE are marked with solid black circles. The mass of a particle that hits the lunar surface once per year (on average) is marked with an open circle, and the mass of a particle that cannot produce ejecta larger than 5 mm in diameter is marked with an open triangle..... | 50 |
| Figure 5.4-1 Schematic cross-section illustrating the idealized effect of large-scale crater on the structure of the upper lunar crust (ref. 1) | 53 |
| Figure 5.4-2 Cumulative size-frequency diagram for typical lunar surface soil samples. (ref. 1)..... | 53 |
| Figure 5.4-3 The relationship between grain size, sorting, and agglutinate content for 42 Apollo 17 soils (ref. 3 as cited by ref. 1)..... | 54 |
| Figure 5.4-4 Comparison of soil size distributions..... | 55 |
| Figure 5.4-4 Ejecta flux distribution sensitivity to soil size distribution parameters..... | 56 |
| Figure 5.4-5. Dimensions of a simple crater | 57 |
| Figure 5.4-6. Excavation depth into the lunar regolith by sporadic meteoroids | 59 |
| Figure 5.4-7 NEO mass that will excavate to the bottom of regolith 10-m thick resulting in an 37-m diameter crater | 60 |
| Figure 5.4-8 An example of a bench crater in lunar crater Plato. (ref. 7) | 61 |
| Figure 5.4-9 Contribution to the ejecta flux from impacts by sporadic and NEOs with masses less than 1-kg, less than 100-kg and less than 10^7 -kg..... | 61 |
| Figure 5.4-10 Ivanov's estimate of the probability of an NEO impact with the earth as a function of the diameter of the NEO. (ref. 9) | 62 |
| Figure 5.5-1. How to calculate the penetrating flux for single speed and single impact angle ejecta and sporadic meteoroid environments..... | 65 |
| Figure 5.5-2. Scaled ejection mass versus ejection speed for various geological materials. (ref. 5) | 66 |
| Figure 5.5-3. Apollo, Constellation and HLS Crewed Lunar Landers | 67 |

Restricted distribution to NESC and designated team members until approved by the NRB.

| | |
|---|----|
| Figure 5.5-4. Altair surface element model constructed for the Bumper MMOD impact risk assessment..... | 68 |
| Figure 5.5-5. Altair ascent module wall construction..... | 69 |
| Figure 5.5-6. Altair descent module wall construction..... | 69 |
| Figure 5.5-7. Penetrations per square meter per year by sporadic meteoroids and lunar ejecta..... | 70 |
| Figure 5.5-8. Total number of failures due to ejecta and sporadic meteoroid impacts calculated with the two environment sets. | 71 |
| Figure 5.5-9. Number of failures by component, with and without Whipple shields, evaluated with the NASA SP-8013 lunar ejecta environment and the MEM r2 sporadic meteoroid environment | 72 |
| Figure 5.5-10. Number of failures by component, with and without Whipple shields, evaluated with the MeMoSeE lunar ejecta environment and the MEM 3 sporadic meteoroid environment | 72 |
| Figure 5.5-11. Relative number of penetrations per speed bin for the two ejecta environments..... | 73 |
| Figure 5.6-1. The Zook function G(v) scaled to the sporadic meteoroid impact conditions assumed by Zook in his model compared with the function used in the author's MathCAD analysis..... | 75 |
| Figure 5.6-2. Comparison of published Zook ejecta flux curves and the author's MathCAD implementation of the Zook model..... | 76 |
| Figure 5.6-3. Ratio of convergence (μ_n/μ_{50}) as a function of speed bin spacing and number of speed bins..... | 78 |

List of Tables

| | |
|---|----|
| Table 1: Primary ejecta flux versus elevation and speed for 0°N and 0°E. | 34 |
| Table 2: Crater size estimated for each bin assuming a secondary particle size of 0.072 mm and the average impact elevation (PHI _{avg}) and average speed. | 35 |
| Table 5.4-1 NEO diameter at the transition from simple to complex craters | 58 |
| Table 5.5-1 Summary of results with and without shields for two sets of environments. | 72 |
| Table 5.6-1. Ratio of convergence as a function of speed bin spacing and number of speed bins | 78 |

Restricted distribution to NESC and designated team members until approved by the NRB.

Technical Assessment Report

1.0 Notification and Authorization

Dr. Robert Suggs, Human Landing System (HLS) Natural Environments Discipline Lead, requested the NASA Engineering and Safety Center (NESC) perform an independent review of a new lunar meteoroid ejecta model developed by the Natural Environments Branch at Marshall Space Flight Center (MSFC). MSFC has proposed to use the new model to replace the Apollo-era lunar ejecta environments in the SLS-SPEC-159 Cross-Program Design Specification for Natural Environments (DSNE) document that specifies engineering design environments for NASA's Exploration Systems Development (ESD) and Artemis Programs. The NESC assessment team will review the physical basis of the new lunar ejecta model, identify issues with the model should they exist, and provide recommendations for improvements before the model results are incorporated into a DSNE update.

2.0 Signature Page

Submitted by:

Dr. Joseph Minow Date

Significant Contributors:

Dr. Mark Matney Date

Dr. Michael Bjorkman Date

Dr. Jordan Kendall Date

Dr. Althea Moorhead Date

Dr. Menelaos Sarantos Date

Dr. Emerson Speyerer Date

Mr. Michael Squire Date

Dr. Jamey Szalay Date

Signatories declare the findings, observations, and NESC recommendations compiled in the report are factually based from data extracted from program/project documents, contractor reports, and open literature, and/or generated from independently conducted tests, analyses, and inspections.

Restricted distribution to NESC and designated team members until approved by the NRB.

3.0 Team List

| Name | Discipline | Organization (include host Center) |
|----------------------------|---|--|
| Core Team | | |
| Joseph Minow | NESC Lead, Space Environments SME | LaRC |
| Mark Matney | Technical Lead, Meteoroids and Orbital Debris SME | JSC |
| Michael Bjorkman | Meteoroid and Orbital Debris Impact Risk SME | JSC/Jacobs |
| Jordan Kendall | Impact and Cratering SME | GSFC/University of Maryland-Baltimore County |
| Althea Moorhead | Meteoroid Environment SME | MSFC |
| Menelaos Sarantos | Meteoroid and Dust Environment SME | GSFC |
| Emerson Speyerer | Impact and Cratering SME | University of Arizona |
| Michael Squire | Hypervelocity Impact SME | LaRC |
| Jamey Szalay | Impact and Cratering SME | Princeton University |
| Business Management | | |
| Theresa Bardusch | Program Analyst | LaRC/MTSO |
| Assessment Support | | |
| Missy Strickland | Project Coordinator | LaRC/AMA |
| Linda Burgess | Planning and Control Analyst | LaRC/AMA |
| Leanna S. Bullock | Technical Editor | LaRC/AMA |

3.1 Acknowledgments

The assessment team thanks [list of reviewers who provided inputs] for their time and expertise in providing a peer review of this work.

Restricted distribution to NESC and designated team members until approved by the NRB.

4.0 Executive Summary

The NESC Lunar Meteoroid Ejecta Model Review assessment team was tasked with reviewing the proposed lunar ejecta model MeMoSeE, developed at Marshall Space Flight Center, and to review the model inputs to the SLS-SPEC-159 Cross-Program Design Specification for Natural Environments (DSNE) document to be used by NASA’s Exploration Systems Development and Artemis Programs for future lunar surface system design. The model is intended to update the current Apollo-era model contained in the DSNE providing a better understanding of the impact risk to lunar surface operations.

The NESC review team looked at several aspects of the model, focusing on several questions related to the physical basis of the model. Were the direction, velocity, and distributions in time, geography, and size/mass assumed for the primary impactors modeled correctly? Were the direction, velocity, and distributions size/mass/density of the ejecta from the cratering phenomena modeled correctly? Did the transport equations of the debris from cratering events adequately compute the flux on an asset some distance away? Were the DSNE inputs adequate to compute the risks to vehicles, habitats, and other objects on the lunar surface?

Overall, the model was found to incorporate the appropriate phenomenology for a DSNE inputs environment, but with a number of caveats. The review identifies a number of specific sensitivity studies to compare how various sets of assumptions, mostly concerning the physics of the creation of ejecta, would affect the flux calculations. The review also found an unmodeled portion of the flux from ejecta particles ascending from the surface due to nearby primary impacts close by the asset that roughly match in magnitude the NASA SP-8013 flux through a flat sheet lying on the lunar surface. This phenomenon will need to be added to adequately assess the total risk from ejecta.

One important review team finding is that the ejecta flux is highly stochastic, and perhaps a “traditional” average flux may not be adequate to capture some of this highly variable behavior. This could have important implications on how the statistics of risks to surface missions on airless planetary bodies may ultimately be computed.

Finally, the NESC review team did not review the software verification test reports and therefore has no finding on the correctness of the software implementation of the algorithm. No software verification reports were presented to the NESC review team for review and NESC reviews do not perform software verification.

5.0 Introduction and Assessment Plan

The lunar meteoroid ejecta environment is a potential threat to spacecraft and crew operating on and above the lunar surface. The lunar ejecta model used for engineering design by NASA's Artemis Program including the Human Landing System (HLS) and Exploration Extravehicular Mobility Unit (xEMU) System dates to 1969. The SLS-SPEC-159 Cross-Program Design Specification for Natural Environments (DSNE) document applicable for engineering design of all elements of the Artemis Program currently specifies the Apollo era lunar meteoroid ejecta model. MSFC's Natural Environments Branch developed a new lunar meteoroid ejecta model based on improvements since the Apollo days in the knowledge of the primary meteoroid flux at the Moon and impact processes responsible for generating the ejecta environment. MSFC is proposing the new model, named the "Meteoroid Model of Secondary Ejecta" and abbreviated as MeMoSeE (pronounced "mimosa"), replace the 1969 ejecta model in an upcoming DSNE revision scheduled for release in late 2021. HLS, as one of the lunar surface systems primarily impacted by the ejecta environment, requested an independent NESC assessment to review the new lunar ejecta model and proposed update to the DSNE.

The NESC established a review team with expertise on lunar impacts and cratering, hypervelocity impacts, and space environmental effects to review the physical basis of the proposed new MeMoSeE model and the model inputs to the DSNE document to be used by NASA's Exploration Systems Development and Artemis Programs for future lunar surface system design. The model is intended to update the current Apollo-era model contained in the DSNE providing a better understanding of the impact risk to lunar surface operations.

The NESC review team looked at several aspects of the model, focusing on the physical basis of the model. This review summarizes the physical basis of the MeMoSeE model, its applicability to NASA lunar programs, and provides recommendations to improve the model.

6.0 Problem Description

6.1 Prior Work

Prior work on the lunar ejecta environment can be divided into two groups. The first consists of engineering environments for evaluating the spacecraft impact risk. The second is the vastly larger literature considering the ejecta environment as an important geologic process modifying the lunar surface and as a mechanism for lofting dust from the surfaces of airless bodies into solar orbit. The Lunar Source Book (Heiken et al, 1991) is an entrance to the literature on impact as a geologic process and (Szalay et al, 2018) to the literature on lofting dust.

Lunar ejecta engineering models begin with a BELLCOMM study performed for the Apollo program office at NASA Headquarters during 1963. Orrok (1963) concluded in the BELLCOMM study that crater ejecta could no more than double the threat of puncture by meteoroids. He argued that the meteoroid could transfer no more than 100% of its kinetic energy to the lunar ejecta. Because the spacecraft skin thickness that will stop an ejecta particle is proportional to the kinetic energy of the ejecta particle, Orrok thought that the penetration rate at the surface of the Moon would at most be double the penetration rate in lunar orbit. This result was widely circulated at the time as evidenced by the following quote from a NASA history of Apollo.

Restricted distribution to NESC and designated team members until approved by the NRB.

"NASA issued a technical note reporting that scientists at Ames Research Center (ARC) Hypervelocity Ballistic Range, Moffett Field, Calif., were conducting experiments simulating the impact of micrometeoroids on the lunar surface. The experimenters examined the threat of surface debris, called secondary ejecta, that would be thrown from resultant craters. Data indicated that secondary particles capable of penetrating an astronaut's space suit nearly equaled the number of primary micrometeoroids. Thus the danger of micrometeoroid impact to astronauts on the moon may be almost double what was previously thought."

(Morse and Bays, 1973; see also Miller, 1963.)

NASA engineers quickly recognized that an estimate of a factor-of-two larger risk was quite pessimistic because the average speed of ejecta particles is much less than the average meteoroid speed. The Manned Spacecraft Center (MSC) EC-1 meteoroid environment spec (Anonymous, 1963) included a lunar ejecta environment that reduced the risk from ejecta to a factor two orders of magnitude smaller than the risk from sporadic meteoroids. The results from Gault's impact tests at ARC (Gault et al., 1963) mentioned above indicated that the ejecta flux was three to four orders of magnitude larger than the meteoroid flux. The writers of EC-1 chose the ejecta flux to be an intermediate value of 6,800 times larger than the incident meteoroid flux. The ratio of ejecta flux to incident flux coupled with the Whipple (1963) sporadic meteoroid flux relation (where $F \propto m^{-1.34}$), an average sporadic meteoroid speed of 30 km/s and an average lunar ejecta particle speed of 200 m/s gave exactly a factor of 100 between the incident penetrating meteoroid flux and the penetrating lunar ejecta flux.

Zook (1967) extended the EC-1 ejecta environment analysis by considering a distribution of ejecta speeds, binned into three ranges of speed: 0 to 100 m/s, 100 to 250 m/s and 250 m/s to 1 km/s. Figure 6.1-1 is a plot of the flux curves for each of the 3 speed bins. Like the EC-1 environment spec, Zook based his analysis on Gault's basalt cratering results. Zook's lunar ejecta environment gives a comparable ratio between the ejecta flux and the incident flux (~100), however, Zook based the incident meteoroid flux on the smaller DS-21 REV A (January 1967) environment specification. This environment specification revised the sporadic meteoroid flux down by a factor of 12.

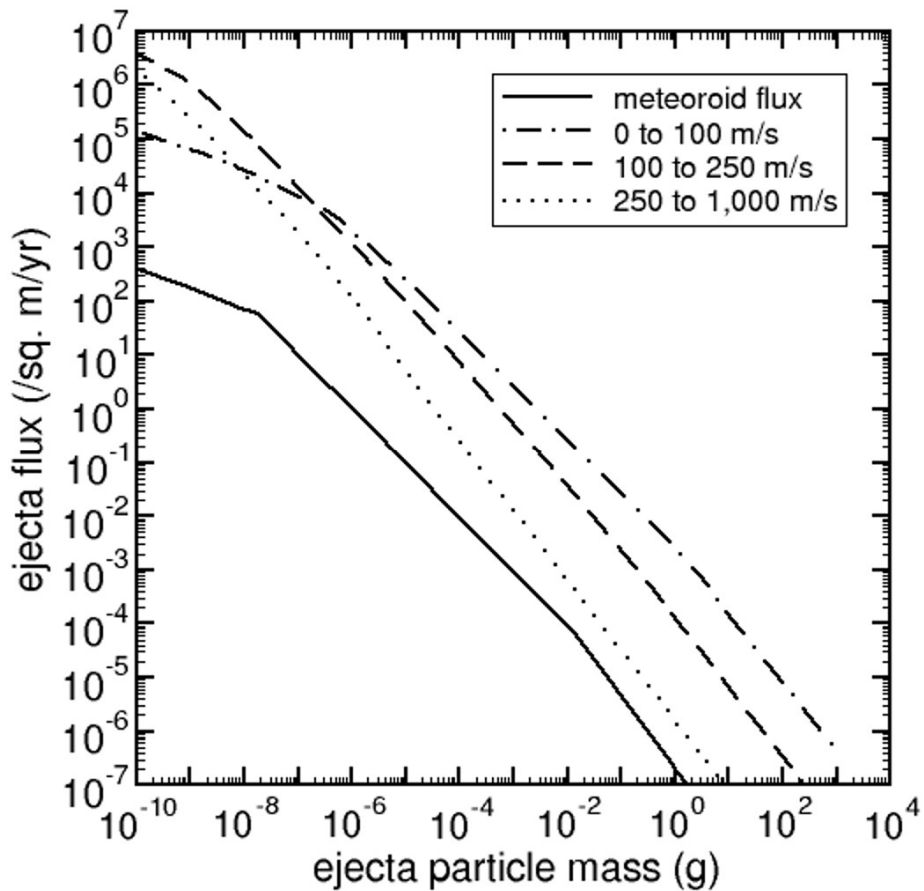


Figure 6.1-1. Zook's cumulative ejecta flux environment.

The NASA SP-8013 meteoroid environment (Cour-Palais, 1969) released in 1969 also broke the ejecta flux up into three speed bins, similar to Zook, but took the same approach as EC-1 and used a fixed ratio of penetrating sporadic flux to penetrating ejecta flux. NASA SP-8013 contains a model of the flux of ejecta particles for particles with speeds from 0 to 100 m/s, 100 to 250 m/s and 250 m/s to 1 km/s. NASA SP-8013 specifies a 100-m/s average ejecta speed. Figure 6.1-1 is a plot of the NASA SP-8013 ejecta fluxes. NASA SP-8013 does not specify the upper size limit of ejecta particles; however, it does plot the flux for masses up to 100 g.

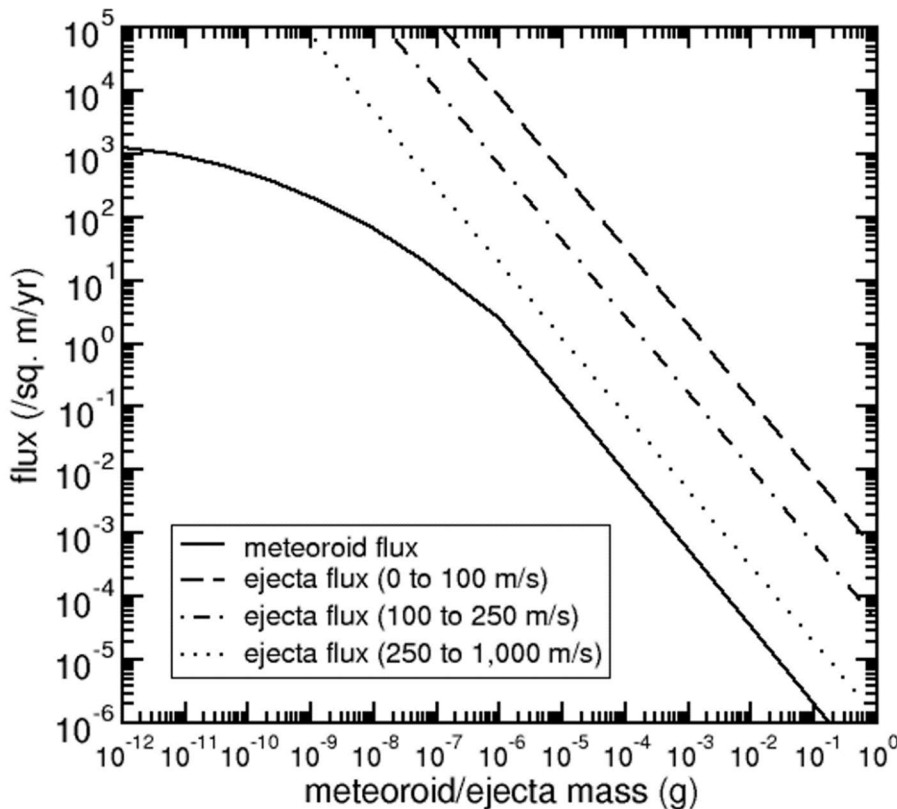


Figure 6.1-2 NASA SP-8013 cumulative ejecta flux environment.

The NASA SP-8013 is the last released lunar ejecta environment for design. It is currently the environment specified in the DSNE.

The four engineering environment models described here have trended towards smaller and smaller impact risk as the modelers eliminated conservatism. MeMoSeE continues this trend; however, the lunar ejecta impact risk is not ignorable for all spacecraft components as section 10.5.2 describes.

6.2 Summary of MeMoSeE model

MeMoSeE combines models of impacting particles (both meteoroids and asteroids or comets) with cratering relations and regolith properties to generate a description of lunar ejecta particles.

6.2.1 Input models

MeMoSeE relies on two separate models of incoming particles to compute the impact rate. These models are the Meteoroid Engineering Model (MEM, version 3; Moorhead, 2020a; Moorhead et al., 2020) and a very simple near-Earth object model (Brown et al., 2002; Moorhead 2020b).

MEM is a mature model that has been in use since 2004 to compute the flux of hazardous meteoroids for spacecraft risk assessments. It contains a physics-based, dynamical model of the meteoroid complex (Jones et al., 2001; Jones 2004) that has been recently updated to include meteoroid density information derived from ablation modeling (Kikwaya et al., 2011; Moorhead et al., 2017). MEM 3 has been validated against spacecraft impact rates measured by the Pegasus

Restricted distribution to NESC and designated team members until approved by the NRB.

and Long Duration Exposure Facility (LDEF) satellites (Moorhead et al., 2020). It reports the flux of meteoroids and its breakdown by mass, speed, angle, and density, providing the quantities needed by MeMoSeE to compute the ejected mass (see equation ??).

Unlike MEM, the near-Earth object model used by MeMoSeE is quite simplistic. It is constructed by combining the estimated flux of large objects onto the Earth's atmosphere (Brown et al., 2002) with the speed distribution of bolides reported on the CNEOS website. The directionality of near-Earth objects is not modeled; instead, the impact angle distribution is assumed to be the same as that of the high-density meteoroid population in MEM.

6.2.2 Cratering relations

The model uses a relation given in Housen and Holsapple (2011) to compute the mass ejected from an impact as a function of: secondary ejecta speed, target density, impactor mass, impactor density, impactor speed, and impact angle from the surface normal. This framework uses scaling laws to extend the range of experimentally determined ejecta properties given in 16 separate references and is utilized in here to compute lunar impact ejecta properties. Equation 2.18 summarizes the scaling laws used in the model. This model does not use the empirical relations in Koschny and Grün (2001), which were applicable to solid ice-silicate mixtures.

Once the total ejected mass as a function of speed is computed following the Housen and Holsapple (2011) scaling relations, the model incorporates additional assumptions on the ejecta mass and angular distributions. The model assumes the angular distribution is independent of speed and particle size and adopts the zenith and azimuth distributions from Rival and Mandeville (1999).

6.2.3 Assumptions

As with any physical model, there are several simplifying assumptions in the model to make the calculations simpler. We will try to summarize them in this section.

6.2.3.1 Flux calculation assumptions

The MeMoSeE flux is calculated assuming a flat disc on the surface of the Moon. In order to avoid calculation difficulties, no primary impacts are assumed to occur within a 1 km radius of the target disc. Also, the ejecta population is assumed to be only from those particles that have passed their apoapsis and are starting to descend onto the lunar surface. Note that particles are assumed to be on elliptical Kepler orbit paths until they re-encounter the lunar surface, so secondary perturbation effects, such as the gravity of the Earth, are ignored.

The flux is calculated as an average where impacts around the Moon are integrated over time and geography.

6.2.3.2 Cratering assumptions

There are a number of assumptions in the model about how the particles are ejected from an impact event in zenith angle (the angle from the local normal), in azimuth (due to the direction of the primary impactor hitting at oblique angles), in size distribution, and in ejection speed. There are also assumptions about the composition (primarily material density) of the ejecta particles,

based on assumptions of the composition of the surface of the Moon where the impact occurs. All of these assumptions are spelled out in the documentation.

One assumption that may affect ejection directions is that the model assumes the surface of the Moon to be a smooth sphere. While this is probably a good assumption for large impacts, local structure (e.g., hills, rocks) may influence the ejection physics of small impacts. MeMoSeE uses radius of this smooth lunar sphere that differs from the one used by other lunar scientists.

Observation 1: The radius of the Moon used in MeMoSeE is 1737.1 km instead of the traditional 1737.4 km. The 1737.1 km value is also used by the model when calculating the escape velocity.

Recommendation 1: Use the canonical value of 1737.4 km for the geometrically averaged lunar radius.

6.2.4 Model name and acronym

The model is named the "Meteoroid Model of Secondary Ejecta" and abbreviated as MeMoSeE (pronounced "mimosa"). This name and acronym are likely to be troublesome for a number of reasons:

1. It contains the words "meteoroid model" but does not describe meteoroids. (Ejected particles that remain gravitationally bound to the Moon do not meet the International Astronomical Union's definition of a meteoroid:
https://www.iau.org/static/science/scientific_bodies/commissions/f1/meteordefinitions_approved.pdf)
2. It does not contain the words "lunar" or "Moon" even though the model is specific to the Moon (for instance, the size distribution of the ejecta particles is taken from that of the lunar regolith).
3. The term "secondary ejecta" is somewhat ambiguous. Some researchers use the term to describe particles ejected from primary impact craters, but others describe such particles simply as "ejecta." These ejected particles can go on to produce secondary impact craters, which can excavate a new population of ejected particles. One could conceivably call this third population of particles, or second population of ejected particles, "secondary ejecta." However, this latter population is not included in the model.
4. The acronym is rather long and alternates between uppercase and lowercase letters. This is tedious to type and is unlikely to be rendered correctly by anyone other than the model creator.
5. The pronunciation chosen by the model creator (which resembles "mimosa") will not be apparent to those encountering the acronym in print. Native English speakers are most likely to pronounce it as "memo-see". The differences in both stress pattern and vowel sounds could produce confusion in meetings and presentations; listeners may not even realize that "mimosa" refers to MeMoSeE.

Observation 2: The model name "Meteoroid Model of Secondary Ejecta" does not accurately and unambiguously describe the environment modeled and the acronym (MeMoSeE, pronounced "mimosa") is difficult to type and unclear how to pronounce.

Recommendation 2: Consider changing the model name and acronym to those that emphasize accuracy and ease of use. For example, "Lunar Ejecta Engineering Model (LEEM)" would be clear, accurate, and simple to type and pronounce.

Observation 3: Both the model acronym and documentation use the term "secondary ejecta." This term can be ambiguous, as it can be confused with other phenomena on the Moon.

Recommendation 3: Use the terms "secondaries," "secondary environment," or "ejecta" in place of "secondary ejecta."

6.3 Model use

Spacecraft can be damaged in a number of ways, and one source of risk is penetration of the spacecraft by particle impacts. These particles can be either man-made (such as orbital debris) or natural (such as meteoroids). The risk of penetration by these particles can be assessed by combining up-to-date models of the environment, a spacecraft description and trajectory, and damage equations using a risk assessment code (see Figure 6.2-1). NASA's primary risk assessment code is Bumper, which is operated by the Hypervelocity Impact Technology (HVIT) team at Johnson Space Center.

The risk of damage from impacts is governed not only on the number and properties of particles striking a spacecraft but also by the spacecraft or asset configuration and its location and motion. For instance, a sheet of mylar may be vulnerable to small impacts and therefore penetrated many times compared to a plate of mm-thick aluminum. A simple Whipple shield is very effective at protecting a surface from high-speed meteoroid impacts, but less effective at blocking slower particles (for this reason, it is customary to use a stuffed Whipple shield to protect against orbital debris impacts, which are slower than meteoroids). Furthermore, a spacecraft's motion can increase (or decrease) the relative speed of some impacts, changing the risk they pose. Thus, the outputs from models such as MeMoSeE must be combined with a spacecraft or asset description and trajectory and the risk of failure or penetration computed according to ballistic limit or damage equations that are specific to the materials in question. This combination of information and analysis flow is depicted in Figure 6.2-1.

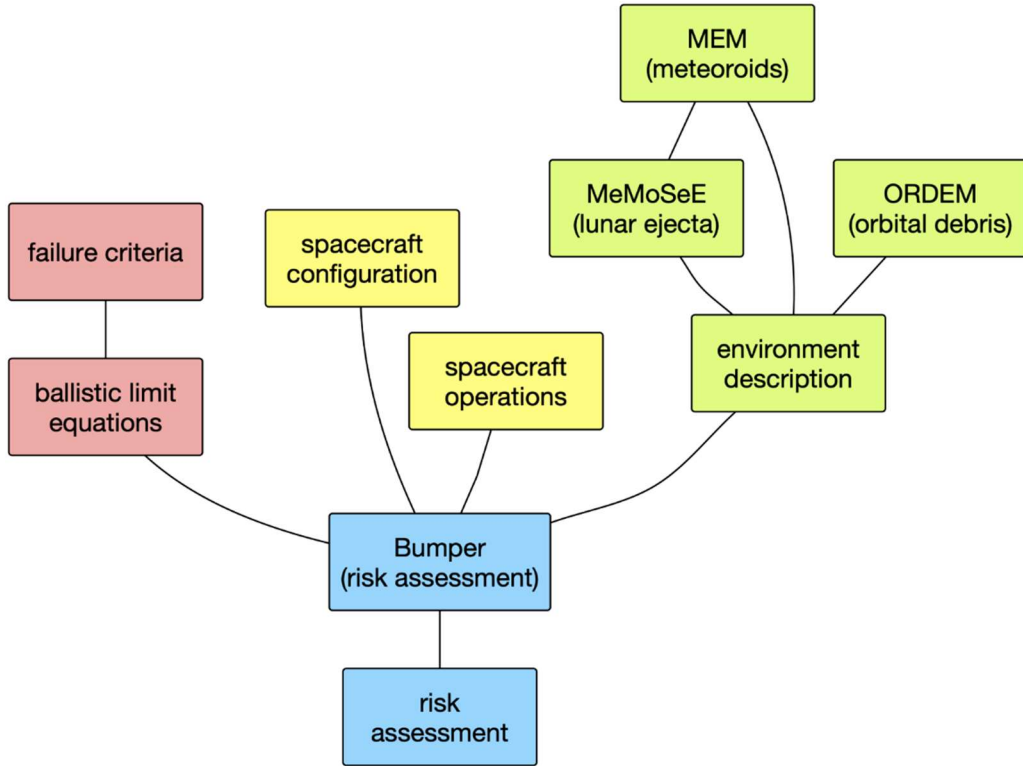


Figure 6.2-1. Risk assessment model flow chart.

MeMoSeE will be one of three environment models that is integrated into the Bumper risk assessment code. The other two are the Meteoroid Engineering Model (MEM) and the Orbital Debris Engineering Model (ORDEM). MEM contains a dynamical model of the meteoroid environment and uses this model to compute the flux, speed, impact direction, and bulk density of meteoroids striking a spacecraft on a given trajectory. Users may either attempt to interpret MEM's outputs directly, or they can use an established risk assessment code. Similarly, users can use ORDEM to generate descriptions of the debris environment near Earth, or they can rely on Bumper. However, ORDEM is not relevant for lunar-orbiting spacecraft, as the amount of debris generated in cislunar space is far lower and lunar orbits unstable.

Unlike MEM and ORDEM, the MeMoSeE code is not intended for public distribution nor for direct incorporation into Bumper. Instead, the developers plan to use it to generate location-specific descriptions of lunar ejecta in the form of tables that can then be incorporated into risk analyses. The main output are tables of flux that will be provided via the Design Specification for Natural Environments (DSNE) document (see, e.g., Roberts et al., 2019).

While MeMoSeE relies on MEM to calculate the rate of ejecta-generating meteoroid impacts, it is not responsible for generating a description of the meteoroid environment for incorporation into Bumper. MEM continues to provide that information for risk assessments. MEM describes the meteoroid flux only; this includes natural particles traveling through interplanetary space, but it does not include particles liberated from the surface of the Moon by meteoroid or asteroid impacts. These ejected particles largely remain gravitationally bound to the Moon and do not contribute to the meteoroid environment as a whole but may be able to significantly increase the particle flux near the lunar surface. MeMoSeE fills this gap by modeling lunar ejecta.

6.3.1 DSNE inputs

The primary use of MeMoSeE is to generate tables of the flux of ejected particles that can be incorporated into the DSNE document (Roberts et al., 2019). **The DSNE describes a wide variety of environmental hazards and is referenced during the design phase of a mission.**

The model developer has drafted a new proposed section of the DSNE on lunar ejecta that briefly describes the model and contains three flux tables, a single particle density value, and a size-scaling relation. Each table corresponds to a different selenographic latitude or pair of latitudes (0° , $\pm 45^\circ$, and $\pm 90^\circ$) and reports the flux in three velocity bins and nine elevation angle bins. The fluxes are those of particles between 1 micron and 1 centimeter in "size", although it is not specified whether this size is radius, diameter, or some other quantity.

The damage done by a particle impact is typically expressed as a function of impactor diameter, bulk density, speed, and impact angle. Thus, some description of these four quantities must be provided. The proposed DSNE inputs break the flux down by impact speed and elevation angle; it is stated that the variation with azimuth is small, implying that readers should assume axisymmetry about the zenith. The size distribution is handled by providing an equation that can be used to scale the flux values to the desired minimum "size," and readers are advised to use a particle density of 3100 kg m^{-3} .

6.3.2 Bumper integration

MeMoSeE output is an input to the micrometeoroid impact risk codes used to verify spacecraft meet the impact risk system-requirements. The computer program Bumper is the NASA product used to evaluate NASA spacecraft (see, section 10.5.2), however the NASA partners also use a number of different codes. The MeMoSeE and Bumper developers concurred on the format of the tables of MeMoSeE output included in a DSNE draft during the third quarter of 2020. Subsequently, the Bumper developers implemented the MeMoSeE environment tables in a developmental version of Bumper. The MeMoSeE environment is not available in versions of Bumper released to NASA partners and contractors.

The Bumper developers think implementing the MeMoSeE environment in the NASA partner codes is straightforward. This can be done by either reformatting the DSNE tables into the STENVI environment data interchange format (which is read directly by the European Space Agency's ESABase code) or through copying the DSNE tables into code specific input data files as the Bumper developers did.

Finding 1: The DSNE tables do provide the information necessary for Bumper MMOD risk assessments.

7.0 Section 1 - Primary impact flux

MeMoSeE models the flux, speed, and elevation angle of particles produced by impacts of meteoroids and asteroids on the lunar surface. These primary impactors range in mass from $1 \mu\text{g}$ to $1.6 \times 10^{15} \text{ g}$ in size, where the upper bound is the mass of a sphere that is 1 km in diameter and has a density of 3000 kg m^{-3} .

Restricted distribution to NESC and designated team members until approved by the NRB.

7.1 Meteoroids

Small primary impactors, or meteoroids, are modeled using the Meteoroid Engineering Model (MEM), version 3 (Moorhead, 2020a; Moorhead et al., 2020). For each selenographic latitude of interest, the modeler generated a series of state vectors corresponding to a point on and rotating with the surface of the Moon at that latitude. These state vectors spanned a Metonic cycle (19 years) and thus represent an average meteoroid environment seen at that latitude. The resulting fluxes, speeds, and impact angles generated by MEM were used as inputs to the chosen cratering relation.

MEM specifically describes the sporadic meteoroid complex, and the particles it models arise from different families of comets. It does not describe the directionality of near-Earth objects (NEOs). Thus, above a certain size threshold, it becomes necessary to switch to an asteroid dynamical model. MEM's upper mass limit is 10 g, and so the modeler uses this as the dividing line between meteoroids and asteroids.

MEM 3 is a mature, peer-reviewed model. It is not the only possible choice for describing meteoroid impacts, but it is certainly reasonable to use MEM 3 to describe the flux, speed, density, and directionality of meteoroids impacting the Moon in the 1 μg --10 g mass range.

7.2 Near-Earth objects

7.2.1 Flux

Above the 10 g threshold, the modelers use the Brown et al. (2002) relation for the NEO flux, adjusted for the difference in gravitational focusing at the Moon vs. the Earth and converted to a mass-limited flux (Moorhead, 2020b). The flux per unit lunar surface area is

$$g_{lun} = 2.89 \times 10^{-11} \text{ m}^{-2} \text{ yr}^{-1} \cdot m^{-0.9}$$

where m is the mass of the impactor in kg. Above the 10 g threshold, MeMoSeE rescales the high-density component of the MEM outputs such that its total matches that of Eq. flun, after multiplying by 4 to convert to a flux per unit cross-sectional area. However, this re-scaling appears to be done incorrectly.

Eq. flun gives the large impactor flux averaged over the entire surface of the Moon. This is most analogous to the flux computed for MEM on an outward-facing plate. It is not analogous to the "total cross-sectional flux" listed at the top of the MEM output files, which is analogous to the flux on a sphere hovering just above the lunar surface. Furthermore, the total flux computed by MEM may vary per location.

Finding 2: The NEO flux appears to be implemented incorrectly in the model. A meteoroid flux that is partially shielded by the Moon is rescaled using a NEO flux that contains no such shielding.

Recommendation 4: The meteoroid-to-NEO flux scaling should be conducted using the meteoroid flux on a flat plate facing away from the lunar surface and the NEO flux on the lunar surface per unit surface area.

One possible approach is the following:

- [1] Select a large number of random points on the surface of the Moon's surface, and a corresponding number of random Julian dates within a single Metonic cycle.
- [2] Generate a "trajectory" file that corresponds to these points and dates, where the velocity vectors reflect the rotation of the lunar surface.
- [3] Perform a MEM run using this trajectory file, a limiting mass of 10 g, and a body-fixed coordinate system for outputs (so that the $+z$ direction will point directly outward from the lunar surface).
- [4] Extract the total flux for the appropriate population (low- or high-density) on a space-facing surface: this will correspond to the \hat{z} direction. Divide Eq. flun by this quantity to obtain a flux scaling term as a function of limiting NEO mass that can be applied to MEM flux elements.

7.2.2 Speed distribution

MeMoSeE adopts a NEO speed distribution that is derived from speeds of kiloton-or-larger impacts on the Earth's atmosphere, taken from the CNEOS website (<https://cneos.jpl.nasa.gov/fireballs/>) and converted to a mass-limited lunar speed distribution (Moorhead, 2020b). This is a global average; it is unknown whether the speed distribution varies substantially from location to location on the lunar surface. However, this question cannot be easily answered without constructing a full dynamical model of the NEO population.

7.2.3 Directionality of larger objects

A geocentric radiant distribution is not available from the CNEOS data. MeMoSeE therefore assumes that the orbital inclinations of NEOs are concentrated near the ecliptic, and, on that basis, assumes that their zenith angles relative to the lunar surface will be distributed similarly to that of helion/antihelion meteoroids in MEM (also known as the "high density population" in MEM 3), which are also concentrated near the ecliptic.

To test the validity of this assumption, we have constructed a crude model of the NEO population by replacing MEM's distributions of meteoroid orbits with those of near-Earth asteroids taken from JPL's Small-Body Database. The population was chosen by using a cumulative magnitude distribution and finding the point where the cumulative curve "turned over"; which would mark the brightness below which the population was starting to be incomplete. While this sub-population is more likely to be complete, it is not fully corrected for observing biases, and thus may differ from that encountering the Moon. However, this simple test reveals that the angles at which NEOs encounter the Moon do not, in fact, resemble those of helion meteoroids. Instead, these angles are more similar to those of the "low density population," which consists of apex and toroidal meteoroids.

Figure 1 presents the elevation angles of NEAs impacting the lunar surface for three locations: a point near the lunar equator (top left), a point near 45° S (top right), and a point near the lunar south pole (bottom left). In each case, we compare the NEA zenith angle distribution with that of the high-density and low-density populations from the Meteoroid Engineering Model (MEM). The high-density meteoroid population seems to be more similar to the NEAs in its distribution of elevation angles. At bottom right, we compare the speed distribution of NEAs impacting the lunar surface, averaged over all locations, with that derived from CNEOS data (Moorhead

2020b). The NEA-MEM speed distribution appears faster than that derived from the CNEOS data; this may be due to detection biases.

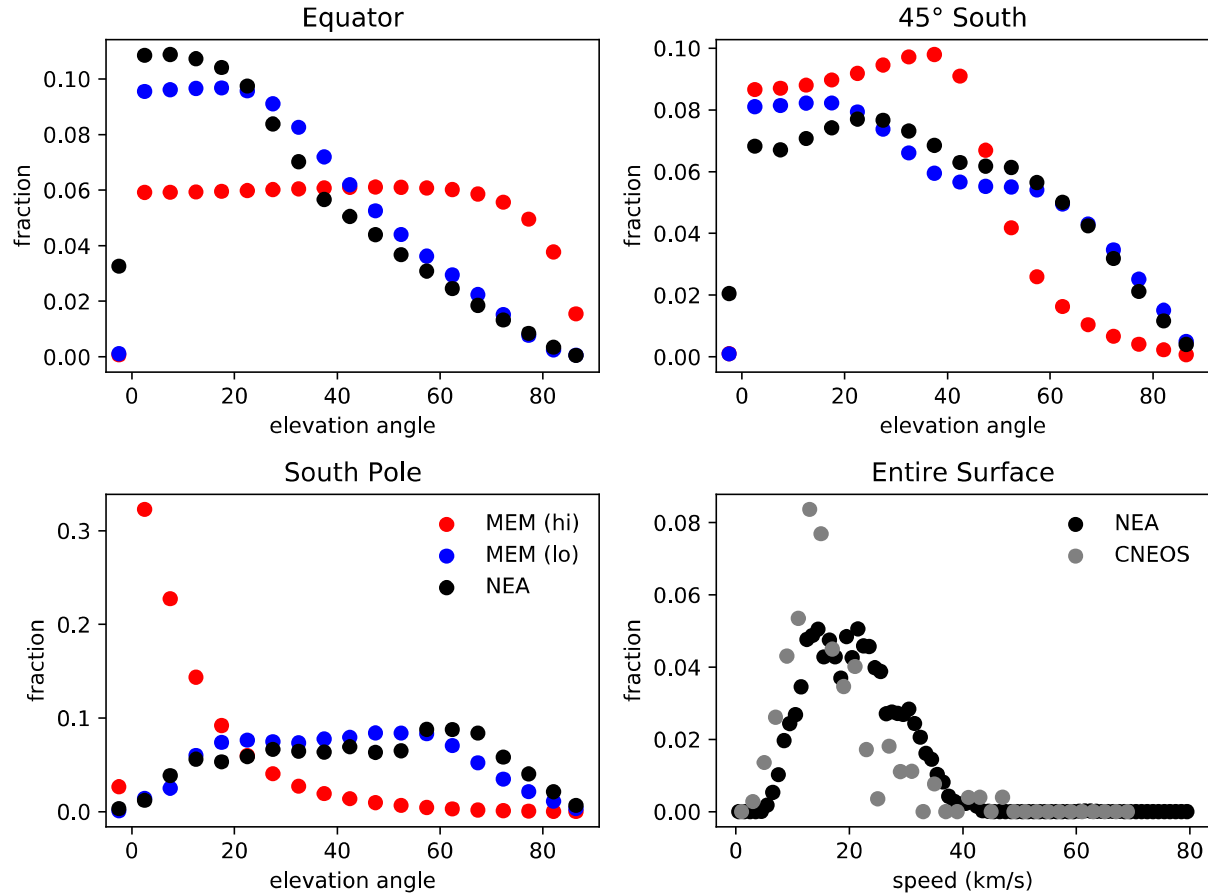


Figure 1 - Elevation angle and speed distributions of NEAs impacting the lunar surface.

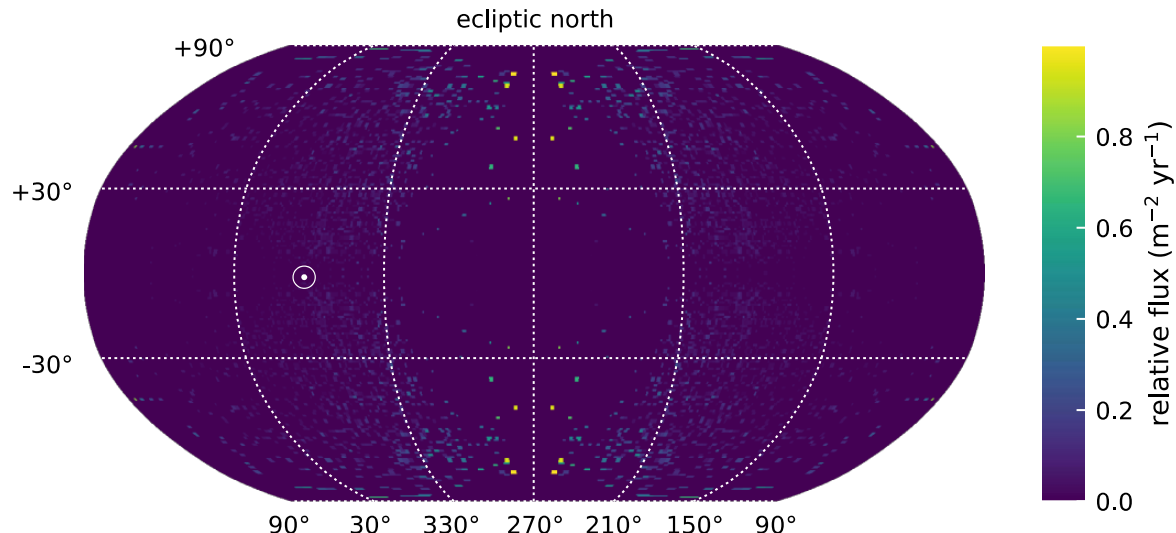


Figure 2 - Directionality of NEAs relative to an object orbiting the Sun at 1 au.

Restricted distribution to NESC and designated team members until approved by the NRB.

Figure 2 presents the directionality of NEAs relative to an object orbiting the Sun at 1 au, modeled using the framework of the Meteoroid Engineering Model (MEM). Angular coordinates are in a Sun-centered ecliptic frame, in which the center of the plot (270° , 0°) points in the direction of the reference object's orbital motion (i.e., "ram"). Again, the directionality does not resemble that of the high-density population in MEM. This difference in behavior is very likely due to the fact that NEOs are on more circular orbits than most meteoroids, which originate primarily from comets. A relatively small inclination can correspond to a fairly inclined selenocentric trajectory: a small out-of-ecliptic velocity component will be proportionally larger to the in-ecliptic velocity component after subtracting the Moon's velocity vector.

Finding 3: The model's assumed angles of incidence of NEO impactors with respect to the Moon's surface resembles the MEM high density population. However, these directions should more closely resemble the low-density meteoroid population in MEM than the high-density population.

Recommendation 5: Consider replacing the NEO angular distribution with that of the low-density MEM population.

8.0 Section 2 - Ejection process

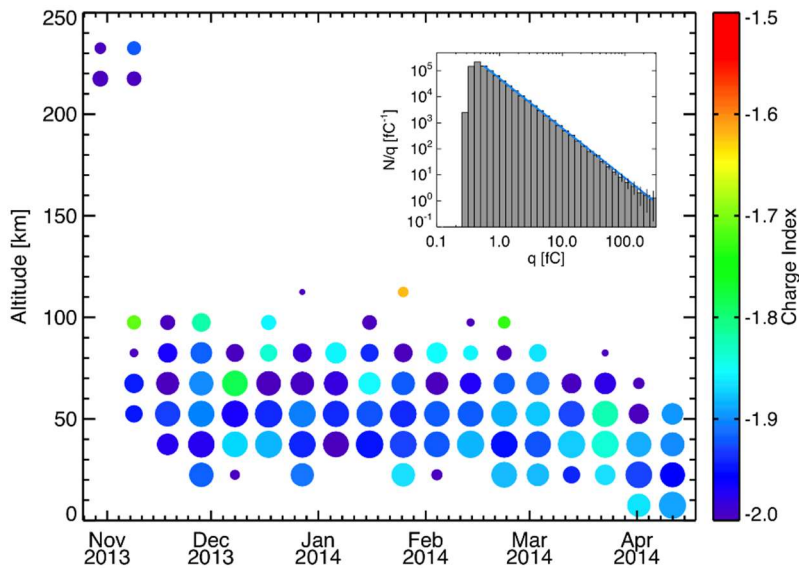
This section will compare the MeMoSeE model crater ejection phenomena and corresponding output to observations acquired by the Lunar Atmosphere Dust and Environment Explorer (LADEE) and the Lunar Reconnaissance Orbiter (LRO). The LADEE mission launched in September 2013 and entered orbit on 6 October 2013. During the 100-day science mission, the Lunar Dust Experiment (LDEX) recorded more than 11,000 impacts from dust cloud particles. The LRO spacecraft launched in June 2009 and has been orbiting the Moon for nearly 12 years. The spacecraft is equipped with two Narrow Angle Cameras (NACs) and a Wide Angle Camera (WAC) packaged together as the Lunar Reconnaissance Orbiter Camera (LROC).

8.1 LADEE Comparison

8.1.1 Size distribution

The discussion and last two paragraphs of Section 2.5.1 discusses how the size distribution is modified to account for the LADEE-observed power-law cumulative size index of -2.7 (Horányi et al. 2015) for grains with radii below $\sim 5 \mu\text{m}$ (Report Figure 1). Report Figure 1 shows the exponent of the power-law distributions fitted to LDEX measurements as functions of altitude (15 km bins) and time (10 day bins). The color indicates the value of the differential mass distribution index ($1+\alpha$), and the size of a circle is inversely proportional to its absolute uncertainty. The inset shows the impact charge distribution for all heights for the entire mission, resulting in a χ^2 minimizing fit of $\alpha = 0.910 \pm 0.003$. From Horanyi et al. (2015). The model adequately accounts for the LADEE size distribution measurements in the triple power-law distribution given in Equation 2.16.

Finding 4: The model adequately accounts for the LADEE ejecta particle size distribution measurements.



Report Figure 1. Slope of the charge and mass distributions.

8.1.2 Ejecta Yield

The ejecta yield is the ratio of total ejecta mass produced to the total impacting mass. For example, an ejecta yield of 100 means that 100 times more mass is produced as secondary impact ejecta than the total sum of primary impacting meteoroid masses. The ejecta yield for MeMoSeE was estimated to be on the order of 10-20 for impactors in the 1 microgram to 10 gram range, which are commensurate with those observed by LADEE. LADEE observed yields ~ 10 (Szalay et al. 2019, Pokorny et al. 2019) for the Moon's fine regolith surface. This is in contrast to yields $\sim 10^3$ - 10^4 at the icy Galilean moons of Jupiter (Table 3 in Krüger et al. 2003). To explain the low ejecta yield measured by LADEE compared to the Galilean moons, we suggested that “the ejecta observed by LDEX may have been launched from the surface under an entirely different regime of impact ejecta physics, where a much larger fraction of the energy is available to be partitioned into local heating of the regolith instead of into the kinetic energy of launched particles” (Szalay et al. 2019).

The preliminary value 10-20 derived for this model is consistent with the LADEE observations. Our main explanation for the low yields from LADEE is that the impactor and regolith sizes were comparable for the LADEE observations, leading to a less efficient production of ballistic ejecta. In the other limit (icy Galilean moon surface), an impact into a solid surface gives significantly larger yields. As this model deals with impactors typically larger than those producing the ejecta observed by LADEE (which was likely at the lower limit of this model of 10^6 g), it is reasonable to expect a larger yield. The fact that the yield of 10-20 used in MeMoSeE agrees with that for the fine regolith LADEE-derived yield of 10 suggests the total ejecta production is well estimated in this model.

Finding 5: The magnitude of ejecta yield in the model reasonably matches LADEE data.

Restricted distribution to NESC and designated team members until approved by the NRB.

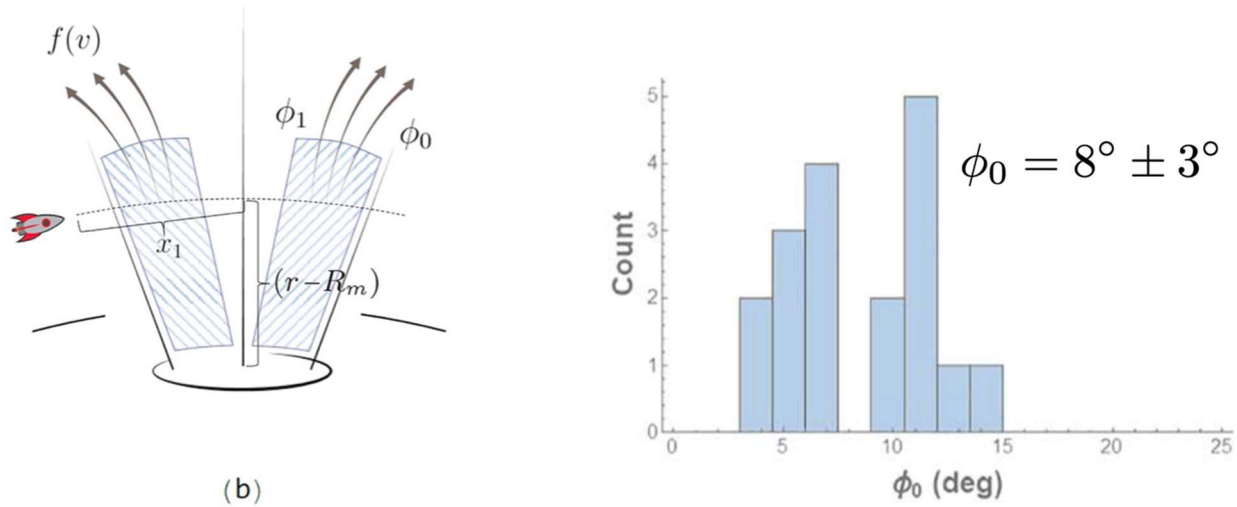
8.1.3 Angular distribution

The model is not fully consistent with LADEE results for the ejecta angle distribution, but this may not mean the model is unrealistic. For background, LADEE typically detected a single ejecta particle per lunar impact event. However, occasionally it observed dense ejecta plumes when a large number of LADEE detections were attributed to a single lunar impact. In these cases, the LADEE data allowed for estimates of the impact ejecta plume properties, notably the exterior angle (which should be analogous with the Zenith Angle). For the dense plume detections by LADEE, we found that angle to be $8^\circ \pm 3^\circ$ (Bernardoni et al. 2019), as shown in Report Figure 2. In this figure, the left shows the assumed plume parameters for simulation to compare to LADEE/LDEX plume observations. The right panel shows a histogram of fitted outer plume angles. Plumes with outer angle $8^\circ \pm 3^\circ$ were consistent with LADEE/LDEX observations (from Bernardoni et al. 2019).

This angle is notably narrower than any of the zenith angles given in Table 2 and could have bearing in the ejecta distance estimates. The LADEE data also does not give any information on the impact zenith angle, so the values it determines represent an average over a range of impact zenith angles for LADEE's latitudinal range of approximately $\pm 20^\circ$ selenographic latitude. It was posited that the LADEE-observed plume detections were "reverse plumes", which are "narrow high-velocity plumes produced shortly after the initial plume cone is generated due to the swift collapse of the crater or impactor breakdown". Hence, the LADEE observations may not represent the bulk of the ejecta distribution and therefore the discrepancy between this model's assumptions and the narrow LADEE plumes is not in direct contradiction.

Finding 6: The model ejecta angular distribution does not reproduce LADEE measurements.

Recommendation 6: Incorporate LADEE ejecta angular distributions into the model. If the resulting assessed risks are significantly different, permanently incorporate the LADEE ejecta angular distributions into the model.



Report Figure 2. Angular ejecta distribution from LADEE/LDEX.

Restricted distribution to NESC and designated team members until approved by the NRB.

8.1.4 Velocity Distribution

Combining Equations 2.18 and 2.68, the model includes a complex speed dependence. This speed dependence appears fundamentally to be related to a power-law distribution, which is different than the one derived from LADEE data. The LADEE distribution was derived with certain assumptions. First, LADEE/LDEX measured impact rates, not densities. To convert rates into densities, knowledge or assumptions about the impact velocity vector must be determined. The following assumptions were made: 1) all grains detected by LADEE had no horizontal velocity component (launched purely normal from a reference lunar spheroid), 2) grains were detected at their vertical turning points, such that they had zero relative speed with respect to the Moon.

After these assumptions were made, the impact rates were converted into impact ejecta densities. It was then found that the density as a function of altitude was well-represented by an exponential, such that $n(h) = n_0 \exp(-h/h_0)$ where a scale height of $h_0 = 200$ km best fit the data (Szalay and Horányi, 2016). From conservation of energy, this density distribution was then inverted to derive an initial impact ejecta speed distribution,

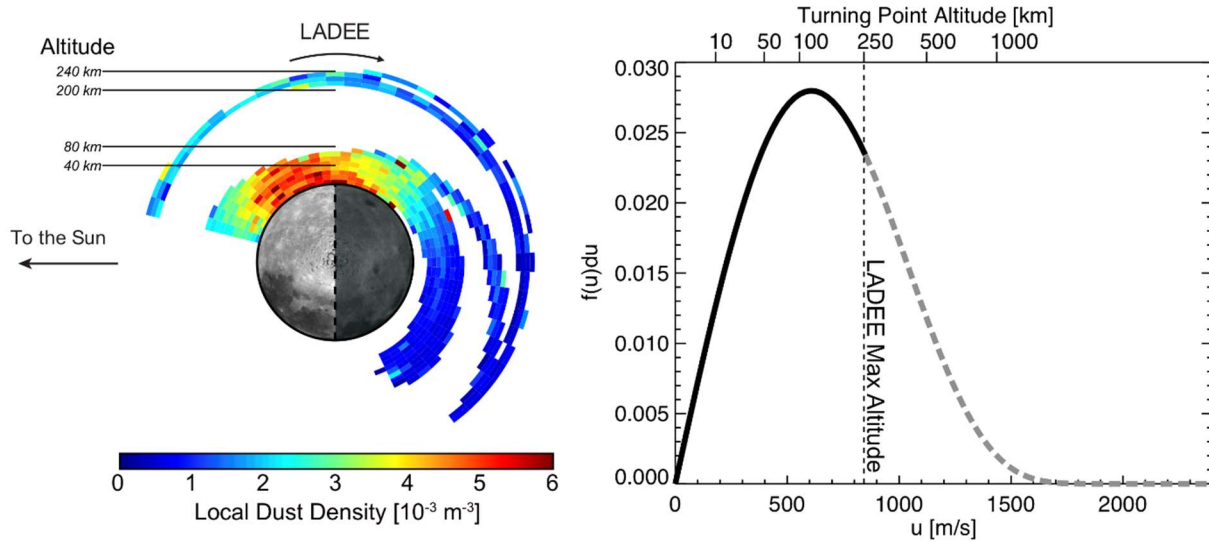
$$f(\hat{v}) = \frac{\delta \hat{v}}{(1 - \hat{v}^2)^2} e^{-\frac{\beta \hat{v}^2}{1 - \hat{v}^2}}$$

where $\hat{v} = v/v_{esc}$ is the speed normalized by the Moon's escape speed, and $\beta = 8.69$ & $\delta = 7.2 \times 10^{-3}$ s m⁻¹ (Eq. 1 in different form in Szalay and Horányi, 2016; Eq. 19 in Szalay et al. 2018). Report Figure 3 (right panel) shows this inferred speed distribution from LADEE/LDEX data, calculated using $\sim 140,000$ impacts averaged over LADEE's 6 months of operations in lunar orbit. White regions indicate locations either LADEE did not visit or that LDEX could not take measurements due to sun pointing constraints. Altitude bands are not to scale. The right panel shows the inferred surface ejecta velocity distribution from the altitude density fit. The dotted line indicates the maximum altitude explored by LADEE, above which the distribution function is an extrapolation. From Szalay et al. (2018). Notably, the lunar speed distribution derived from LADEE/LDEX avoids the artificial cutoff speed required for purely power-law distributions which are not defined at $v = 0$. However, it also has intrinsic assumptions that limit it to purely bound ejecta, as it was derived assuming all detected impacts were bound (at their vertical turning points). Hence, it is an approximation of the impact ejecta speed distribution.

The power-law ejecta speed distribution function is used extensively throughout the literature and provides a common framework to cross-compare measurements. However, this distribution is not consistent with the impact ejecta distribution observed at the Moon for grains with radii below ~ 5 μ m.

Finding 7: The shape of the model's ejecta speed distribution differs from the exponential distribution determined from LADEE observations.

Recommendation 7: Incorporate LADEE ejecta speed distributions into the model. If the resulting assessed risks are significantly different, permanently incorporate the LADEE ejecta speed distributions into the model.



Report Figure 3. Left. The dust density distribution about the Moon.

8.1.5 Ejected Mass

Both the projectile and the target density are used in the ejecta rate calculation. Whereas the meteoroid density of 2.5 g cm^{-3} is frequently assumed as the standard projectile density (Grun et al. 1985), the proposed model accounts for the expected variation of densities between the different populations of meteoroids (Fig. 9, Section 2.9), which are more icy or more stony depending on their origin (e.g., Moorhead et al., 2017).

The density of the target can be taken as either the specific gravity or the bulk density of lunar regolith. The concept of bulk density includes porosity and is always smaller than the density of individual regolith particles. Thus, whereas a representative value of density for individual regolith grains is $\rho \approx 3 \text{ g cm}^{-3}$, which is used for all calculations, representative values for regolith bulk density are approximately 1.30 g cm^{-3} at the surface and 1.52 g cm^{-3} at a depth of 10 cm (Carrier III, 2005). However, the precise value of the target density adopted in the model seems to have only a small effect ($\sim 10\%$) in the model output as the total ejected mass falls off as $\rho^{-0.2}$ (Eq. 4.5).

The model approximates the size distribution of ejecta as the size distribution of lunar regolith particles (Section 2.5). It further extends the results from lunar samples to particles < 5 microns by using LADEE measurements.

The ejecta model for total mass is based upon Housen and Holsapple (2011). Comparison to the old Zook (1967) formula was provided (Section 3.1). Comparison to other formulas frequently used for the calculation of ejecta rates were not provided. Here we assess this approach.

According to the formula adopted, the total mass ejected by an impactor is given by Eq 2.18 and 4.1:

$$M_{>\nu} = C_4 m_p \left(\frac{\nu}{v_p \sin \alpha} \right)^{-3\mu} \left(\frac{\rho}{\rho_p} \right)^{1-3\nu}$$

where

$$C_4 = \frac{3k}{4\pi} C_1^{3\mu}$$

In these equations, v is the ejecta speed (minimum of 0.1 km/s considered), m_p is the mass of the primary impactor/projectile, v_p is its speed, and ρ_p is its density. The quantity α is the impact angle, measured from the local horizon, and ρ is the density of the regolith and ejected particles, which is assumed to be 3100 kg m^{-3} . The quantities $\mu = 0.4$, $\nu = 0.4$, $k = 0.3$, and $C_1 = 0.55$ are material-specific constants for sand-fly ash (see Table 3 of Housen and Holsapple, 2011). With the values adopted, $M \propto m_p v_p^{1.2}$

Another popular formula for the mass production rate is that of Koschny and Grun (2001):

$$M = C \cos^2 \alpha m_p^{\gamma_1} v_p^{2\gamma_2} = C \cos^2 \alpha m_p^{1.23} v_p^{2.46}$$

This formula was derived in laboratory experiments for impacts $v_p < 10 \text{ km/s}$, which are smaller than experienced on the lunar surface. It is evident that the Koschny and Grun (2001) formula is a more sensitive function of the projectile speed and will tend to accentuate the ejecta production from high speed impactors at the apex. Importantly, there is an additional dependence on projectile mass in the Koschny and Grun (2001) formulation that, albeit weak, $m_p^{0.23}$, provides a way to assess which formula should be used. Using a similar dynamical model to MEM, Pokorny et al. (2019) found that the ejecta production rate should be described as proportional to the mass of the projectile, $M \propto m_p v_p^{2.46}$ (i.e., $\gamma_1=1$ in the Koschny and Grun 2001 formula), in order for LADEE measurements to be consistent with the current constraints on the relative ratios of JFC, HTC and OCC particles as measured from radar at Earth. This finding follows from a segregation in the mass indices of the different populations arriving at Earth according to Pokorny et al. (2019). The velocity index was found to be uncertain and was studied only in the range 2-2.6. With the Kochny and Grun formula the total ejection rate seems to have exceeded LADEE by four orders of magnitude.

In conclusion, the LADEE data appear to be more consistent with the Housen and Holsapple (2001) formula over the Koschny and Grun (2001) formula, but at reduced yields.

Refs:

Carrier, D. (2005). The four things you need to know about the geotechnical properties of lunar soil. Lunar Geotechnical Institute, 2-9.

8.2 LROC Comparison

The LROC instrument has collected nearly half a million WAC images (100 meters per pixel) and 1 million NAC observations (meter-scale pixels) over illuminated terrain. With this extensive image library and additional observations collected during a series of extended science missions, LROC has a large catalog of temporal image pairs. These before and after image pairs have nearly identical lighting and viewing geometries and are separated in time by six months to almost the length of the mission. By systematically scanning these observations, newly formed surface features can be mapped and classified. To date, LROC has identified over 500 newly formed craters and 150,000 other surface changes. Many of these other surface changes are thought to be distal secondary impacts due to their proximity to newly formed craters.

In 2015, the LROC team published a manuscript documenting a newly formed 18-meter crater located with the help of an impact flash observed on 17 March 2013 by the Automated Lunar and Meteor Observatory (ALaMO) at NASA Marshall Space Flight Center (Suggs et al., 2014). Robinson and coauthors (2015) identified four distinct reflectance zones around the impact site: Proximal High Reflectance Zone (PHRZ), Proximal Low Reflectance Zone (PLRZ), Distal High Reflectance Zone (DHRZ), and Distal Low Reflectance Zone (DLRZ). Figure 1 highlights shows the extent of each zone by computing a ratio image of the after image (M1129645568L) and the before image (M183689789L). The blue outline in Figure 1a shows the outer extent of DLRZ, red line delimits outer boundary of DHRZ, orange polygon defines the outer limit of the PLRZ, and the PHRZ extends from the crater rim out to the green boundary. An enlargement of the top panel is shown in Figure 1b detailing the zones closer to the impact site. This work also documented 248 distal ejecta impacts creating a series of splotches that surrounded the impact site. Figure 2 displays a subset of these splotches (white arrows) exhibited herringbone patterns that pointed toward the impact site (direction of the black arrows).

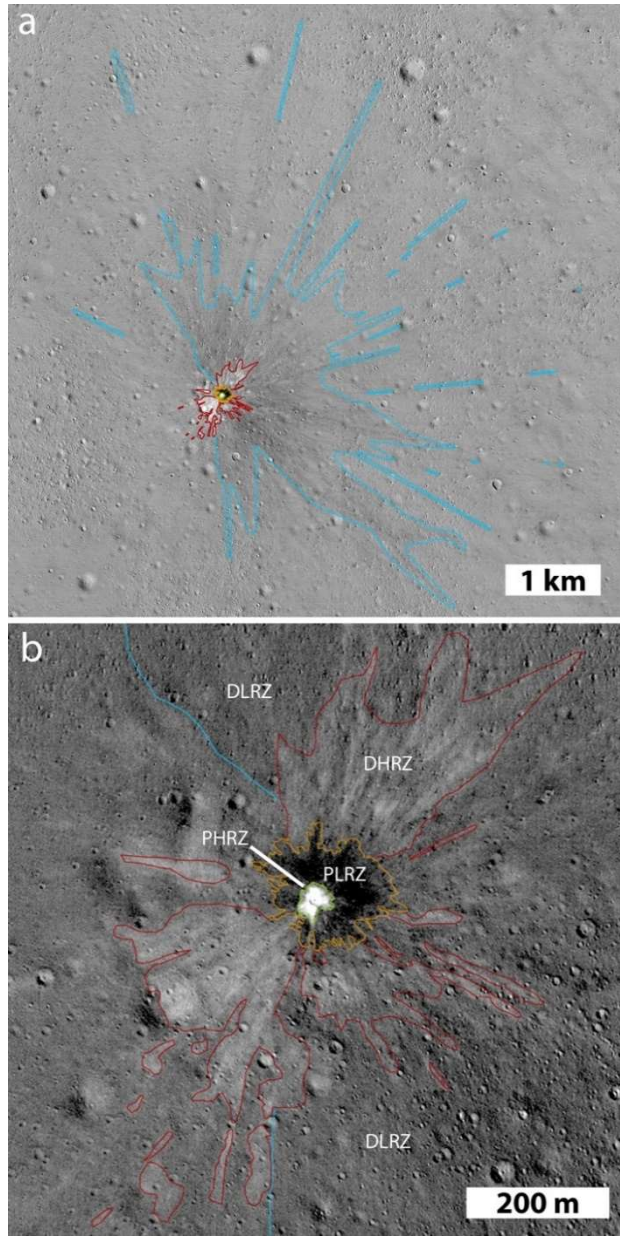


Figure 1: Temporal ratio image of an 18 m impact that formed on 17 March 2013. From Robinson et al. (2015).

Restricted distribution to NESC and designated team members until approved by the NRB.

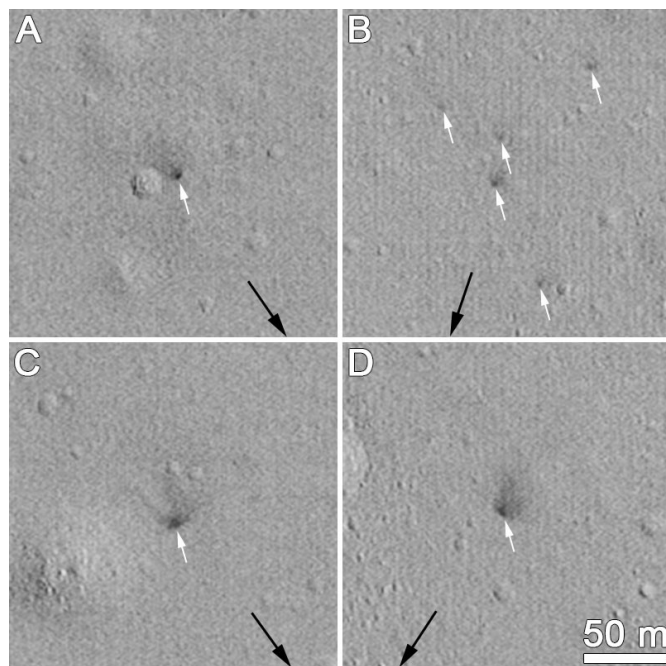


Figure 2: Secondary splotches (highlighted with white arrows) observed in temporal ratio images around the 17 March 2013 impact site.

Speyerer and coauthors (2016) examined 222 newly formed impact craters and 120,000 splotch like features in a follow-on study. With these additional craters, the study expanded upon the existence of the reflectance zones and proposed that the two distal zones result from impact jetting. Jetting occurs in the contact and compression phase of the impact process. This process occurs before the projectile is fully compressed and ends with the projectile halfway into the target ($t=D/2v$; D = projectile diameter, v = projectile velocity) (Melosh, 1989). While the mass ejected during jetting is small compared to the material removed during the excavation phase, the velocity profile is on the same order or even faster than the original projectile velocity (Vickery, 1993). Previous work indicates that this jetting phenomenon is more pronounced in oblique impacts. Jetted material is composed of a mixture of melted and vaporized rock – primarily from the impactor – that travels along the surface. Figure 3A-C shows temporal ratio images highlighting distal zones around a newly formed 19.5, 12, and 11 m crater, respectively. Image ratios (Figure 3D and 3E) also show the distal zones flowing around topographic features (small crater), which indicates that the jet indeed has a low ejection angle. Additionally, we find that these disturbances can cover large distances from the primary impact (up to 100 km for a 70m crater; **Figure 3F**) when the surrounding surface exhibits few topographic obstacles (i.e., lunar maria).

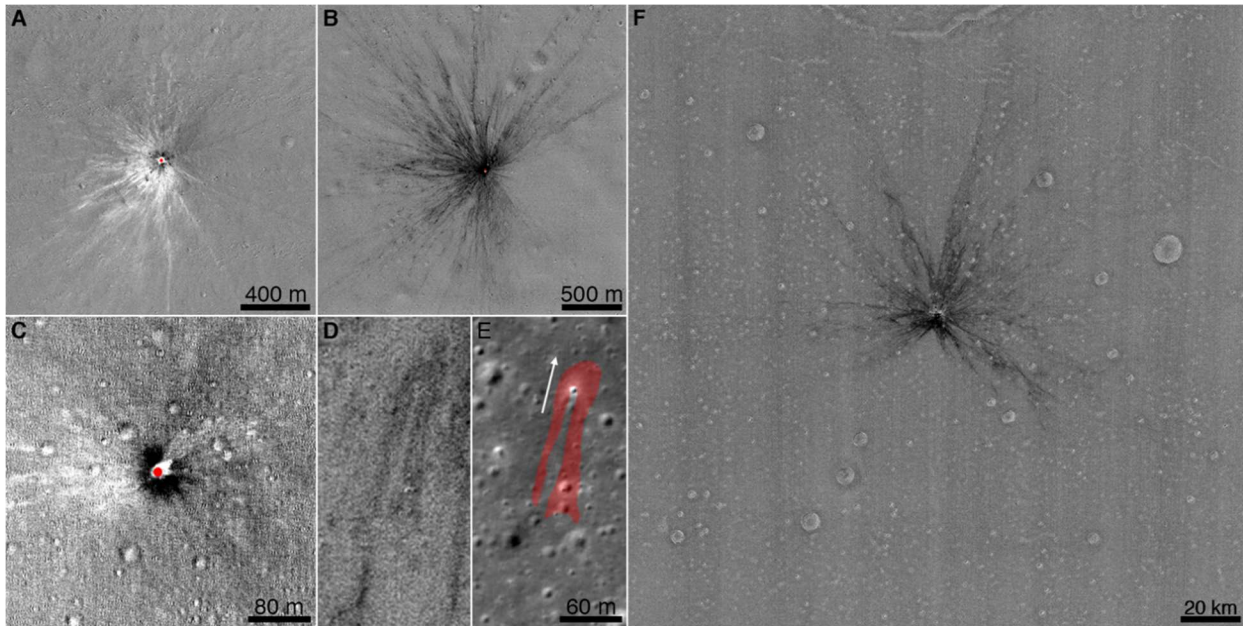


Figure 3: Series of temporal ratio image showing extent of distal zones around newly formed craters. The MeMoSeE model is a convenient tool to assess the average ejecta distribution during the excavation phase of the impact process. When modeling oblique impacts, the model accurately portrays the impact process by ejecting more material in the downrange direction and leaving an exclusion zone in the up-range direction of the impact site. Modification to the code could enable the modeling of an individual or a handful of impacts to further study the ejecta distribution around newly formed craters observed with LROC and help constrain the impactor's properties, such as the impact angle.

The MeMoSeE model estimates the number of particles impacting a surface as a function of impact angle (8 bins) and speed (3 bins). The table for the secondary statistics gathered for the nearside equatorial region (0°N 0°E) is reproduced in Table 1. Using the median particle size (0.072 mm; see section 3.4.2.2.1 of DSNE) along with speed and impact angle information, the crater size created by the ejected particles was estimated using the Holsapple scaling model and approximations (Housen and Holsapple, 2010; Holsapple, 1993). While these models typically are not used to assess impacts caused by low-speed projectiles, the equations provide a rough estimate of the secondary crater size (Table 2).

Table 1: Primary ejecta flux versus elevation and speed for 0°N and 0°E .

| Elevation | | | Speed | | |
|-----------|------|--------|------------------------------------|---------------------------|-----------------------------|
| PHI1 | PHI2 | PHIavg | 0.1-0.3 km/s avg=170 m/s | 0.3-1 km/s avg=535 m/s | 1-2.4 km/s avg=1.53 km/s |
| Degrees | | | Number Flux [$\#/m^2/\text{yr}$] | | |
| 0 | 10 | 4.98 | 2.75E-12 | 1.97E-12 | 3.32E-13 |
| 10 | 20 | 14.94 | 3.21E-07 | 1.57E-07 | 2.95E-08 |
| 20 | 30 | 24.90 | 2.02E-04 | 8.20E-05 | 1.10E-05 |
| 30 | 40 | 34.85 | 1.35E-02 | 5.10E-03 | 6.56E-04 |
| 40 | 50 | 44.78 | 2.35E-01 | 8.70E-02 | 1.13E-02 |
| 50 | 60 | 54.69 | 1.53E+00 | 6.00E-01 | 7.73E-02 |

Restricted distribution to NESC and designated team members until approved by the NRB.

| | | | | | |
|----|----|-------|----------|----------|----------|
| 60 | 70 | 64.54 | 4.37E+00 | 1.87E+00 | 2.70E-01 |
| 70 | 80 | 74.21 | 5.03E+00 | 2.78E+00 | 4.78E-01 |
| 80 | 90 | 82.93 | 1.25E+00 | 1.17E+00 | 2.55E-01 |

Table 2: Crater size estimated for each bin assuming a secondary particle size of 0.072 mm and the average impact elevation (PHIavg) and average speed associated with each bin.

| Elevation | | | Speed | | |
|-----------|------|--------|-----------------------------------|---------------------------|-----------------------------|
| PHI1 | PHI2 | PHIavg | 0.1-0.3 km/s avg=170 m/s | 0.3-1 km/s avg=535 m/s | 1-2.4 km/s avg=1.53 km/s |
| Degrees | | | Diameter of Secondary Crater [cm] | | |
| 0 | 10 | 4.98 | 0.11 | 0.17 | 0.26 |
| 10 | 20 | 14.94 | 0.17 | 0.27 | 0.41 |
| 20 | 30 | 24.90 | 0.21 | 0.33 | 0.50 |
| 30 | 40 | 34.85 | 0.23 | 0.37 | 0.56 |
| 40 | 50 | 44.78 | 0.25 | 0.40 | 0.61 |
| 50 | 60 | 54.69 | 0.27 | 0.42 | 0.65 |
| 60 | 70 | 64.54 | 0.28 | 0.44 | 0.67 |
| 70 | 80 | 74.21 | 0.29 | 0.45 | 0.69 |
| 80 | 90 | 82.93 | 0.29 | 0.46 | 0.70 |

Suppose each of these secondary impacts (Table 2) creates an ejecta blanket that extends two crater diameters away from the rim. In that case, we can execute a Monte Carlo model to estimate the resurfacing rate of the Moon and compare it to observations made by LROC and the secondary splotches observed in the temporal images. Speyerer et al. (2016) found that splotches down to 1 m in diameter had the potential to cover 99% of the Moon in 81,000 years. Using the secondary crater size estimates in Table 2 and the assumption that each impact modifies the surface within two crater diameters, we estimate a resurfacing rate of 78,000+- 1400 years, within 4% of the resurfacing estimates computed from LROC observations!

While these estimates are nearly in agreement, it should be noted that LROC observed secondary splotches that were 1.5 to as large as 30 m in diameter. None of the ejecta particles described in the MeMoSeE model could account for creating these significant disturbances. Speyerer et al. (2016) proposed that these splotches could be formed by a grouping of poorly consolidated regolith ejected in clumps. This method would imply that the splotches are created by many dozens to thousands of small particles modifying the surface and increasing the roughness of the top regolith layer and reducing the overall observed reflectance. This scenario would also not create a crater visible in LROC images, consistent with what was observed in temporal pairs. However, it is possible that small craters (<3 pixels across) form during these secondary impacts but are not observable from orbit with the current camera systems.

Finding 8: The model focuses on particles ejected during the excavation phase of the impact process and does not account for jetted material expelled away from the impact site at low angles to the target's surface and high velocities during the contact/compression phase.

Recommendation 8: Incorporate jetted material expelled during the impact contact/compression phase into future versions of the model.

Finding 9: The resurfacing rate (~80,000 years) caused by secondary impacts modeled with MeMoSeE agrees with statistics derived from temporal observations collected by the LROC NAC.

Finding 10: While the derived resurfacing rate is consistent with LROC measurements of secondary surface changes, the stochastic clustering of distal ejecta is not considered in the current model. LROC temporal image pairs (before/after observations) reveal secondary surface disturbances that are significantly larger (1 to 30 m in diameter) than the secondary impacts modeled in MeMoSeE (<0.01 m). These observed secondary features are likely the result of the clustering of many secondary particles that impact the surface.

Recommendation 9: Consider modifying the model to account for the clustering of secondary particles impacting the surface. This should not affect the average flux of secondary particles, however the risk to a surface asset may increase if impacted by multiple, closer packed particles.

Observation 4: With some code modifications, the model could help assess the distribution of secondaries around impact sites, particularly the distal ejecta identified in LROC images around newly formed impacts.

9.0 Section 3 – Propagation of the ejecta to the asset

One of the important aspects of the model is how the various ejecta models are put together to generate the flux at a position on the Moon. As this is a particularly important component of MeMoSeE, and it is difficult to isolate the mathematics of the flux calculations from the numerous other calculations, we need a tool to isolate these calculations and to compare with some sort of “truth”.

9.1 Monte Carlo approach

The easiest way to do this is to come up with a simplified version of the ejecta model, and to use a Monte Carlo technique to compute the fluxes on a lunar target. One simplification is to have the primary impactor flux isotropic over the Moon, and have the ejecta only have a single particle size that leave the crater isotropic in azimuth and a simple function for speed and zenith angle distributions.

The target on the surface of the Moon must be carefully considered in order to compute accurate and usable flux values. MeMoSeE uses a hemispherical target for flux calculations, but the simplest Monte Carlo target is a sphere with a given radius sitting on the surface of the Moon (Fig. 1). It presents its πr^2 cross sectional area to particles from any direction. That way, the cross-sectional area is easy to assess from any given ejecta direction as merely the number of particles that penetrate the sphere divided by the cross-sectional area.

Note that cross-sectional area of a target hemisphere useful for computing the flux is a function of the zenith angle of the impactor γ ,

$$A_{hemisphere} = \frac{\pi}{2} r^2 (1 + \cos \gamma)$$

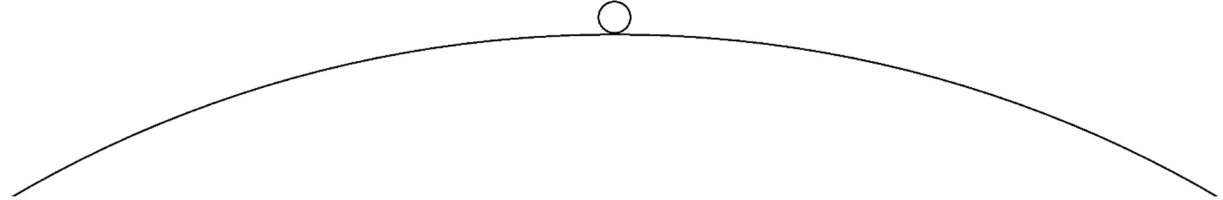


Figure 3-1 – for the Monte Carlo flux calculations, a virtual sphere of known radius is placed on the surface of the Moon. Flux is computed from the number of ejecta that penetrate the sphere.

The idealized flux is computed for the limit when the sphere on the surface of the Moon has a vanishingly small radius. However, for practical reasons, the sphere needs to be of sufficient size to record a nontrivial number of impacts. Ideally, as long as the radius of the sphere is much smaller than the radius of the Moon, the Monte Carlo flux should be accurate.

The Monte Carlo procedure is as follows:

1. The sphere (radius 500 m) is placed on the surface of the Moon
2. A primary impact site is randomly chosen on the surface of the Moon
3. A single ejecta particle is created, with randomized azimuth, zenith angle (based on the distribution to be tested), and speed (also based on the distribution to be tested)
4. The Kepler orbit for that ejecta particle is computed, and it is determined whether a particle intersects the sphere before it re-encounters the surface of the Moon
5. The conditions of that impactor are written to a file
6. The process is repeated at step 2 until a sufficient number of Monte Carlo runs have been completed

The total number of particles created is recorded, as this will be useful in determining flux. Note that the initial velocities of all particles created from a cratering event will be ascending from the surface of the Moon, but the zenith angles of particles hitting the sphere can be any value between 0° and 180°, with angles between 0° to 90° representing “descending from above” (case I), and those from 90° to 180° “ascending from below” (case II, see Fig. 2).

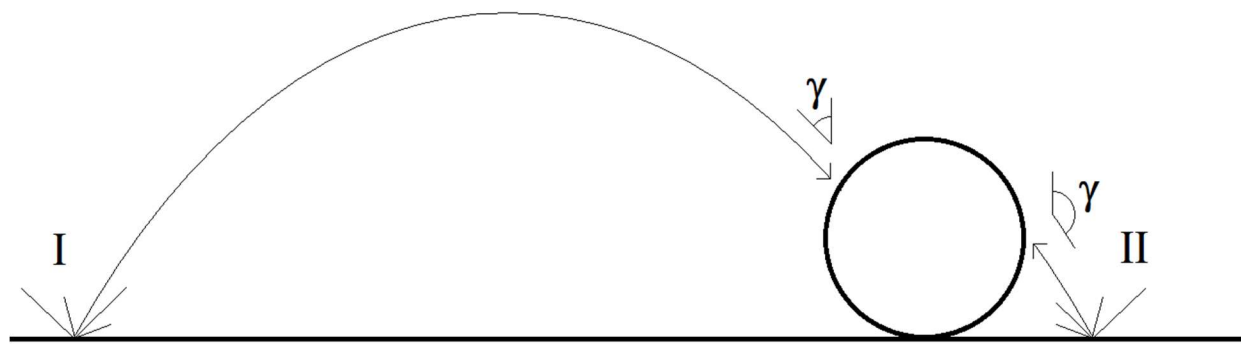


Figure 3-2 – There are two general cases of objects that hit the sphere; case I “descending” and case II “ascending”.

Restricted distribution to NESC and designated team members until approved by the NRB.

For the cases studied, the velocity distribution was that used in the model, with the speed distribution given by

$$D(v)dv \propto \left(\frac{v}{v_{min}}\right)^{-2.2} dv$$

With a maximum velocity equal to the escape velocity, and a minimum velocity set at 100 m/s.

As stated above, the azimuth distribution was randomized, but for the zenith angle γ distribution several different distributions were used.

The first (Case A) was a simple distribution that sheds light on the physics of this process

$$D(\gamma) \propto \sin \gamma \cos \gamma$$

The sine term is due to the solid angle, but the cosine term is to avoid large numbers of particles created horizontally.

The second test zenith angle distribution is the one used in the model

$$D(\gamma) \propto \sin \gamma (\cos \gamma)^\alpha (1 - \cos \gamma)^{1/\alpha}$$

Here again, the sine term is due to the solid angle. The α term determines the peak zenith angle: $\alpha = 1$ corresponds to peak zenith angles near 60° (Case B60), and $\alpha = \sqrt{1 + \sqrt{2}} \approx 1.554$ corresponds to peak zenith angles near 45° (Case B45).

Figure 3-3 shows a histogram of the distribution in zenith angle hitting the 500 m radius target sphere from Case A. The histogram represents the fraction of the 2×10^{11} total ejecta particles created. Note that a large number of impacts – roughly half – are ascending from the lunar surface (zenith angles $> 90^\circ$). Figure 3-4 shows the computed distribution of the zenith angle of ejecta as a function of the range of the parent impact. Note that most of the descending impacts are from distant primary impacts all over the Moon; some from the antipode or that travel more than halfway around the Moon before striking the sphere. But those that hit ascending from the lunar surface are actually from primary impacts near the sphere – within a few km (the actual distance is a function of the physical size and shape of the target, and should be considered illustrative that most of these impacts occur within a few radii of the target). A significant fraction of primary impacts are from “beneath” the sphere. While some of these are problematical (how can you have a primary impact if the sphere blocks it?), it does show the considerable contribution of near-field ejecta relative to the more conventional descending ejecta from primary impacts far away. Figure 3-5 shows the normalized distribution of these distances, broken out by whether the impacts are ascending or descending. ~15% of the total ejecta striking the sphere originate from primary impacts “beneath” the sphere, and ~70% originate from within a 10 km radius. Of the population that strike the target sphere “from below”, virtually all are from primary impacts very close to the target sphere (the simulation shows < 10 km, but that precise distance is a function of the shape and size of the 500 m radius sphere). Of the population that strike the target sphere “from above”, 40% come from the near field (< 10 km), and most ($> 85\%$) are from distances within 100 km. Only a small fraction come from distant parts of the Moon. There are probably some geometry effects from the finite size of the (500 m diameter) sphere used in the calculations that affect these precise ranges, but the general trend should be correct.

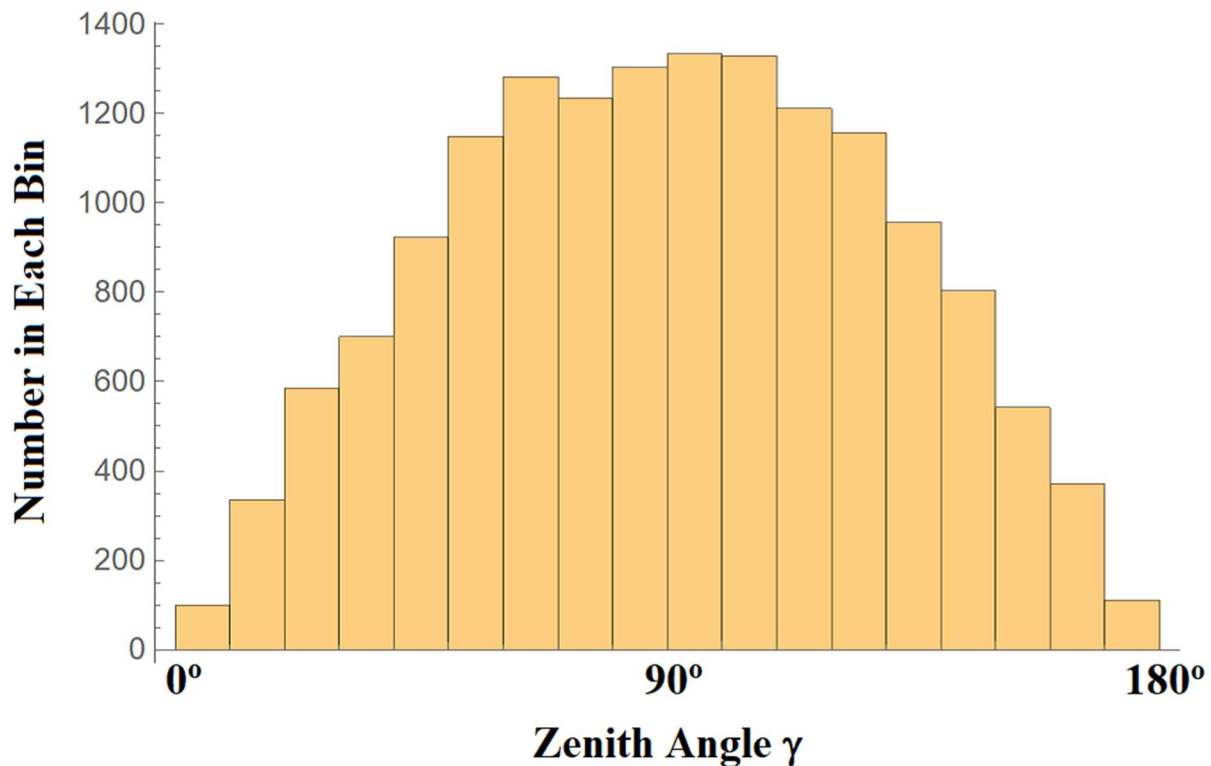


Figure 3-3 – The distribution in zenith angle of simulated ejecta hitting the 500 m sphere using the Case A direction distribution looks similar to an isotropic distribution.

Restricted distribution to NESC and designated team members until approved by the NRB.

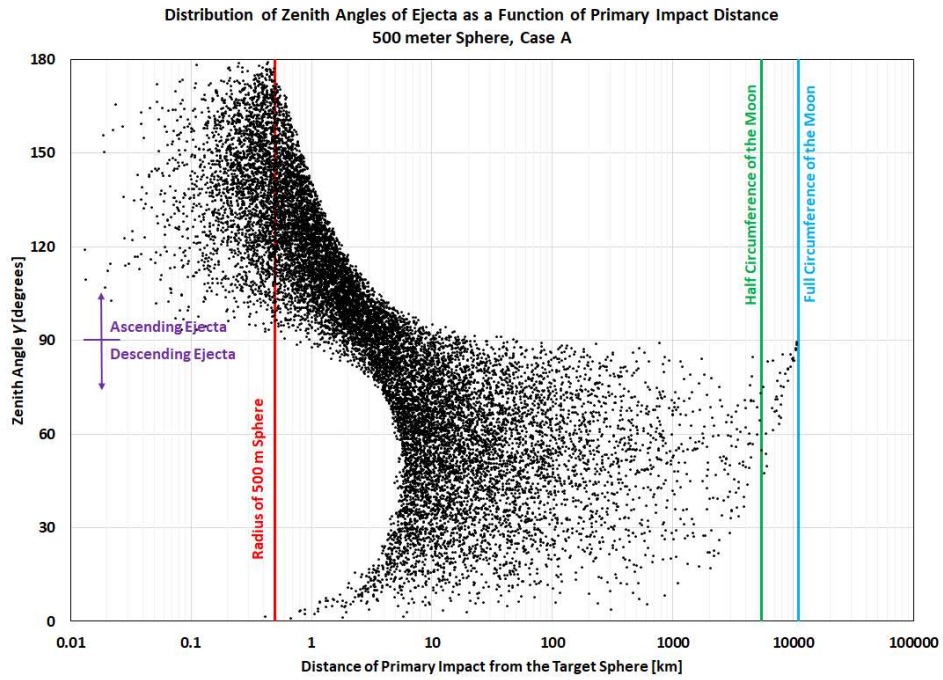


Figure 3-4 – A scatter plot of the relationship of the ejecta zenith angle to the range shows that most of the ascending ejecta impacts (zenith angles $>90^\circ$) are due to nearby primary impacts.

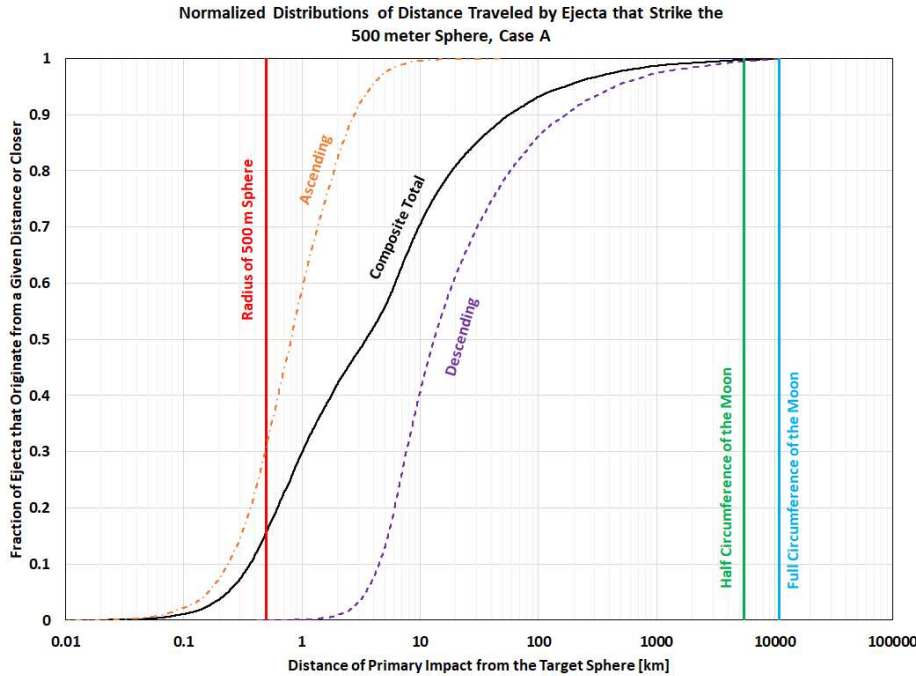


Figure 3-5 – The normalized cumulative distribution of the distance to the primary impact location shows that most of the descending ejecta originates within a few tens of km of the target, and most of the ascending ejecta from even closer.

The total number of ejecta simulated for this calculation was 2×10^{11} . Of these, 7610 hit the target from descending trajectories, which means for every ejecta particle created the probability of striking a target “from above” is approximately 4.8×10^{-14} per square meter of target. There

Restricted distribution to NESC and designated team members until approved by the NRB.

were 7812 that hit the target on ascending trajectories, with a probability of striking the target “from below” of 5.0×10^{-14} per square meter.

The actual numbers, of course, are dependent on the details of the simulation. To demonstrate this, Figure 3-6 shows the zenith angle histogram of Case B60. Note that the shape of the distribution changes, but the fraction of descending and ascending ejecta hitting the target shows that these are both of similar magnitude. Of a total of 10^{11} total ejecta particles created, 4936 hit on descending trajectories for a probability of 6.3×10^{-14} , and 5210 hit on ascending trajectories for a probability of 6.6×10^{-14} . Not these numbers are slightly higher than for Case A.

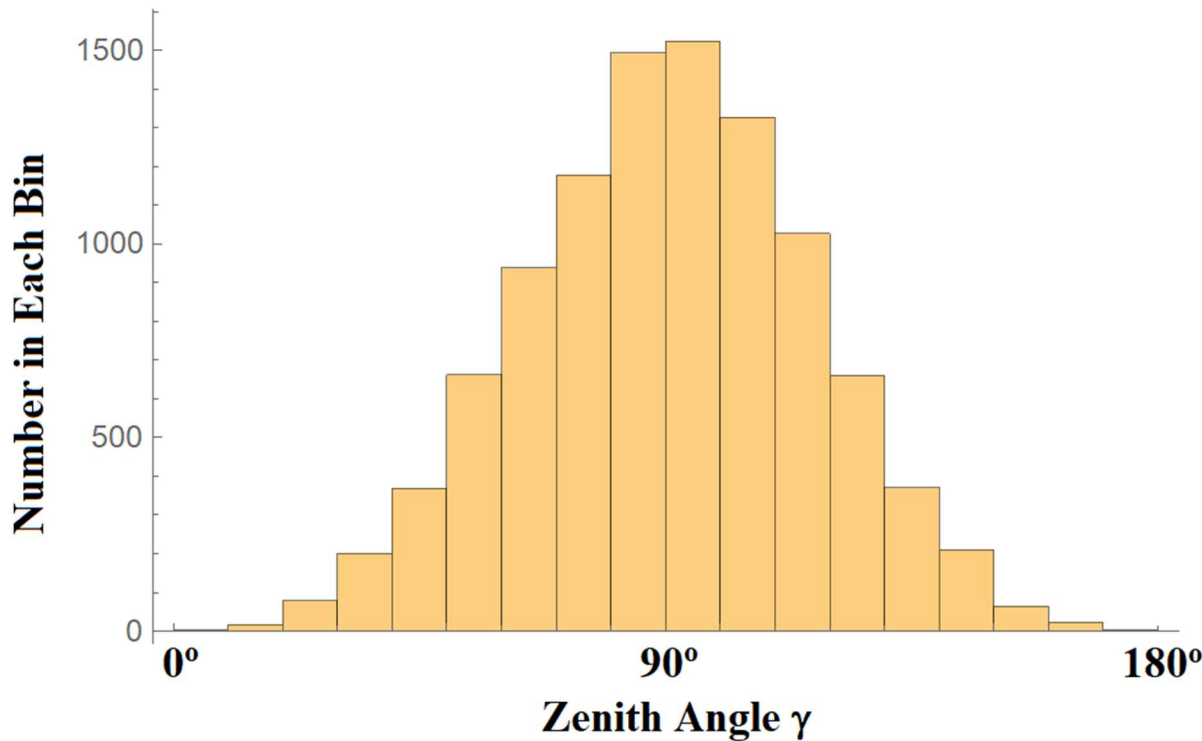


Figure 3-6 – The distribution in zenith angle of simulated ejecta hitting the 500 m sphere using the Case B60 direction distribution shows similar ascending/descending symmetry as in Case A.

For Case B45, Figure 3-7 shows similar symmetry for ascending and descending ejecta as the other cases, though the shape of the zenith angle distribution is different. Of a total of 10^{11} total ejecta particles created, 4311 hit on descending trajectories for a probability of 5.5×10^{-14} per square meter, and 4243 hit on ascending trajectories, for a probability of 5.4×10^{-14} per square meter.

While there are some differences, depending on the detailed ejecta model chosen, the trend is the same: similar probabilities of each ejecta particle hitting the target sphere, and approximately the same flux from ascending and descending trajectories.

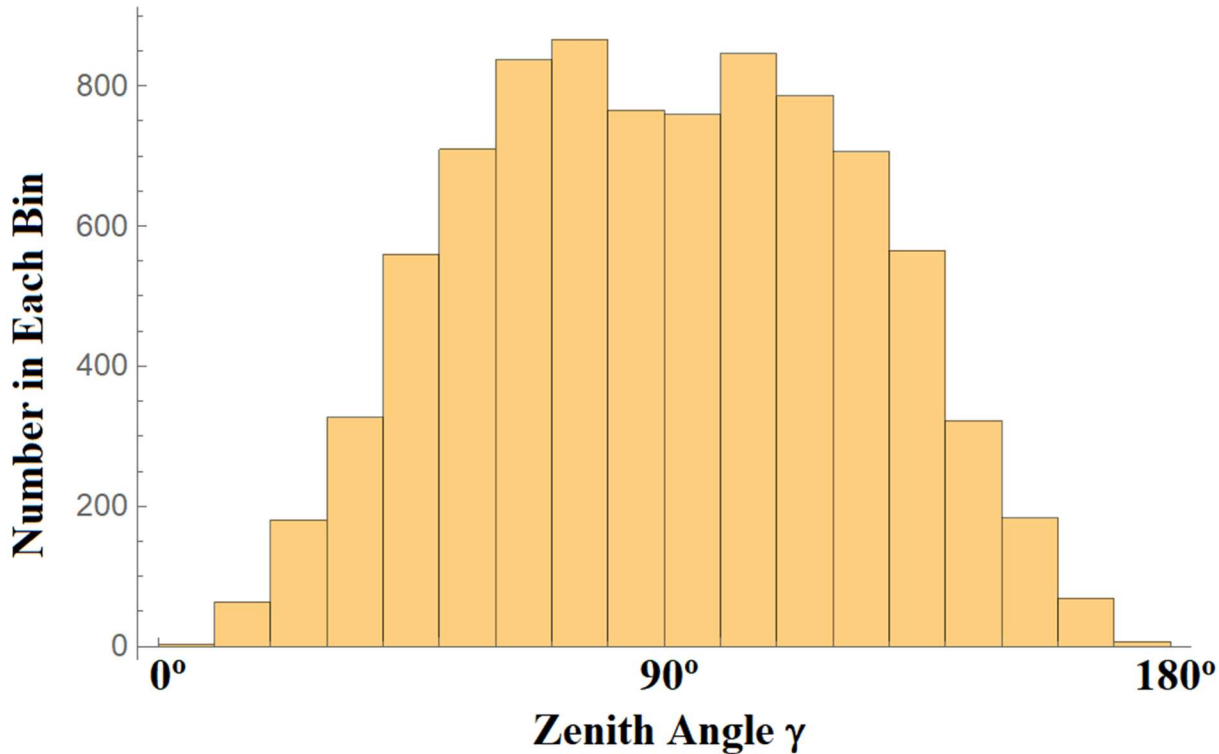


Figure 3-7 – The distribution in zenith angle of simulated ejecta hitting the 500 m sphere using the Case B45 direction distribution shows similar ascending/descending symmetry as in Case A and Case B60.

One other parameter to consider is that some ejecta may leave the impact crater with velocities exceeding the escape speed. These are typically ignored for descending ejecta, as they will not re-encounter the surface of the Moon. However, secondaries from the near field that exceed the escape velocity can still impact the target while on ascending trajectories, so limiting to speeds below the escape velocity may undercount that population hitting the target "from below".

As MeMoSeE only computes ejecta from impacts at least a minimum distance away, the ascending contribution is currently not taken into account. While the details of primary impacts that occur "below" the asset are not clear, it is clear that the ascending ejecta component can be of the same order of magnitude as the contribution from the more "traditional" long-distance descending ejecta. This means any complete ejecta model will ultimately need to include this component from primary impacts near the asset.

Note that the nature of the "long range" ejecta allows the model to treat the asset in a simple manner much like orbital debris or meteoroids; only taking into account the projected area of the surfaces. However, if the "short range" component is computed, the detailed geometry of the asset may become important; especially how the asset "shadows" primary impacts from "below" it. This may mean the assumption of a sphere may not be a good one for a particular flux calculation for a particular asset. Therefore, the results presented here are intended to show the general effects, not to be definitive computations of the relative contribution of the different types of ejecta.

Finding 11: Monte Carlo results have been used to test the flux algorithms used in MeMoSeE.

Recommendation 10: Use the Monte Carlo flux calculation results provided to verify model flux calculations.

Finding 12: The flux of ascending ejecta (i.e., striking the asset “from below”) generated by primary impacts close to the asset can be of a similar order of magnitude as the flux of descending ejecta (i.e., striking the asset “from above”) due to impacts farther away. However, the ascending population is not currently included in the model. The detailed effect of this ascending component of the flux on an asset is dependent on the detailed shape of that asset.

Recommendation 11: Include in future versions of the model effects of ascending ejecta from primary impacts that occur very close to the asset.

9.2 Stochastic Behavior of Primaries

This Monte Carlo method of simulating average numbers of impacts may help reveal the effects of another phenomenon. Primary impacts by larger impactors are rare, but primary impacts by smaller impactors are more common, and behave more like a constant “rain” over the lunar surface. Primary impacts that contribute a large probability to impact risk are those close to the asset. For very large impactors, the probability of hitting within a short distance of the asset during a finite time is very low, but the risk contribution of such rare events is very high. Using the distribution in Figure 3-5 for the descending population, it is possible to simulate a number of finite time intervals, and see the variability of the flux. Figures 8-10 show the results of such a simulation. Each case uses a different expectation value of the number of primary impacts.

The Monte Carlo procedure is as follows:

1. An integer number of primary impacts is generated from a Poisson sample of the expectation value (10.0, 100.0, and 1000.0)
2. Those primary impacts are distributed randomly around the Moon
3. For each primary impact, the probability of an ejecta impact on the sphere is computed using the curve in Figure 3-5
4. The probability is summed, and compared to the average value
5. The process is repeated at step 1 until a sufficient number of Monte Carlo runs have been completed

The figures show the distributions in these fluxes for each random pattern of primary impacts scaled to the mean value, considering only the descending component of the flux.

**Distribution of Flux Contributions for 1000
Monte Carlo runs where Expected Number
for Poisson Sample of Primary Impacts is 10.0**

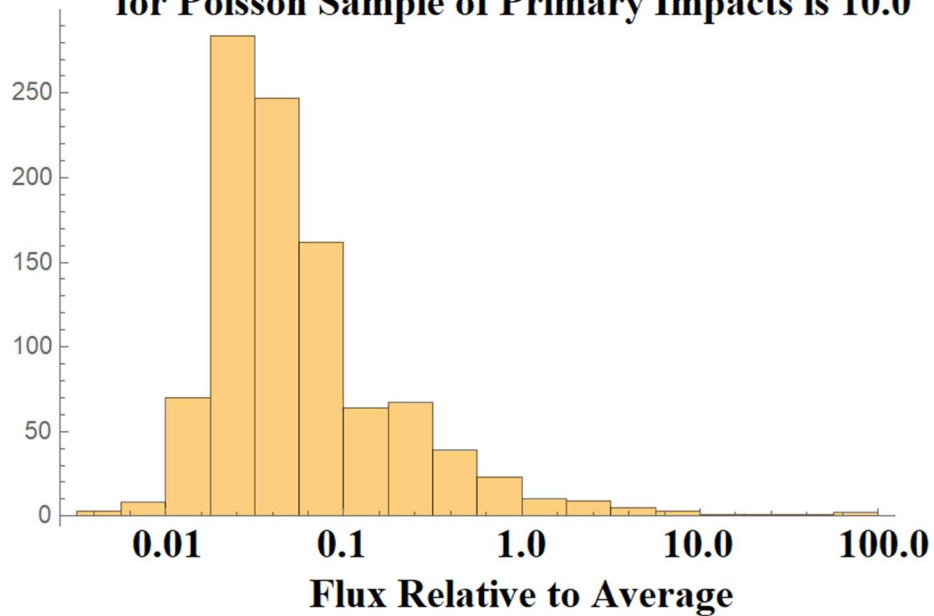


Figure 3-8 – The range in possible flux values scaled to the average descending flux for N primary impacts (chosen from the Poisson expectation value of 10.0) randomly distributed over the surface of the Moon.

Restricted distribution to NESC and designated team members until approved by the NRB.

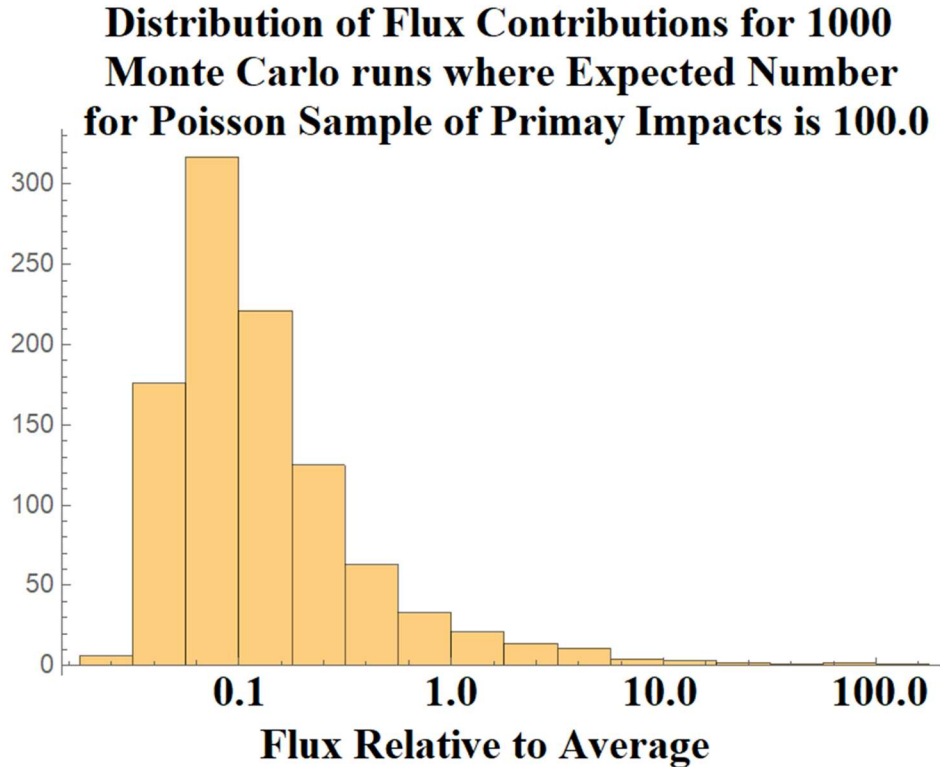
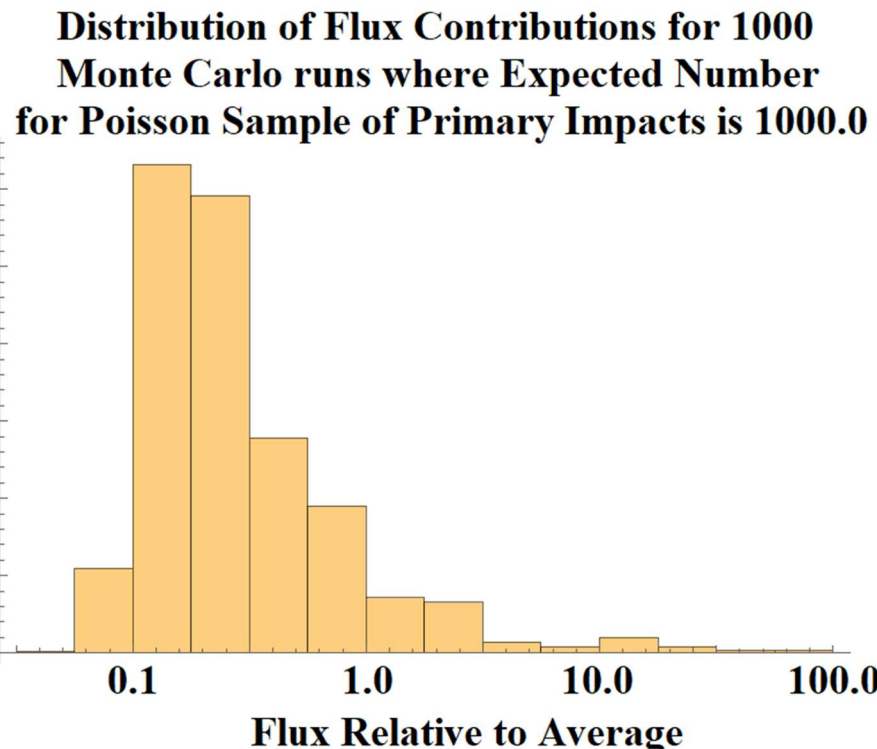


Figure 3-9 – The range in possible flux values scaled to the average descending flux for N primary impacts (chosen from the Poisson expectation value of 100.0) randomly distributed over the surface



of the Moon.

Figure 3-10 – The range in possible flux values scaled to the average descending flux for N primary impacts (chosen from the Poisson expectation value of 1000.0) randomly distributed over the surface of the Moon.

For the expectation value = 10.0 case, most of the sampled cases have flux lower than the computed average value, but about 3% of the cases have primary impacts near the asset, giving fluxes higher than the average value. This skewed distribution is affecting the mean values, with a tiny minority of cases giving flux much greater than the mean. For the expectation value = 100.0 case, about 6% of the cases have fluxes higher than the average. For the expectation value = 1000.0 case, about 10% of the cases have flux higher than the average.

The average flux is driven by these rare close impacts, but only a small fraction of cases have higher-than-average flux. Interestingly, the more expected total number of primary impacts, the higher the chance of higher-than-average flux and lower the probability of much lower-than-average flux. This dramatic variability is much more dynamic than what are typical for Poisson statistics. In fact, it is not clear that traditional average fluxes are the correct metric for computing risk in such a system. Note that the contribution of ascending flux from nearby primary impacts has not been included. The stochastic variability from this population is likely even more dynamic.

Finding 13: - The stochastic nature of the location of the primary impact flux, combined with the strong dependence of the flux on distance from the asset, mean that for any finite length of time, the actual number of secondaries impacting an asset may vary by several orders of magnitude from the mean value – much more than from standard Poisson sampling error. This stochastic nature of the flux appears to be the main driver in the uncertainty of the flux for any mission.

Recommendation 12: - Consider modifying the model to use Monte Carlo methods in addition to or in lieu of analytic methods to compute flux for future versions of the mode. This will allow the ability to compute the stochastic variability of the flux.

Recommendation 13: - The model output should have a way of calculating and reporting the stochastic variability of the flux. This might be shown by identifying the mean, median, and extreme cases (such as a 95% confidence level for maximum flux). The corresponding DSNE tables will need some breakdowns in probability for use in PRA analyses.

10.0 Risk Model Sensitivity

What are most important model assumptions that are driving the risk?

10.1 Variability in Time and Space

In addition to the stochastic behavior described above, the model includes the effects of variable primary impactor fluxes at different regions of the Moon and at different times. These will lead to different ejecta fluxes for different mission scenarios. This raises questions about which scenarios should be included in the DSNE tables.

Restricted distribution to NESC and designated team members until approved by the NRB.

Tests with the model indicate that temporal variations can vary up to a factor of 2. Different lunar latitudes/longitudes can give ejecta variations of up to a factor of 5, but averaging over local time, these will be reduced to more like a factor of 2.

However, these variations are mostly swamped by the stochastic behavior outlined above, where the random variability can be orders of magnitude. As with the stochastic variations, the tables in the DSNE will need to include “average” and “worse case” scenarios or split into percentiles. The time averages could include results from more “typical” missions (e.g., 7 days), rather than only a generic long-term average.

Finding 14: The ejecta flux can be non-uniform over different geographical regions of the Moon and at different times. Temporal variations are typically factors of 2 and variations with latitude/longitude are typically factors of 5, but closer to factors of 2 when averaged over local time. However, these variations are still small compared to stochastic variations.

Recommendation 14: Reconsider choosing what is the “average” location on the Moon vs choosing several example locations for the DSNE (e.g., at different longitudes or use 7-day intervals rather than average 19 years). The DSNE tables should include both nominal and worse-case scenarios.

10.2 Relative contribution of large versus small impactors

MeMoSeE uses the following equation from Table 1 of Housen and Holsapple (2011) to compute the total mass ejected at a speed of v or greater by an impacting particle:

$$M_{>v} = C_4 m_p \left(\frac{v}{v_p \sin \alpha} \right)^{-3\mu} \left(\frac{\rho}{\rho_p} \right)^{1-3\nu} \quad (1)$$

where

$$C_4 = \frac{3k}{4\pi} C_1^{3\mu} \quad (2)$$

In these equations, m_p is the mass of the projectile, v_p is its speed, and ρ_p is its density. The quantity α is the impact angle, measured from the local horizon, and ρ is the density of the regolith and ejected particles, which is assumed to be 3100 kg m^{-3} . The quantities $\mu = 0.4$, $\nu = 0.4$, $k = 0.3$, and $C_1 = 0.55$ are material-specific constants for sand-fly ash (see Table 3 of Housen and Holsapple, 2011); these values are not specified in DeStefano (2020b), but are mentioned in a separate presentation (DeStefano 2020a). Particles with speeds less than 0.1 km s^{-1} are not included in the proposed DSNE edits (DeStefano 2020c), and so we take this as the speed threshold for all calculations in this section. The total mass is partitioned into individual particles using a separate equation that does not depend on projectile properties.

From Equation 1, we see that the total mass of incoming particles is the key factor in determining the mass (and therefore number) of ejected particles. As discussed in Section 1, the flux of incoming meteoroids is obtained using version 3 of the Meteoroid Engineering Model (MEM; Moorhead, 2020a), which is proportional to equation A3 of Grün et al. (1985). The flux of larger

particles is derived from the flux of large objects onto the Earth's atmosphere (Brown et al., 2002), after accounting for the difference in gravitational focusing between the Earth and the Moon (Moorhead, 2020b). The two flux curves are presented in Figure 1; the solid blue curve presents the meteoroid flux obtained using MEM, while the dashed orange curve is the NEO flux derived from Brown et al. (2002).

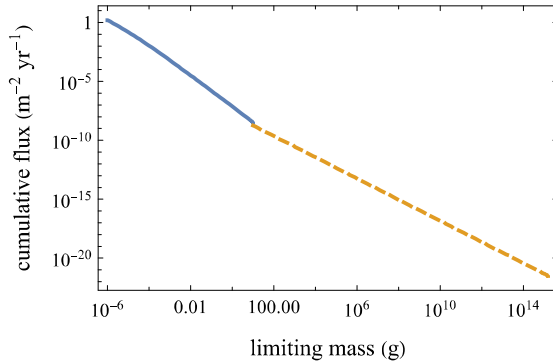


Figure 1 – The flux of particles of a given mass or larger onto the Moon.

While these sources provide the number flux of particles (f), we can obtain the total incoming mass flux in the mass range (m_1, m_2) as follows:

$$M_{1,2} = \left| \int_{m_1}^{m_2} \frac{df}{dm} m dm \right| \quad (3)$$

We take the absolute value of this integral so that either m_1 or m_2 can be greater. MeMoSeE includes primary impactors ranging from 110 µg (DeStefano, 2020c) in mass to 1000 m in diameter (which, for an assumed NEO density of 3000 kg m⁻³, corresponds to a mass of 1.57×10^{12} kg). In Figure 2, we present the mass flux of meteoroids lighter than $m_1 = 10$ g and NEOs heavier than $m_1 = 10$ g as a function of m_2 , highlighting MeMoSeE's chosen limits. Again, the flux corresponding to meteoroids appears as a solid blue line and that corresponding to NEO impacts appears as a dashed orange line. The mass shown is that of impacting objects that are between 10 g and the mass limit depicted on the ordinate axis. The nominal limits used by MeMoSeE are marked with solid black circles. The mass of a particle that hits the lunar surface once per year (on average) is marked with an open circle, and the mass of a particle that cannot produce ejecta larger than 5 mm in diameter is marked with an open triangle

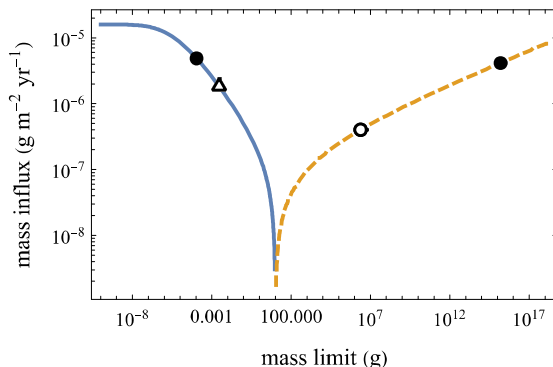


Figure 2 - Mass flux onto the lunar surface from meteoroid and NEO impacts.

Several pieces of information can be obtained from Figure 2. First, the current lower mass limit of 110 µg used by MeMoSeE does not capture most of the incoming meteoroid mass. If we

Restricted distribution to NESC and designated team members until approved by the NRB.

include arbitrarily small particles in our mass flux calculation, the total incoming mass would increase by 123%. However, these particles are unlikely to produce ejecta that are large enough to be hazardous. For large objects, the incoming mass continues to increase as we raise the upper mass limit. However, the upper mass limit used by MeMoSeE (1.57×10^{15} g) is substantially larger than the maximum NEO mass that impacts the Moon annually (2.38×10^6 g). If we were to restrict the mass influx calculation to those objects that hit the Moon at least once per year on average, we would obtain a mass flux that is about 40% lower than that obtained using MeMoSeE's nominal limits.

While Figure 2 characterizes the incoming mass, the amount of ejecta produced also depends on the impactors' speeds, densities, and impact angle. So long as projectile speed, mass, and density are not correlated in the models of incoming particles (which is true if we analyze the high- and low-density populations in MEM separately), we can estimate the total mass of ejecta produced as follows:

$$M_{>\nu} = C_4 M_p \left\langle \left(\frac{\nu}{v_p} \right)^{-3\mu} \right\rangle \left\langle \left(\frac{\rho}{\rho_p} \right)^{1-3\nu} \right\rangle \langle \sin^{3\mu} \alpha \rangle \quad (4)$$

We performed a MEM run using a “trajectory” in which the state vectors traced the position and motion of points on the lunar surface. The outputs provide us with the speed and density distribution of two populations (high- and low-density) of meteoroids striking the Moon. The NEO speed distribution is taken from Moorhead (2020b) and the density is assumed to be 3000 kg m^{-3} , following Brown et al. (2002) and DeStefano (2020b).

For both meteoroids and NEOs, we compute the angular term as:

$$\langle \sin^{3\mu} \alpha \rangle = \frac{2\pi \int_0^{\frac{\pi}{2}} \cos^{3\mu} \phi \cdot \cos \phi \sin \phi}{2\pi \int_0^{\frac{\pi}{2}} \cos \phi \sin \phi} = \frac{5}{8} \quad (5)$$

where $\phi = \frac{\pi}{2} - \alpha$ is the central angle between the impactor's sub-radiant point and a given location on the Moon. This gives us the the impact angle raised to the power of 3μ , averaged over the entire lunar surface and expressed relative to the incoming flux. Figure 3 presents the results of our ejected mass calculation for both meteoroid (solid blue) and NEO (dashed orange) impacts. The mass shown is that produced by impacting objects that are between 10 g and the mass limit depicted on the ordinate axis. The nominal limits used by MeMoSeE are marked with solid black circles. The mass of a particle that hits the lunar surface once per year (on average) is marked with an open circle, and the mass of a particle that cannot produce ejecta larger than 5 mm in diameter is marked with an open triangle

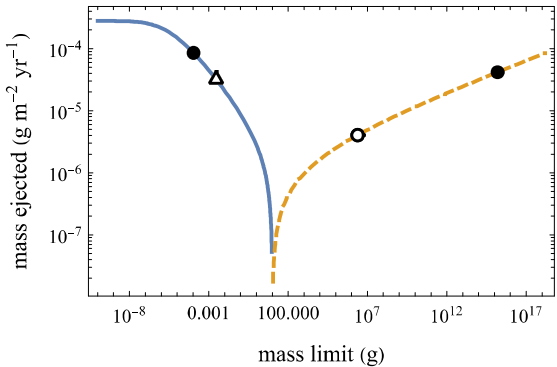


Figure 3 – The mass of particles ejected from the lunar surface due to meteoroid and NEO impacts.

It is apparent in Figure 3 that the mass of the ejected particles exceeds that of the primary impactors by an order of magnitude. This factor depends on the speed and density distribution of the incoming particles; the comparatively slow-moving NEOs excavate 10 times as much mass as impacts the Moon, while the very fast, low-density meteoroid population excavates nearly 20 times their mass.

More importantly, we can now assess the relative importance of meteoroids and NEOs in ejecta production. Using MeMoSeE’s nominal limits of $110 \mu\text{g}$ and $1.57 \times 10^{12} \text{ kg}$, we find that meteoroids are responsible for 54% of ejected particles. If particles larger than 2400 kg (i.e., those too large to impact the Moon each year) are excluded, the total ejected mass is 30% lower and 95% of it is produced by meteoroid impacts. Thus, the current upper mass limit for NEOs is conservative, at least on average, but the degree of conservatism is modest.

MeMoSeE does not appear to truncate the ejecta particle size distribution depending on the primary impactor size; instead, it allows small impacts to produce large particles. According to DeStefano (2020b), the fraction of ejected particles larger than a given size, x , is:

$$P_{>x} = e^{-\frac{1}{ax^b+cx^d}} \quad (7)$$

where x must be in units of mm and the constants are $a = 0.0548$, $b = -1.015$, $c = 0.337$, and $d = -0.2518$ (DeStefano, 2020b). No upper limit is incorporated into this equation (which is Equation 2.7 of DeStefano, 2020b), but an upper limit of 10 mm is used to normalize the PDF (Equation 2.8 of DeStefano, 2020b). Note that Equation (7) contains no dependence on any impactor properties or on the total amount of ejecta produced. Thus, according to MeMoSeE, 1.43% of the mass ejected by any impact above the 0.1 km s^{-1} minimum speed will also be larger than 5 mm in diameter, regardless of the size of the impactor.

If we include arbitrarily small impactors in our ejected mass calculation, we will increase the total ejected mass by 153%; note that this increase is larger than the 123% percent increase we calculated for the total *incoming* mass. If the size distribution of ejected particles is independent of the incoming particle mass, this would also increase the total quantity of hazardous ejecta. However, conservation of energy dictates that the largest ejecta particle that can be lifted by an incoming dust particle is:

$$m_e = m_p \frac{v_p^2}{v_e^2} \quad (6)$$

where m_p is the mass of the incoming particle, v_p is its speed, and v_e is the speed of the ejected particle. As discussed elsewhere (see Section 5.5), ejected particles 5-10 mm in diameter are capable of damaging manmade assets. If we set $m_e = 0.2$ g (the mass of a 5-mm-diameter particle with a density of 3100 kg m^{-3}), $v_p = 70 \text{ km s}^{-1}$, and recall that $v_e = 0.1 \text{ km s}^{-1}$, then $m_p = 4.1 \times 10^{-7}$ g, which is much smaller than MeMoSeE's lower limit. This assumes that the collision is completely inelastic.

However, if we instead assume that the mass of the largest particle is instead constrained by Equation (1), an ejected particle of 0.2 g then corresponds to an impactor mass of 2.9 milligrams, assuming a normal impact and that the impactor belongs to the low-density population in MEM; this mass is marked with an open triangle in Figures 2 and 3. This is quite a bit larger than 110 μg mass limit used by MeMoSeE and indicates that the model may be overconservative in attributing part of the mass ejected by smaller particles to the hazardous ejecta flux.

Thus, if the maximum particle size is limited by the conservation of kinetic energy, MeMoSeE may be underestimating the quantity of hazardous ejecta (by more than a factor of 2) by not considering particles smaller than 110 μg . If the maximum particle size is instead limited by Equation 1, then MeMoSeE is overestimating the quantity of hazardous ejecta by a factor of 3-4.

Finally, we note that we have interpreted references to “size” in DeStefano (2020b) and DeStefano (2020c) as the diameter of a spherical particle. If these sizes are instead radii or some other measure, some of the numbers in this section will change.

Finding 15: By including NEO sizes that rarely impact the Moon, the model may be overconservative in computing the quantity of ejecta produced by these objects in a typical year.

Recommendation 15: Limit the maximum size of primary impactors that are computed to contribute to ejecta in the model. One practical way to limit maximum projectile size is to identify the size of impactor that has a 1% chance of hitting the Moon during a nominal mission time. For a 10-year lunar base mission, this corresponds to a mean time between impacts of 1000 years. Alternatively, a Monte Carlo analysis with the full range of possible sizes might capture this effect without artificially limiting impactor size.

Finding 16: Assuming the mass of the largest particle ejected by an impact cannot exceed the total ejected mass predicted by the Housen and Holsapple (2011) equations, then the model may produce estimates of the hazardous ejecta flux that are a factor of 3-4 too high.

Recommendation 16: Consider placing an upper limit on the ejected particle size that is determined using conservation of energy and/or the ejecta mass.

10.3 Sporadic Versus Shower Meteoroid Contribution to the Ejecta Flux

By using MEM, a sporadic meteoroid model, to compute the flux of incoming meteoroids, MeMoSeE excludes meteor showers from the impactor population. This mimics the approach

taken by the Meteoroid Environment Office, in which sporadic meteoroids are included in engineering models, and any short term enhancements in the flux produced by meteor showers are provided separately in “forecasts.” The reasoning behind this approach is that meteor showers produce a small fraction (roughly a few percent) of hazardous particles on average, and thus do not merit inclusion in MEM, but can occasionally produce short-term enhancements of the flux that can be relevant during short periods of increased vulnerability, such as space walks.

However, meteor showers tend to be more heavily skewed toward large particles than the sporadic complex. Thus, it is possible that while showers contribute only a small portion of the *number* flux of meteoroids, they could contribute a more substantial fraction of the mass flux. To test this, we used an existing estimate of the mass flux of the Geminid meteor shower computed in Blaauw (2017). Table 2 of Blaauw (2017) gives this flux as 9.1×10^{-4} g km⁻² hr⁻¹ when the largest particles considered have a mass of 1 kg. After performing a unit conversion and dividing by 4 to convert this to the flux per unit lunar surface area, we obtain a value of 2.0×10^{-6} g m⁻² yr⁻¹ at the time of the shower’s peak. This is 22% of the nominal mass influx. If we use a Geminid speed of 35 km s⁻¹ and density of 2600 kg m⁻³ (Borovička et al., 2010), we obtain a mass production rate of 4.8×10^{-5} g m⁻² yr⁻¹, which is 37% of the nominal rate. Thus, at the time of peak activity, the Geminids could substantially increase the ejecta production rate.

Blaauw (2017) also provides Geminid fluences (e.g., 271 g km⁻²), which we can use to compute the contribution of the Geminids when averaged over the course of a year (6.8×10^{-8} g m⁻² yr⁻¹). Thus, on average, the Geminids constitute 0.7% of the incoming mass and produce 1.3% of the ejected mass. These calculations do depend on the largest Geminid considered. If, for instance, we include Geminids as large as 100 kg in mass, all Geminid rates presented here will be a factor of 4 larger (Blaauw, 2017).

The small contribution of the Geminid stream to the overall ejecta production rate justifies their exclusion from an average environment description. The Geminids produce the greatest flux of hazardous meteoroids in a typical year (Moorhead et al., 2019) and have produced both large numbers of lunar impact flashes and spikes in lunar impact ejecta measured by LDEX (Szalay et al., 2018). If they are not capable of raising the average ejecta production rate by more than a few percent, it is not likely that any other shower will.

10.4 Effect of Depth of Excavation on the Soil Size Distribution Ejected from the Crater

MeMoSeE assumes that comminution and agglutination in a single sporadic or NEO impact is sufficiently small to leave the regolith particle distribution unchanged, hence the in-situ soil size distribution is the distribution of ejecta particle sizes.

The lunar regolith constitutes the uppermost ten meters of the maria and the upper most thirty meters of the lunar highlands. Sufficiently energetic sporadic meteoroids and NEOs will punch through the regolith into material with a different size distribution and launch that material as ejecta. Our knowledge of the layers below the regolith comes from seismic studies. Figure 10.4-1 is a summary of the suspected layering based on sound speed measurements. (ref. 1)

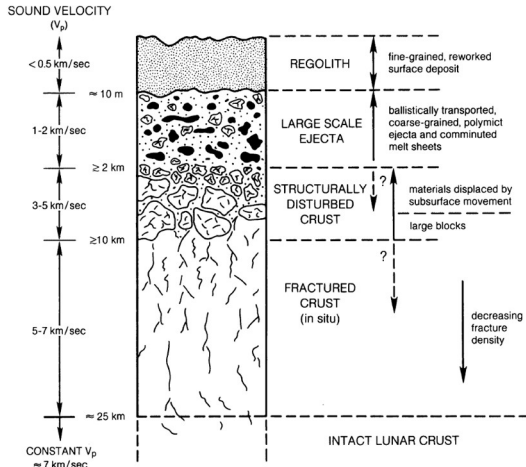


Figure 10.4-1 Schematic cross-section illustrating the idealized effect of large-scale crater on the structure of the upper lunar crust (ref. 1)

The material between 10-m and 2-km depth has a sound speed more than 4 times larger than the regolith sound speed indicating larger particles and less porosity. However, the authors are unaware of any estimates of the particle size distribution for these depths.

What follows in subsection 10.4.1 is an overview of Apollo regolith particle size distribution measurements and how they vary between the Apollo sites. Subsection 10.4.2 is an estimate of the effect of the site to site variations on the lunar ejecta flux environment. Subsection 10.4.3 is an overview of the lunar crater dimension scaling and Subsection 10.4.4 uses the dimension scaling to estimate the portion of the lunar ejecta flux calculation that is uncertain from the unknown size distribution for depths larger than 10-m.

10.4.1 Lunar regolith size distribution

Figure 10.4-2 shows the distribution of particle sizes measured from four Apollo samples.

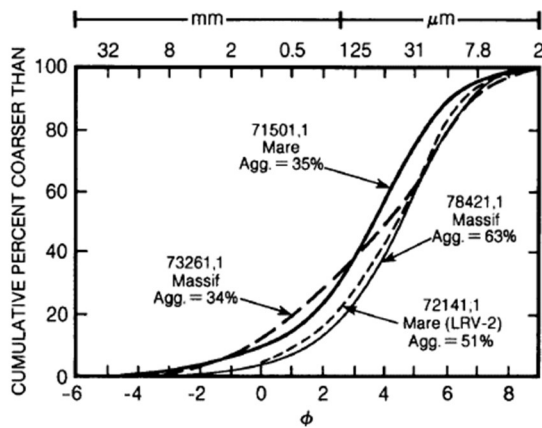


Figure 10.4-2 Cumulative size-frequency diagram for typical lunar surface soil samples. (ref. 1)

The parameter ϕ (called the Krumbein phi scale, ref. 2) is defined as

$$\phi = -\log_2(d \text{ in mm})$$

The corresponding diameters are listed across the top of Figure 10.4-2. The regolith particle sizes are typically distributed with a normal probability density,

$$D(d) = \frac{1}{\sqrt{2\pi}\sigma} \exp[-(\varphi - M)^2/(2\sigma^2)]$$

Where M is the mean grain size and σ is the standard deviation.

A number of researchers have measured the parameters M and σ for various Apollo samples and have characterized the sample ordered pairs (M , σ) as mature, submature and immature as shown in Figure 10.4-3.

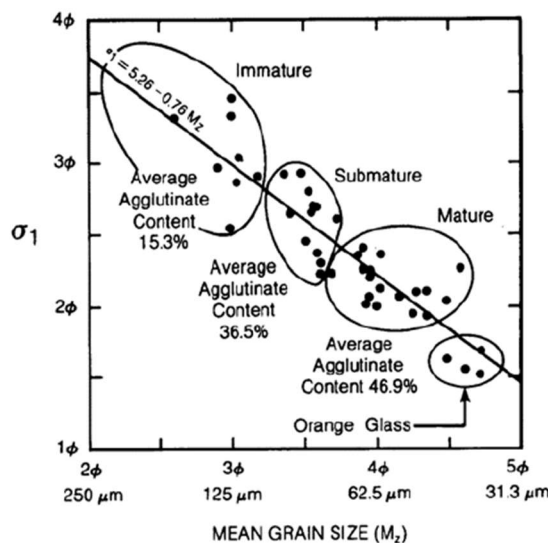


Figure 10.4-3 The relationship between grain size, sorting, and agglutinate content for 42 Apollo 17 soils (ref. 3 as cited by ref. 1)

Maturity is a quantity roughly equivalent to age. Lunar soils change significantly as they develop over time, and a highly mature soil has the largest degree of comminution and melting. (ref. 1) Thus one expects that the smallest regolith depths have the smallest mean grain size due to the large number of small impacts over time. Furthermore, one expects that the largest regolith depths have the largest mean grain size due to the smaller number of impacts that can penetrate to 10-m depth.

However, the Apollo core samples (60-cm to 3-m core samples) showed no clear trend of change in mean grain size with depth. Reference 1 concluded that

In summary, the analysis of regolith core samples has shown that regolith properties vary in a complex and not entirely predictable way with depth. A trend to coarser-grained samples with depth is present in some of the cores (e.g., Apollo 16), but there are exceptions (e.g. Luna 24).

MeMoSeE uses the soils size distribution from Carrier (2003). Carrier fit 4,500 points from 350 particle size analyses. These soil samples were obtained from seven landing sites on the Moon: Apollo 11, 12, 14, 15, 16, and 17; and Luna 24. Carrier recommended one soil size distribution, plotted as the gold solid curve on the righthand side of Figure 10.4-4. Note that this curve is close to the submature curve from ref. 1 (center filled circle on the righthand side of Figure 10.4-

4). Carrier also plotted plus and minus one standard deviations. These are plotted in Figure 5.4-4 as the gold broken lines. These curves enclose the mature soil distributions, except at the largest particle diameters. The immature soil size distribution lies outside one standard deviation from Carrier's fit.

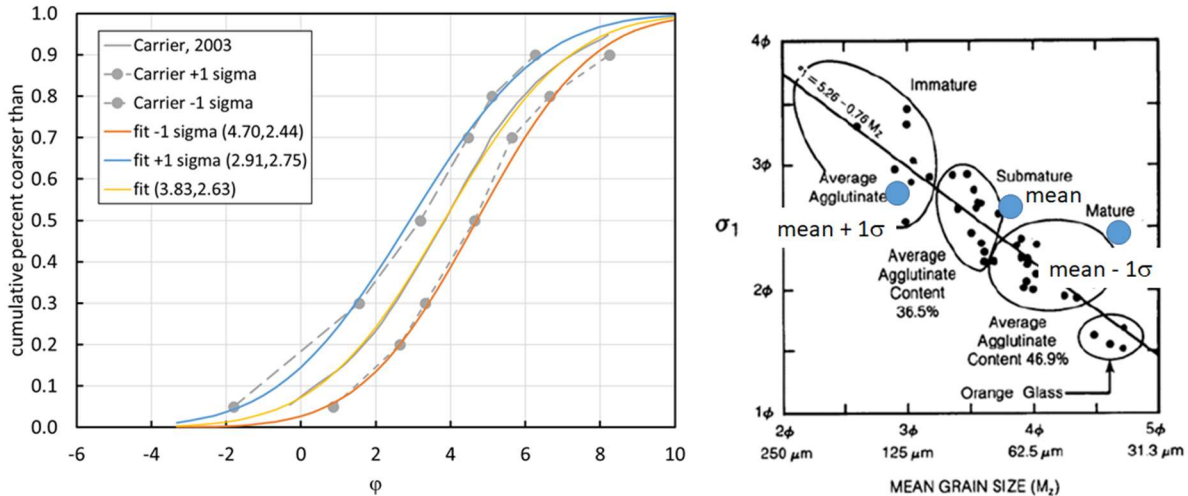


Figure 5.4-4 Comparison of soil size distributions

An (M, σ) pair of $(2.91, 2.75)$ provides a reasonable fit to the upper Carrier distribution and a pair of $(4.70, 2.44)$ provides a reasonable fit to the largest size soil particles in the lower Carrier distribution.

Finding 17: The model uses a soil size distribution characteristic of a single submature soil.

10.4.2 Effect of lunar regolith size distribution on the ejecta flux

The MeMoSeE procedure of using the same size distribution for all depths is as good as any other because there is no clear trend of change in mean grain size with depth. However, the Apollo core samples show a range of size distribution parameters, hence a sensitivity study is called for. This section is a preliminary sensitivity analysis using a simplified analysis that can be used as a verification artifact for the MeMoSeE analysis.

The sensitivity analysis assumes the following

1. The moon is a flat surface
2. No contribution by NEOs
3. Sporadics impact uniformly across the surface
4. All sporadics impact normal to the lunar surface
5. All sporadics impact at 20.3 km/s
6. The flux of sporadics onto the lunar surface is equal to the Grun flux onto a randomly tumbling flat sheet
7. All ejecta is launched at 45 degrees
8. The soil-particle density is 3100 kg/m^3
9. The soil bulk density is 1500 kg/m^3

Restricted distribution to NESC and designated team members until approved by the NRB.

10. Housen's ejecta mass as function of ejection speed cumulative distribution (with a coefficient of 0.018 and a slope of -1.23, the values for dry soils such as dry sand, lunar regolith and dry terrestrial desert alluvium, ref. 5)

Figure 10.4-4 is the plot of the calculated variation in flux with soil size distribution parameters.

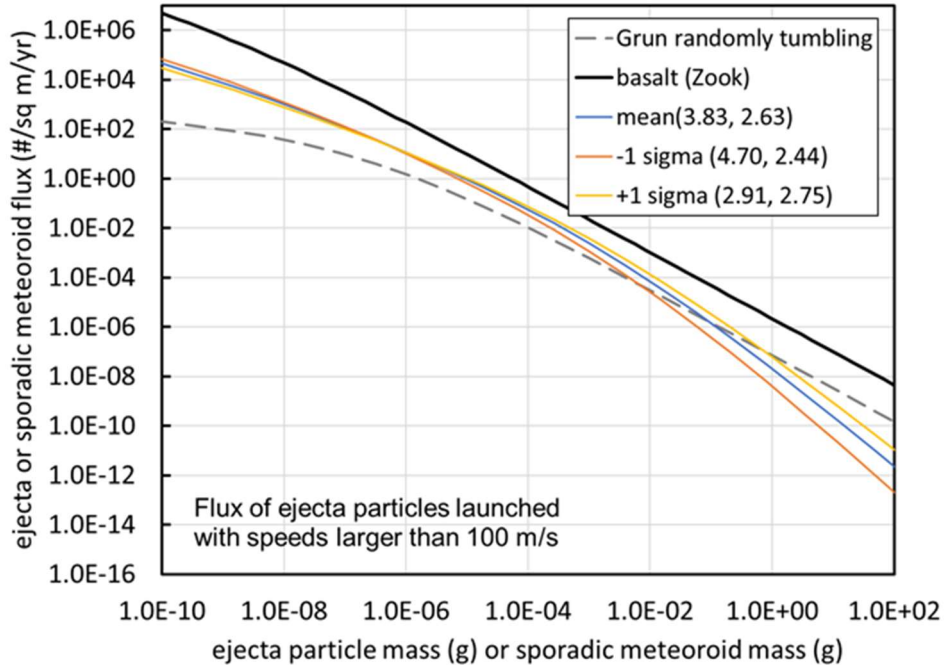


Figure 10.4-4 Ejecta flux distribution sensitivity to soil size distribution parameters

The plotted Grun flux is the flux on a randomly tumbling flat sheet. The ejecta flux is the flux through an upwards facing flat sheet lying on the lunar surface. The solid black curve used the Gault and Shoemaker ejecta size relation and ejecta speed relation for basalt cratering. This curve should match the NASA SP-8013 ejecta model when summing all three speed bins.

The ordered pairs next to the mean and plus or minus one sigma legend entries list the mean and standard deviation (M, σ) of the soil size distribution.

Figure 10.4-4 shows that the ejecta flux relation is insensitive to the soil size distribution for ejecta particle masses less than 10 micrograms (i.e., diameters less than 183 microns). However, at the sizes of interest to spacecraft protection (1-mm to 4.5-mm, or 2-mg to 150-mg) the minus one sigma flux is a factor of 0.48 to 0.24 smaller than the mean and the plus one sigma flux is a factor 1.6 to 2.6 larger than the mean. While perhaps not the largest uncertainty in the analysis, there appears to be a number of these smaller factors that should be accumulated to determine a worst-case flux.

Finding 18: Using the observed regolith particle size distribution instead of the average value used by the model results in an increase in ejecta flux by a factor of 1.6 to 4 for the sizes of most interest to the HLS design.

Recommendation 17: Perform a sensitivity study varying the soil size distribution parameters over the range of measured soil size distributions of the Apollo soil samples.

10.4.3 Crater dimension scaling

Holsapple's crater dimension scaling relations (ref. 6) are the basis of the present estimate of the maximum depth from which ejecta originates during an impact by sporadic meteoroids. Holsapple's crater volume relation for simple craters is

$$\pi_V = K_1 \left\{ \pi_2 \left(\frac{\rho}{\delta} \right)^{\frac{6\nu-2-\mu}{3\mu}} + \left[K_2 \pi_3 \left(\frac{\rho}{\delta} \right)^{\frac{6\nu-2}{3\mu}} \right]^{\frac{2+\mu}{2}} \right\}^{\frac{-3\mu}{2+\mu}},$$

where,

$$\begin{aligned}\pi_V &= \frac{\rho V}{m} \\ \pi_2 &= \frac{ga}{U^2} \\ \pi_3 &= \frac{Y}{\rho U^2}\end{aligned}$$

The variable V is the excavation crater volume, ρ is the lunar regolith bulk mass density, m is the impacting meteoroid mass, a is the impacting meteoroid radius, δ is the impacting meteoroid bulk mass density, U is the impact speed, Y is the lunar regolith strength.

Figure 10.4-5 illustrates the cross section of a simple crater.

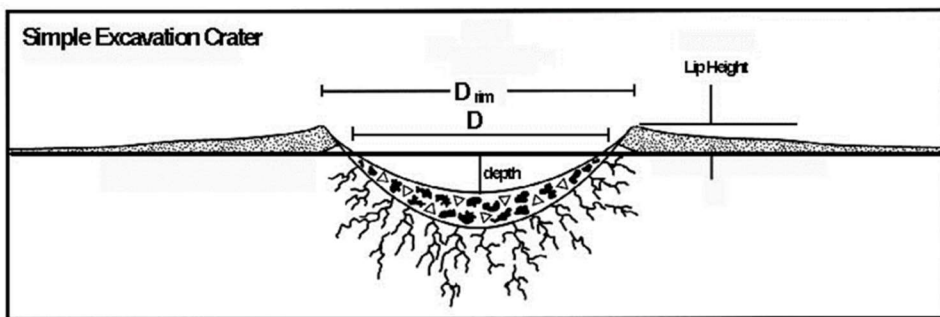


Figure 10.4-5. Dimensions of a simple crater

The crater volume is the volume of the void between the plane of the original surface and the profile of the apparent crater. The depth of the crater is maximum vertical distance between the plane of original surface and the profile of the crater as shown in Figure 10.4-5. The crater diameter D is the crater diameter at the original surface also as shown in Figure 10.4-5.

Holsapple's crater dimension scaling web site (ref. 7) lists the following relation between the apparent crater depth (called the excavation depth by Holsapple) and the crater volume V for a simple crater in lunar regolith

$$\text{depth} = 0.6 V^{1/3}$$

Restricted distribution to NESC and designated team members until approved by the NRB.

and the following relation for the crater diameter D

$$D = 1.1 V^{1/3}$$

Holsapple doesn't list the maximum depth from which the ejecta originates. However, Holsapple does say that the ejecta volume is approximately 80% of excavation (apparent) volume. If the volume from which the ejecta originates has the same shape as the excavation volume, then the maximum depth the ejecta originates from is only 7% smaller than the excavation depth. Therefore, we shall assume that the maximum depth from which the ejecta originates is the same as the excavation depth.

Holsapple's crater dimension scaling web site (ref. 7) lists the following parameters for lunar regolith

$$\begin{aligned} K_1 &= 0.14 \\ K_1 &= 0.75 \\ \rho &= 1500 \text{ kg/m}^3 \\ Y &= 1.0 \cdot 10^5 \text{ Pa} \\ \mu &= 0.4 \\ v &= 0.33 \end{aligned}$$

Finally, a comment about the assumption that all craters produced by sporadic meteoroids and NEOs are simple. This is true for sporadic meteoroids which we've defined as 10-g and smaller. However, it is not true for the upper end of the size range of NEOs considered here. The author used Holsapple's web calculator and obtained the following asteroid diameters at the transition from simple to complex craters for two impact speeds and two impact angles.

Table 10.4-1 NEO diameter at the transition from simple to complex craters

| Impact speed km/s | Asteroid diameter (m) | Impact angle (measured from surface normal) degrees |
|-------------------|-----------------------|---|
| 15 | 420 | 0 |
| 15 | 490 | 45 |
| 40 | 290 | 0 |
| 40 | 330 | 45 |

Thus, the author recommends that the cratering relations for simple craters should not be used for NEOs larger than 200-m.

10.4.4 Contribution to the ejecta flux from impacts excavating to depths larger than 10-m

Finally, we calculate the depth of penetration into the lunar regolith by sporadic meteoroids and by NEOs. The excavation depth is independent of the projectile density because Holsapple chose $v = 1/3$. Thus, the excavation depth by the maximum mass sporadic meteoroid (10-g) is solely a function of impact speed and impact angle. Figure 10.4-6 is a plot of the calculated excavation depths for meteoroids traveling at approximately the average speed (20-km/s) and meteoroids traveling at approximately the maximum speed (70-km/s).

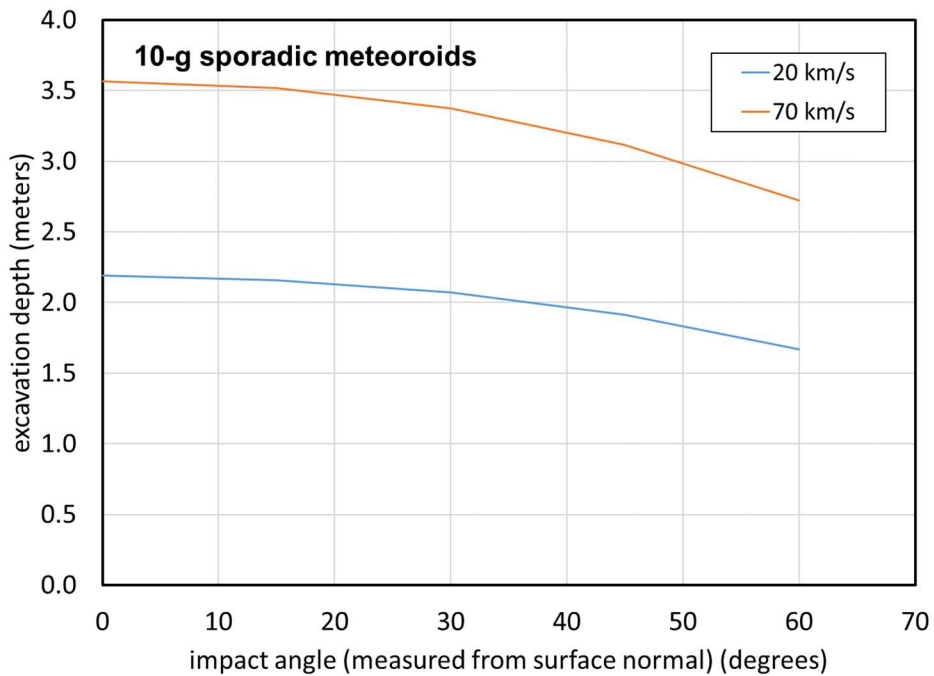


Figure 10.4-6. Excavation depth into the lunar regolith by sporadic meteoroids

The excavation depths are well within the regolith at both the maria and the highlands. Furthermore, the excavation depths are within the sampling depths from the Apollo lunar cores.

One may also use the crater dimension relations to estimate the mass of the NEO that will excavate the lunar regolith to the bottom of the regolith layer. Any NEO that excavates deeper than this is no longer cratering regolith, hence the ejecta scaling relations using regolith material parameters no longer apply. Figure 10.4-7 is a plot of the results for impact speeds near the average and maximum NEO impact speeds and for impact angles near the worst case and the average impact angle on a sphere.

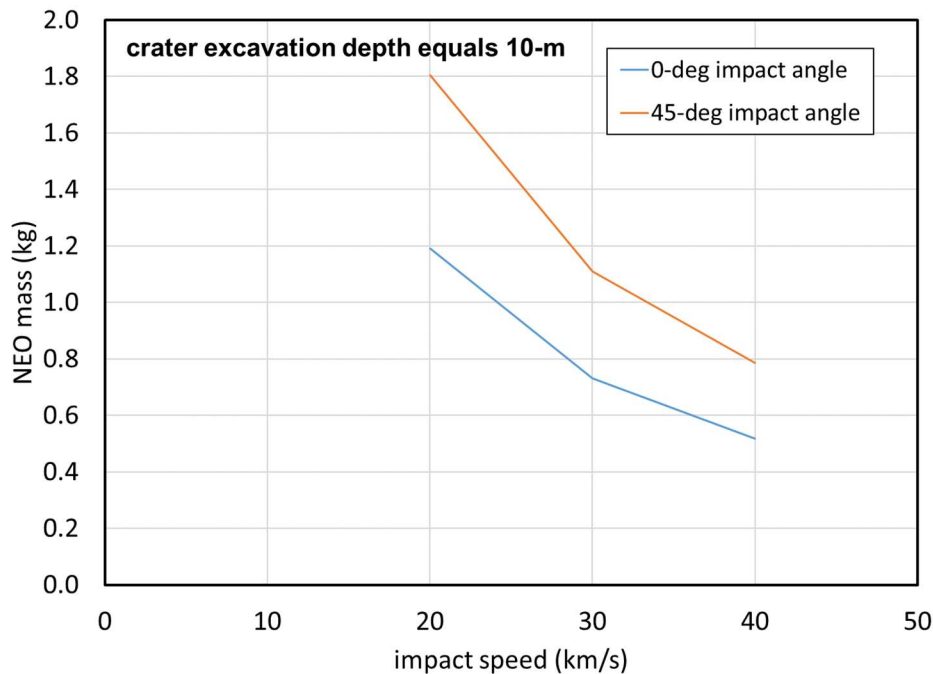


Figure 10.4-7 NEO mass that will excavate to the bottom of regolith 10-m thick resulting in an 37-m diameter crater.

The masses are in the range of 500-g to 1.8-kg (6.8-cm to 10.5-cm), nowhere near the maximum 1.57×10^{12} -kg for a 1-km diameter NEO considered by the NEO environment model. Thus, the NEOs in the range of 1-m to 1,000-m are cratering into bedrock material and different material parameters should be used in the ejecta mass scaling relation.

Finding 19: Ejecta mass scaling for impacts by NEOs 1 m to 1 km in diameter uses soil as the target material, but basalt is more appropriate because the impactor will push through the soil layer and contact the basalt layer below.

Recommendation 18: For large impactors (i.e., NEOs), change the target material characteristics from soil to basalt.

Figure 10.4-8 shows an example of a lunar bench crater, ref. 8, where the impactor has penetrated the regolith. The crater in the regolith is 140-m in diameter. In the center of the crater is a smaller crater in the basalt bedrock. The area between the two crater rims is the exposed basalt bedrock and is roughly flat, forming the bench mentioned in name of the crater morphology. Typically, these types of craters are searched for to estimate the regolith thickness. Note the large blocks surrounding the crater from the excavation of the basalt bedrock. These blocks are not described by the regolith soil size distribution. However, this crater must have had a large amount of ejecta from the regolith as well as ejecta from the bedrock. Not until the crater in the maria is substantially deeper than 10-m will the ejecta be mostly composed of basalt.

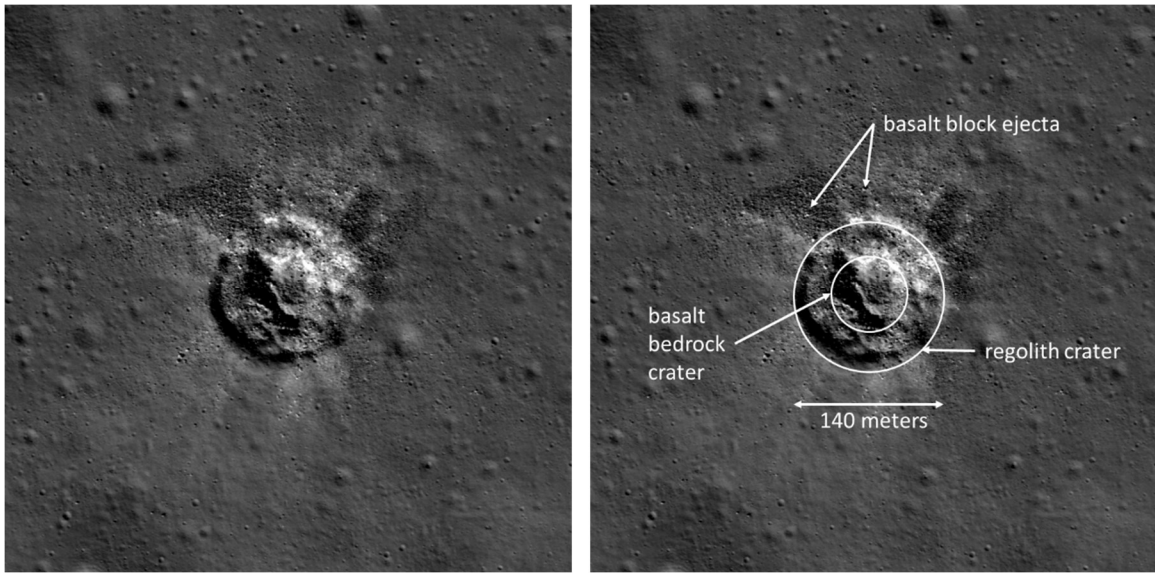


Figure 10.4-8 An example of a bench crater in lunar crater Plato. (ref. 7)

Figure 10.4-9 is a plot of the contribution of the NEO flux to the creation of the lunar ejecta flux. The ratio plotted along the y-axis is the ratio of the ejecta flux created by sporadic and NEO impacts with masses less than 1-kg (gray curve), or 100-kg (orange curve), 10^7 -kg (gold curve) or 10^{12} -kg (blue curve) but larger than 10^{-7} -kg to the ejecta flux created solely by the sporadic flux between 10^7 -kg to 10^{-7} -kg.

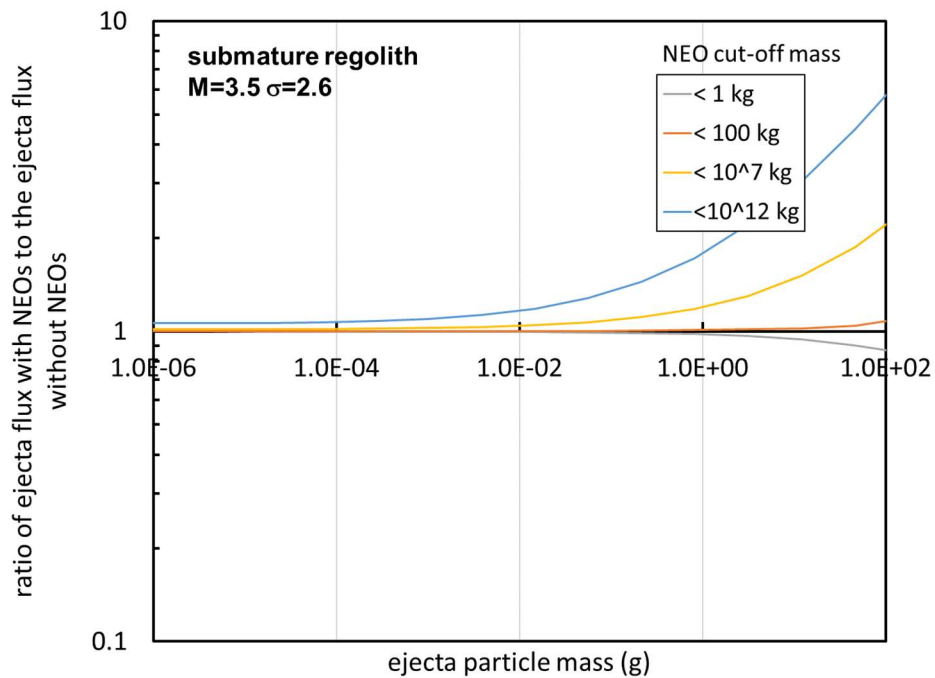


Figure 10.4-9 Contribution to the ejecta flux from impacts by sporadic and NEOs with masses less than 1-kg, less than 100-kg and less than 10^7 -kg.

The mass cut-off at 1-kg is around the mass of a sporadic or NEO that will excavate to 10-m depth. It is also close to the transition between the Grun flux curve for sporadics and the NEO

flux curve. The grey curve shows that about 15% of the flux of 100-g ejecta particles comes from sporadics larger than 1-kg when there is no contribution from NEOs.

The blue curve shows that the MeMoSeE procedure of including 1-km diameter asteroid impacts of Moon increases the ejecta flux of 100-g particles by a factor of about six (at least for the assumptions of this simplified analysis). This is a substantial addition to the ejecta flux based on questionable assumptions about the ejecta particle size distribution.

Furthermore, the mean time between occurrences of impacts of the Moon by 1-km asteroids is large. The author makes an estimate of the mean time using the results of the recent review by Ivanov (ref. 9) plotted in Figure 10.4-10. The probability per year of an NEO impact with the Earth is plotted along the y-axis and the diameter of the NEO is plotted along the x-axis.

The filled squares on point are the data used by Brown to calculate his NEO flux used in MeMoSeE, which range from diameters from 100-cm to 8-m. The red broken line is a curve with slope -2.7 (Brown's flux mass exponent cubed to convert to diameter). The probability of impact per year is about 3×10^{-7} per year or a mean time between occurrences of 3.33×10^6 years. Ivanov lists the impact rate on the Earth as 20 times larger than the impact rate on the Moon, hence the mean time between impacts of the Moon by 1-km diameter NEOs is 6.67×10^7 years.

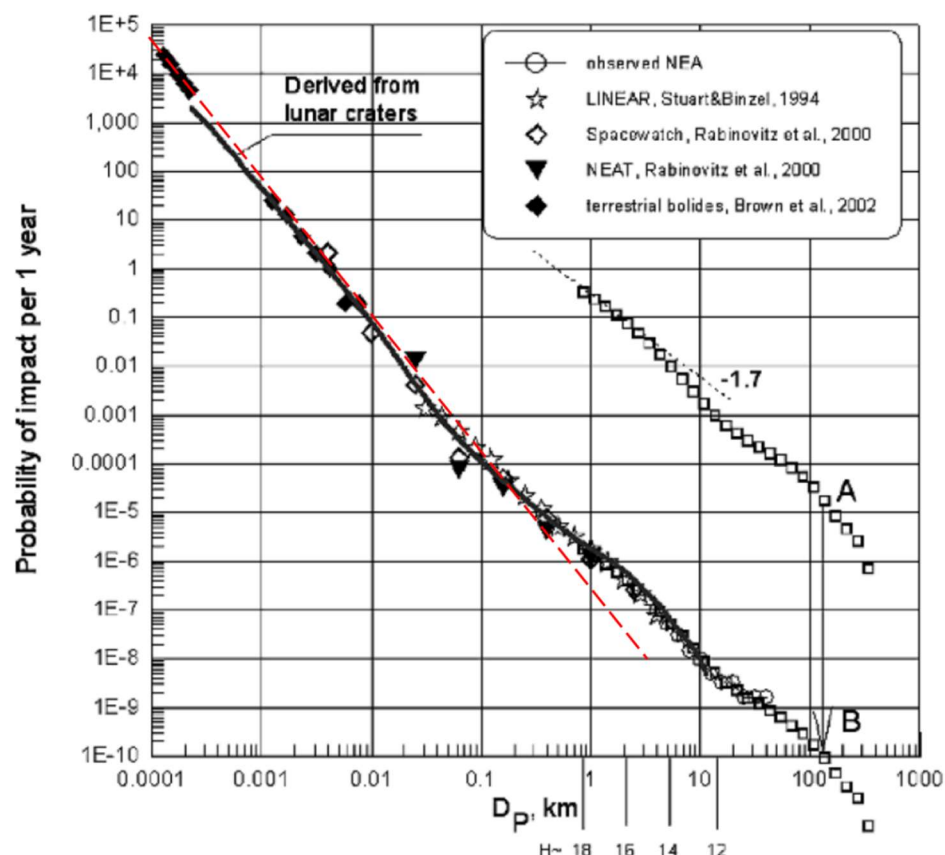


Figure 10.4-10 Ivanov's estimate of the probability of an NEO impact with the earth as a function of the diameter of the NEO. (ref. 9)

Ivanov's estimate of the probability of occurrence of an impact on the Moon by a one-km diameter NEO deviates from Brown's extrapolation. Ivanov estimates the mean time between occurrences as is once every ten million years, six times smaller, but still a large number.

Clearly, averaging this flux over sixty-six million years to obtain a yearly flux is wrong.

The open rectangles in Fig 10.4-10 is the distribution of asteroid diameters in the main belt expressed as a probability. Ivanov translated this curve from point A to point B and obtained good agreement with the NEO size distribution. Ivanov then concluded that the shape of the NEO probability curve at the largest diameters is due to the distribution of the asteroid sizes in the main belt that are perturbed into Earth crossing orbits, Thus the non-power nature of the curve is real and extrapolating from 10-cm to 1-km by a power-law is uncalled for.

10.5 Ejecta Impact Risk Versus Sporadic Meteoroid Impact Risk

The NESC created the Lunar Meteoroid Eject Model Review Team to respond to an HLS request to review and evaluate the MeMoSeE model's physical basis and assumptions, contributing data, verification-and-validation and model output. Engineers will ultimately use the MeMoSeE output to evaluate the risk of an HLS failure by lunar ejecta. Thus, this section uses the MeMoSeE output to calculate a spacecraft's risk of impact by lunar ejecta in order to preview what the HLS engineers can expect.

Section 10.5.1 presents results from Apollo and Constellation using the 1969 ejecta environment model. These results indicate that the lunar ejecta risk is 5% or less of the total sporadic meteoroid and lunar ejecta risk while on the lunar surface. Section 10.5.1 goes on to document reasons to think that the HLS risk of penetration by lunar ejecta risk calculated with MeMoSeE will be an even smaller fraction of the total meteoroid and ejecta risk than that calculated with the Apollo lunar ejecta environment model.

Section 10.5.2 should be preliminary HLS results, however, all three designs are currently competition sensitive and any estimates of ejecta impact risk are not publishable by the team. Therefore, the author used the Constellation Altair lunar lander as a surrogate. This subsection presents results for the previous sporadic meteoroid and ejecta models and the current sporadic meteoroid model with the MeMoSeE ejecta model. As expected, the MeMoSeE results are an even smaller fraction of the total sporadic meteoroid and ejecta risk than the previous models.

Finding 20: The relative HLS penetration risk from lunar ejecta compared to total penetration risk while on the lunar surface is dependent on spacecraft construction. The ratio of the lunar ejecta penetration risk to the total penetration risk can vary from less than a few percent up to half of the total risk while on the lunar surface.

Risk assessments generally develop two numbers, the probability of loss of crew and the probability of loss of mission. The analysis of Section 10.5 uses failure criteria appropriate to loss of crew.

Section 10.5.3 is some thoughts on the importance of lunar ejecta to the Artemis Base Camp mission.

Section 10.5.4 is a summary of the importance of lunar ejecta to the exploration extravehicular mobility unit (xEMU).

10.5.1 Overview of prior results and consequences for MeMoSeE

What follows is a discussion of the reasons for thinking the prior ejecta model specifies more flux than the MeMoSeE ejecta model. The first part is an overview of spacecraft MMOD impact-risk results from the prior ejecta model to establish a baseline for comparison with MeMoSeE. The second part is a discussion of the variability of the baseline results with the spacecraft construction and the relative separation of the ejecta and sporadic meteoroid flux equations. The third and final part combines the second part with the different assumed lunar surface geologies and the different ejecta mass scaling relations to predict how the MeMoSeE results will differ from the prior results.

MMOD analysts evaluated the risk of lunar ejecta impact risk for two prior spacecraft, the Apollo lunar module and the Constellation Altair. In each case, analysts used the Zook lunar ejecta environment (Zook 1967) as simplified for NASA SP-8013 (ref. 11). Eardley and Lang in ref. 12 calculated the Apollo Lunar Module impact risk for the Lunar Module's various components. Eardley and Lang found that ejecta accounted for 4% of the on-surface meteoroid/ejecta impact risk. However, for some components the ejecta was 15% to 50% of the total risk. Similarly, Bjorkman and Christiansen, ref. 13, found for the Constellation Altair lunar lander that ejecta accounted for 5.4% of the total on-surface meteoroid/ejecta impact risk. The single sheet components had ejecta risks ranging from 1.6% to 5.2% of the total component meteoroid/ejecta impact risk and components protected by a meteor bumper (ref. 14) had ejecta risks ranging from 12% to 37% of the total component meteoroid/ejecta impact risk. The reason for ejecta's small contribution to single sheet penetration risk is that ejecta twofold. First, the basalt ejecta travel so slowly that 5 to 10-mm diameter ejecta particles are required to perforate spacecraft components. Second, the flux of larger basalt ejecta particles is so much smaller than the flux of small meteoroids that perforate at a factor of 20 or more in impact speed, that the relative contribution to the risk is small. However, when a meteor bumper protects the component, the meteor bumper acts as a low pass filter and filters out most of the high-speed meteoroids leaving just a few meteoroid perforations roughly equal to the number of ejecta penetrations. Thus, protecting a component with a meteor bumper does not change the number of penetrations by ejecta, but does reduce the number penetrations by sporadic meteoroids to the point that ejecta penetrations become significant.

The result that ejecta may contribute 50% of the risk is specific to the Lunar Module and the NASA SP-8013 environment and may or may not apply to other spacecraft or other ejecta environments. Figure 10.5-1 illustrates the variability of the ejecta contribution to the total risk. Once computes the relative risk from Figure 10.5-1 with the assumption all NASA SP-8013 ejecta particles travel at the average speed of 0.1-km/s and all MEMR2 (ref. 15) sporadic meteoroids travel at the average speed of 22.3-km/s. Furthermore, one must assume all sporadic meteoroid trajectories are normal to the upwards facing flat sheet lying on the lunar surface. The graph on the left is a plot of the ballistic limit curve of a single sheet of aluminum 0.1791-cm thick (the red curve) and the ballistic limit curve of a meteor bumper and its rear wall (a geometry often referred to as a Whipple shield) with the same total thickness. A ballistic limit curve separates the space of impact-speed and projectile-diameter pairs that perforate the shield (those lying above the curve) from those pairs that are stopped by the shield (those lying below the curve). These particular curves apply to projectiles that impact at 90 degrees to a flat sheet

pointing upwards. The graph on the right is the cumulative flux of MEMR2 sporadic meteoroids (red curve) and NASA SP-8013 ejecta (green curve) with diameters larger than the value plotted on the x-axis. The target is a flat sheet lying on the lunar surface pointing upwards. One computes the penetrating flux by reading across the ballistic limit plot starting at the critical diameter that perforates at the impact speed and then reading down the cumulative flux plot to obtain the cumulative number of penetrations per square meter per year.

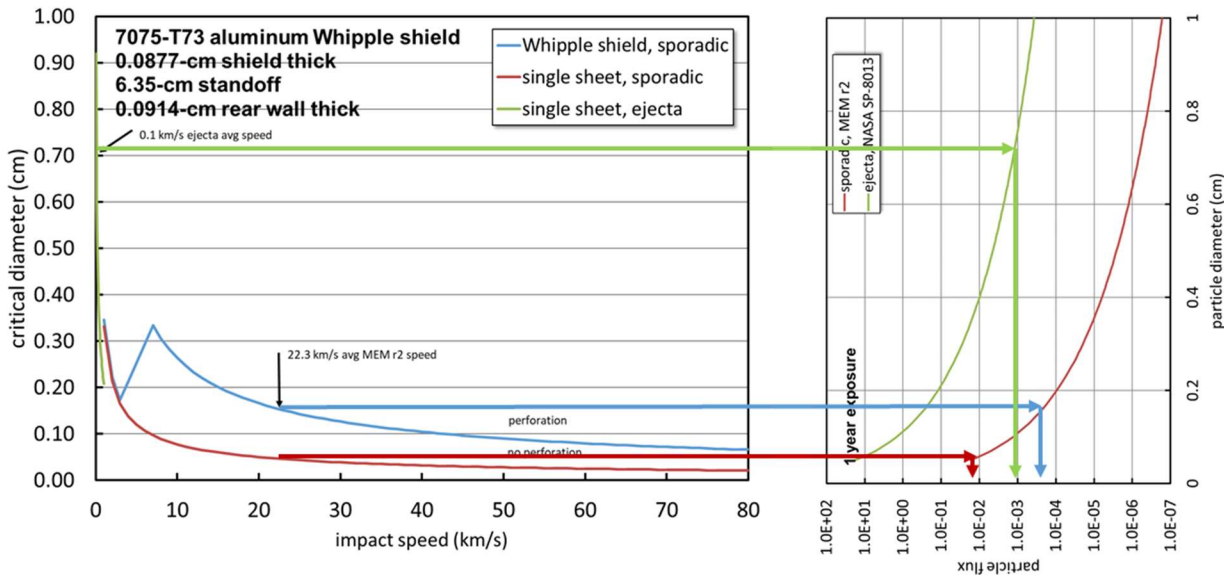


Figure 10.5-1. How to calculate the penetrating flux for single speed and single impact angle ejecta and sporadic meteoroid environments.

The set of green arrows give the ejecta penetration flux, the set of red arrows gives the sporadic single sheet penetration flux and the set of blue arrows gives the sporadic Whipple shield penetration flux. In this example, ejecta accounted for 80% of the total number of Whipple shield penetrations and sporadic meteoroids account for 90% of the total number of single sheet penetrations. The relative positions of the curves in Figure 10.5-1 illustrates two important points:

1. Ejecta will always be a small fraction of the total number of single sheet penetrations provided the ejecta flux is not vastly larger than the sporadic meteoroid flux (i.e., 3 orders of magnitude or more larger than the sporadic meteoroid flux).
2. Ejecta can be a small or large contribution to the total number of Whipple shield penetrations. If the Whipple shield is optimal, then ejecta will be nearly all of the penetrations. If the ejecta environment model is changed so that the ejecta flux is decreased to the point that the ejecta flux is near the sporadic meteoroid flux (or the sporadic meteoroid model changed so that the sporadic meteoroid flux is increased to values near the ejecta flux), then the sporadic meteoroids will be nearly all the penetrations.

Lastly, one should bear in mind that the Apollo and Constellation designs were for sortie missions with a single-use lunar lander. The Artemis program intends to develop reusable spacecraft and to establish the Artemis base camp at the lunar South Pole where the HLS could be exposed to the lunar ejecta environment for months. These two features of the Artemis

program will drive the HLS design towards using meteor bumpers. Thus, the Apollo LM and the Constellation Altair are a low side estimation of the importance of lunar ejecta impact risk to the HLS.

With the above as background, there are two conclusions as to how the MeMoSeE ejecta environment affects MMOD impact-risk assessment results. First, DeStafano based MeMoSeE on the scaling of the total mass ejected for a cratering flow governed by a coupling parameter. Figure 10.5-2 is a plot from ref. 5 of the Gault et al. (1963) results for impacts of basalt (the blue triangles, fitted with the black curve) which Zook and Cour-Palais used to develop the NASA SP-8013 ejecta model.

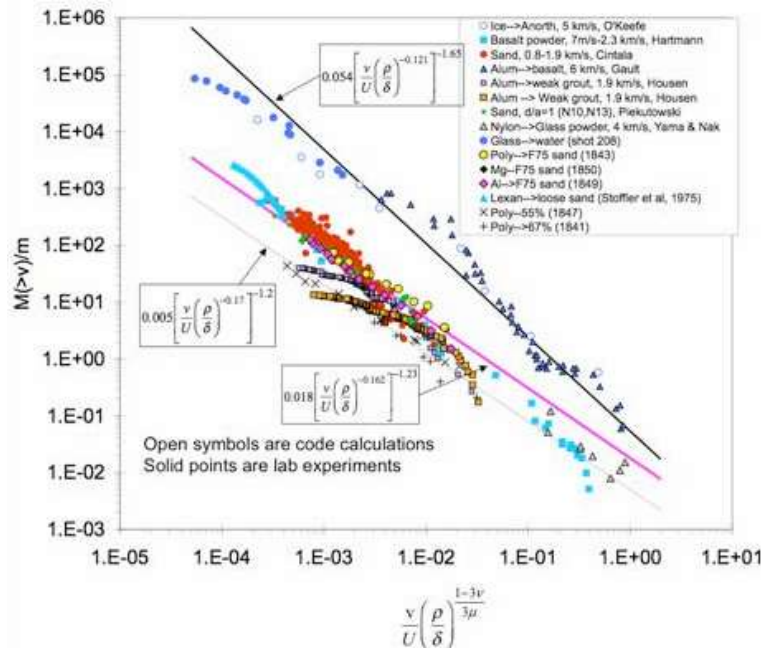


Figure 10.5-2. Scaled ejection mass versus ejection speed for various geological materials. (ref. 5)

The magenta curve fits the test data from the 1970's to the present for impacts of soils. Note that the excavated mass is significantly smaller for the craters in soil. Consequently, the MeMoSeE ejecta flux will be smaller than the NASA SP-8013 ejecta flux. Hence, the conclusion that less flux combined with smaller particles will result in less risk of penetration than the NASA SP-8013 ejecta environment. Second, because of Apollo, we now know that a fine soil layer to a depth of 5 to 10 meters in the lunar maria and a depth of 20 to 30 meters in the lunar highlands covers the lunar surface. The distribution of soil particle diameters is restricted to a small range with an average particle size of 80 to 100 microns. Thus, the maximum mass ejecta particle ever likely to strike a spacecraft is smaller than one would expect if the lunar surface were solid basalt. Thus we conclude that the MeMoSeE lunar ejecta environment requires larger impact speeds to penetrate spacecraft components than the larger particles from the NASA SP-8013 environment.

10.5.2 Application of MeMoSeE to the HLS Sortie Mission

Figure 10.5-3 is a plot to scale of the two spacecraft for which we have results using the NASA SP-8013 environment (LM and Altair) and the three HLS bidder's spacecraft for which we desire results using the MeMoSeE environment (HLS National Team, HLS Dynetics and HLS

Restricted distribution to NESC and designated team members until approved by the NRB.

SpaceX). However, the HLS contract is currently in competition, hence the designs are competition sensitive and not available for this report. Thus, this evaluation uses the Altair minimum requirements spacecraft and the Altair with the HVIT recommended shielding as a stand-in. In light of the discussion in Section 10.5.1, we expect the Altair single wall trends to generalize to the HLS spacecraft, however, the Whipple shield results do not because they are dependent on the shield standoff, which may or may not be similar to the HLS standoffs.

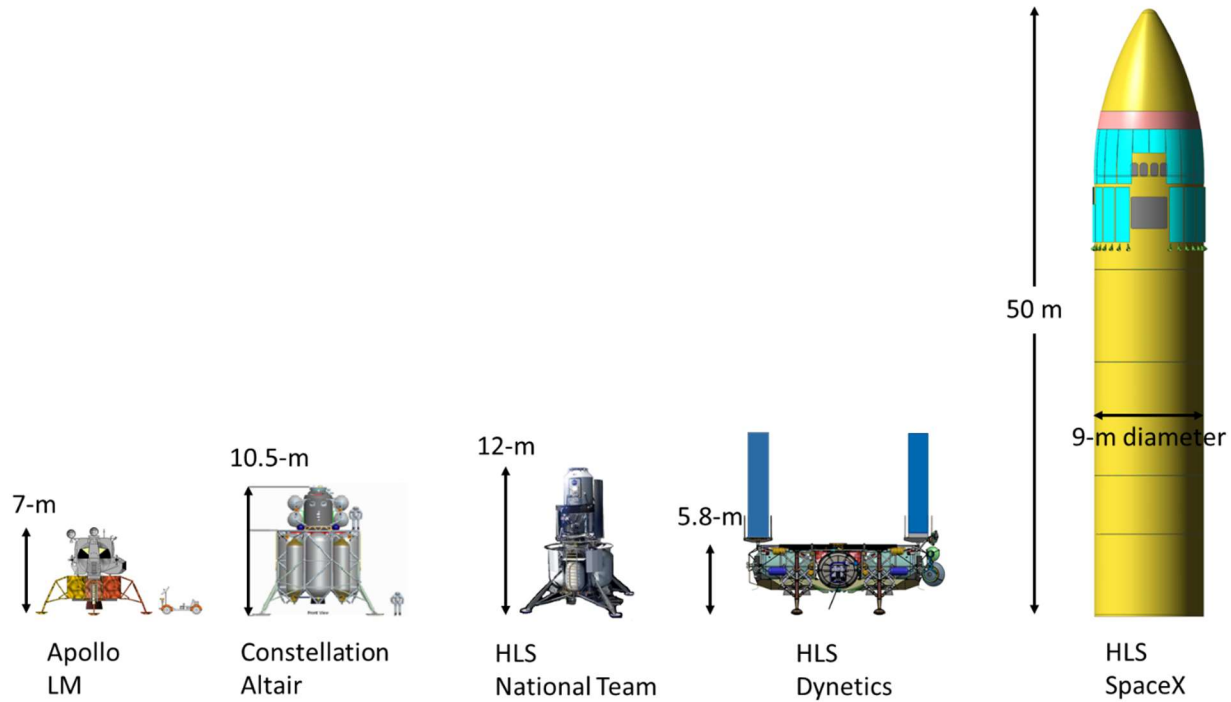


Figure 10.5-3. Apollo, Constellation and HLS Crewed Lunar Landers

The author assessed the Altair meteoroid and ejecta impact-risk using Bumper. NASA has used Bumper to evaluate spacecraft MMOD risk since 1987, ref. 17. In 2005, NESC performed an independent technical inspection of Bumper and concluded, “BUMPER II is the best tool currently available for Space Shuttle and ISS MMOD risk assessments”, ref. 18. A detailed description of the Bumper algorithm is not given here. Suffice it to say:

1. Bumper uses a triangular and rectangular surface-element geometry model of the spacecraft to keep track of the orientation of the various regions of the spacecraft relative to the meteoroid and ejecta trajectories impinging on the spacecraft.
2. Bumper uses ballistic limit equations (BLEs) to calculate the particle diameter required to damage the spacecraft component given the particle’s impact speed and impact angle.
3. Bumper uses the surface element model to calculate the portions of the spacecraft shadowed from the particle trajectory by other portions of the spacecraft.

Figure 10.5-4 is a render of the Altair surface element model created for the 2010 MMOD impact risk assessment. The model includes the Altair ascent module and tanks the descent module tanks, but does not include the landing gear. The landing gear are robust structure resistant to meteoroid and eject impact and they do not shadow significant portions of the

Restricted distribution to NESC and designated team members until approved by the NRB.

spacecraft when it is on the lunar surface. Therefore, this analysis excludes the landing gear to speed up the calculations.

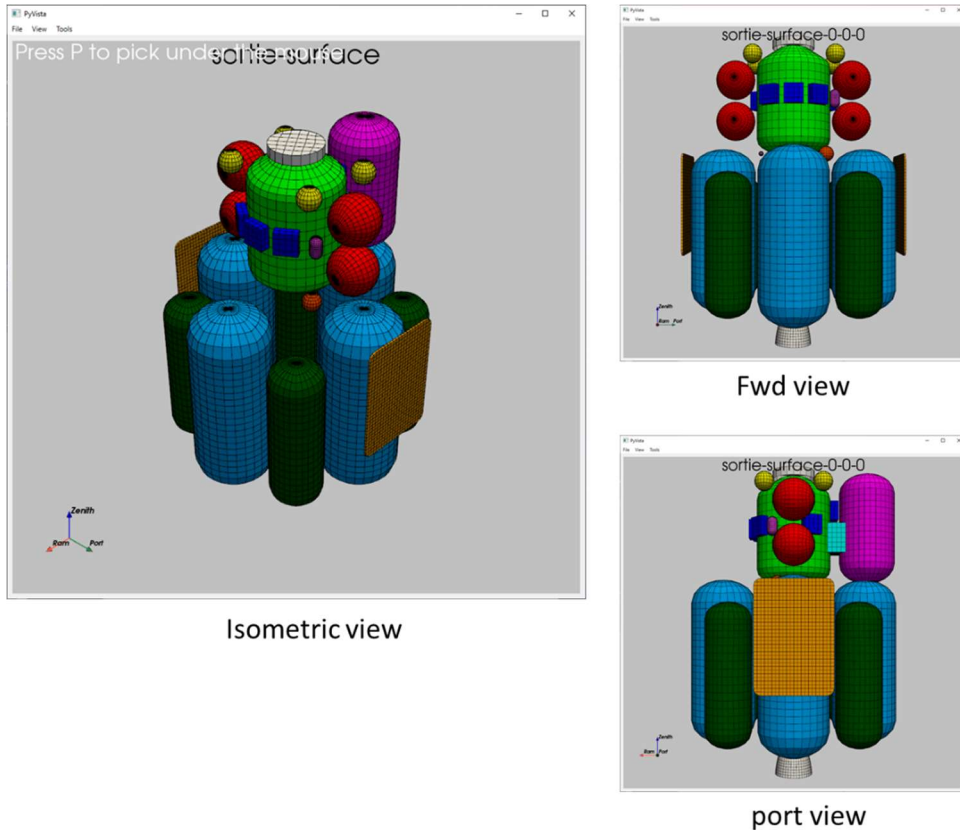


Figure 10.5-4. Altair surface element model constructed for the Bumper MMOD impact risk assessment.

The left hand side of Figure 10.5-5 is a render of the ascent module including labels of the various components assessed. The right hand side of Figure 10.5-5 is a schematic diagram of the component wall thicknesses and materials. Note that the crew cabin is the only double wall construction (i.e., Whipple shield). All the other components are single wall construction. The crew module wall is a one-inch thick aluminum honeycomb with composite face sheets. The short one-inch standoff will reduce the effectiveness of the honeycomb as a Whipple shield.

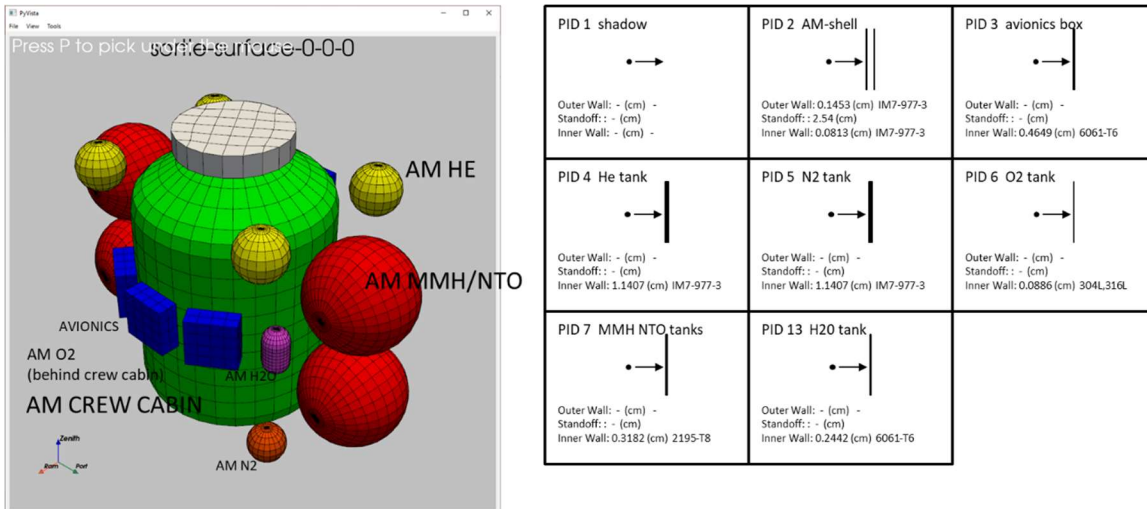


Figure 10.5-5. Altair ascent module wall construction.

Figure 10.5-6 is a similar plot for the descent module. The descent module render is on the left and wall construction of the descent module is on the right.

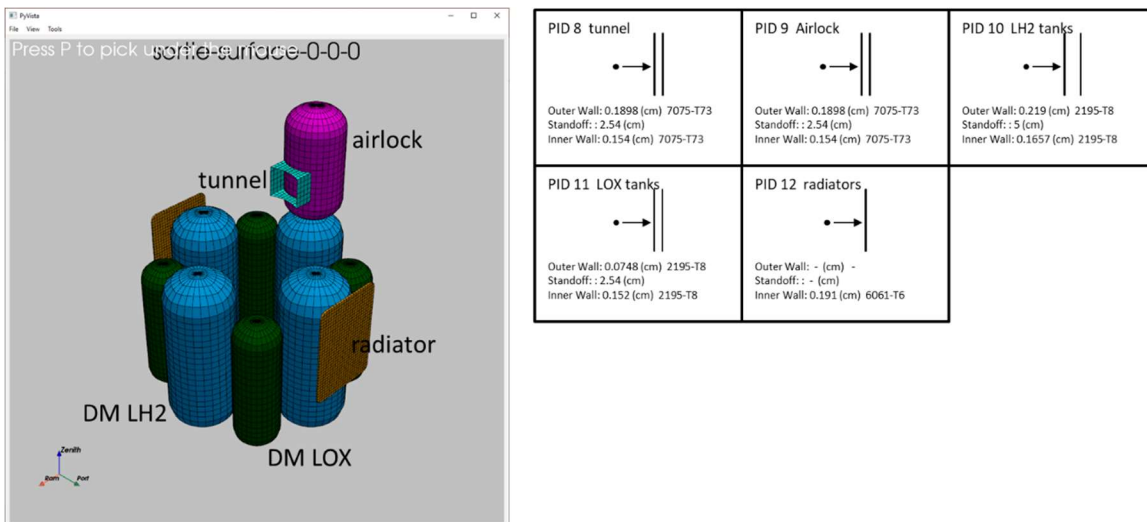


Figure 10.5-6. Altair descent module wall construction.

The descent module tanks all use honeycomb materials for the tank walls. The only single wall component in the descent module are the radiators.

The assessments that follow all use the same HLS sortie mission lunar stay. The lunar stay starts on November 14, 2024 and runs for 5.8 days. The Altair lander is located at the lunar south pole at the HLS design reference mission (DRM) site 01, ref. 19. The Altair lander is oriented so that the Altair X-axis is pointing east. (The axis labeled “ram” in the render is the Altair X-axis.)

Figure 10.5-7 is a render of the number of penetrations per square meter per year contouring the Altair geometry model. The sporadic and ejecta contours are on two different scales. Because the number of ejecta penetrations is so much smaller than the number of sporadic meteoroid penetrations if the two renders used the same color map the color scale would crush ejecta contours into the dark blue.

Restricted distribution to NESC and designated team members until approved by the NRB.

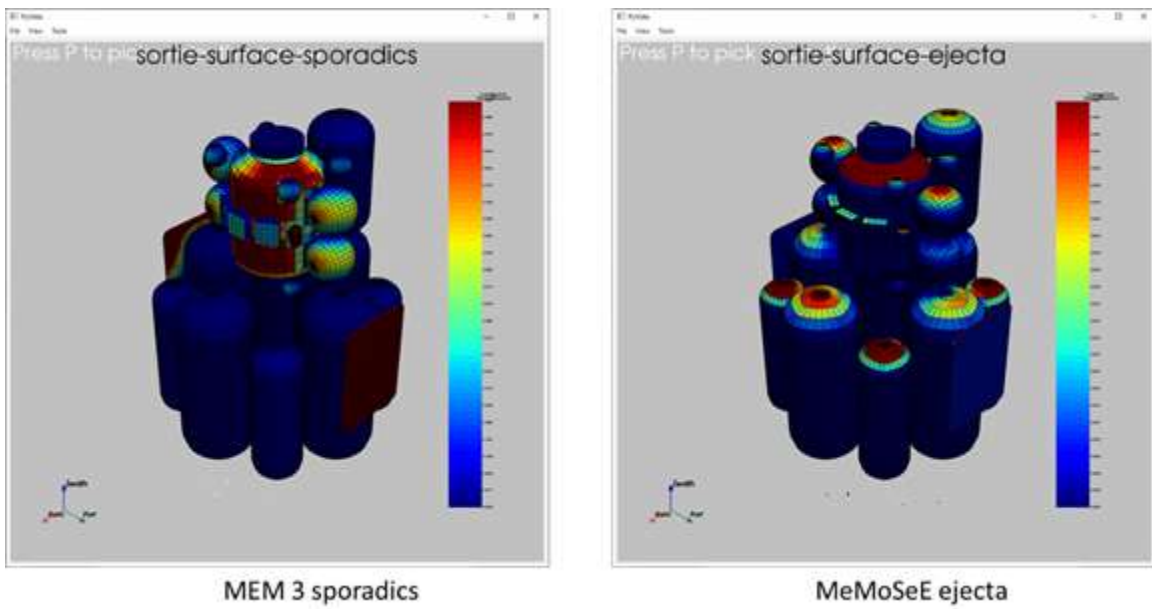


Figure 10.5-7. Penetrations per square meter per year by sporadic meteoroids and lunar ejecta.

Figure 10.5-7 shows that the majority of the MEM 3, ref. 20, penetrating sporadic meteoroids come from one direction along the horizon and that the MeMoSeE penetrating ejecta come from above. If one averaged the sporadic meteoroid flux over 19-years, then the penetrations spread uniformly around the circumference of the crew cabin. Another feature of Figure 10.5-6 is that the descent module Whipple shield protected tanks have less risk of penetration per unit area by sporadic meteoroids than the single wall construction crew cabin and ascent module tanks, as expected.

While not shown in Figure 10.5-7, the location of the peak number of penetrations makes one complete rotation around the circumference of the crew cabin during the lunar month. Thus, the number of penetrations of the crew cabin varies with the landing date because of the shadowing provided by the air lock and tanks.

Figure 10.5-8 is a histogram comparing the relative number of penetrations by sporadic meteoroids and lunar ejecta for the same mission but two different sets of environments. The histogram on the left uses the MEM r2 sporadic meteoroid environment and the NASA SP-8013 ejecta environment. The histogram on the right uses the MEM 3 sporadic meteoroid environment and the MeMoSeE lunar ejecta environment.

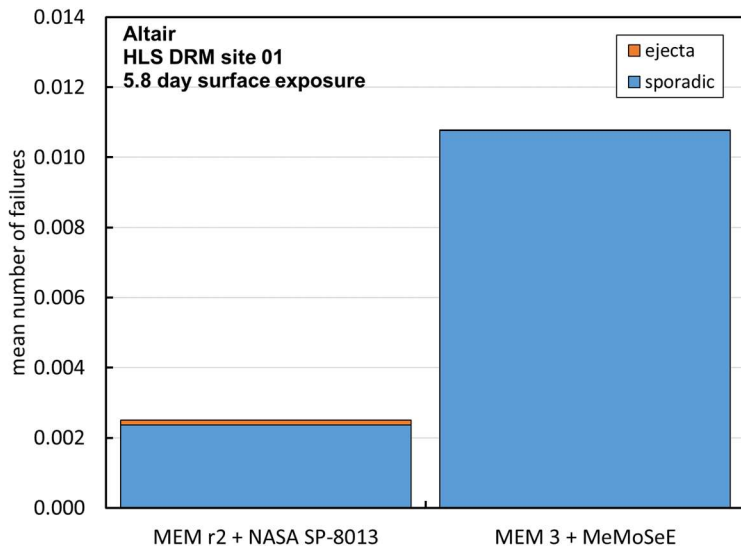


Figure 10.5-8. Total number of failures due to ejecta and sporadic meteoroid impacts calculated with the two environment sets.

The blue fractions of the Figure 10.5-8 histogram are the number of failures due to sporadic meteoroids during 5.8 days of exposure of the Altair minimum functionality vehicle. The orange fractions are the mean number of failures due to ejecta impacts. The NASA SP-8013 ejecta model number of penetrations is a small fraction of the MEM r2 sporadic meteoroid model number. However, as anticipated, the MeMoSeE ejecta number of penetrations is even smaller. The relative contribution to the total number of failures is smaller still due to the much larger number of penetrations by MEM 3 sporadic meteoroids. While the MEM 3 flux is smaller than MEM r2, the mass densities are a factor of 3.5 larger and the impact speeds are also somewhat larger, leading to more penetrations.

The histograms in Figures 10.5-9 and 10.5-10 illustrate the effect of adding the HVIT recommended Whipple shields to two Altair components. Figure 10.5-9 shows the changes in the results from adding Whipple shields to the ascent module shell and the ascent module MMH/NTO tanks when evaluated using the MEM r2 sporadic meteoroid environment and the NASA SP-8013 lunar ejecta environment. Figure 10.5-10 shows the changes from adding Whipple shields when evaluated with the MEM 3 ejecta environment and the MeMoSeE lunar ejecta environment.

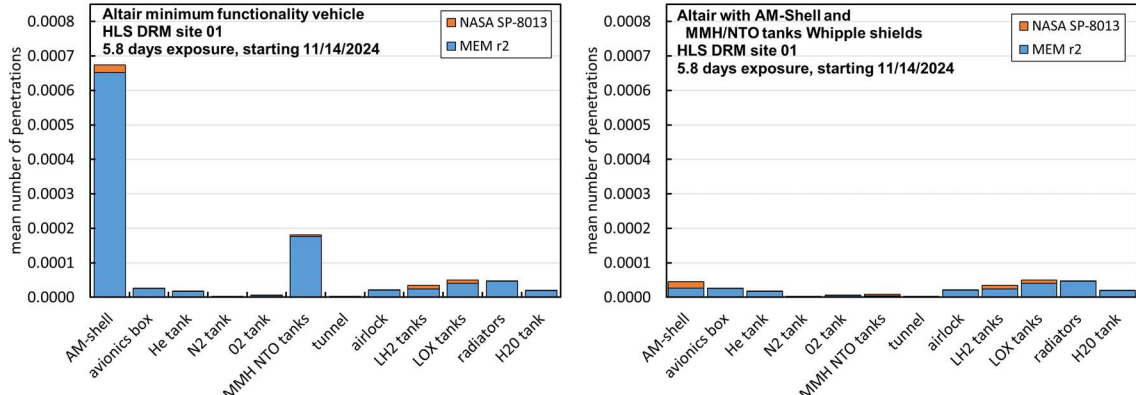


Figure 10.5-9. Number of failures by component, with and without Whipple shields, evaluated with the NASA SP-8013 lunar ejecta environment and the MEM r2 sporadic meteoroid environment

The Figure 10.5-9 histogram on the left shows the component mean number of failures for sporadic meteoroids (blue) and for ejecta (orange). The ascent model shell and the propellant tanks mean number of failures is decreased significantly by the Whipple shield, but only the number of failures by sporadic meteoroids was decreased, not the number of failures by lunar ejecta. This resulted in roughly equal numbers of failures by sporadic meteoroids and lunar ejecta for the two Whipple shield protected components.

Figure 10.5-10 contains plots similar to Figure 10.5-9, only for the MEM 3 sporadic meteoroid number failures and for the MeMoSeE lunar ejecta number of failures. The number of failures by lunar ejecta are so small in this plot they are barely visible.

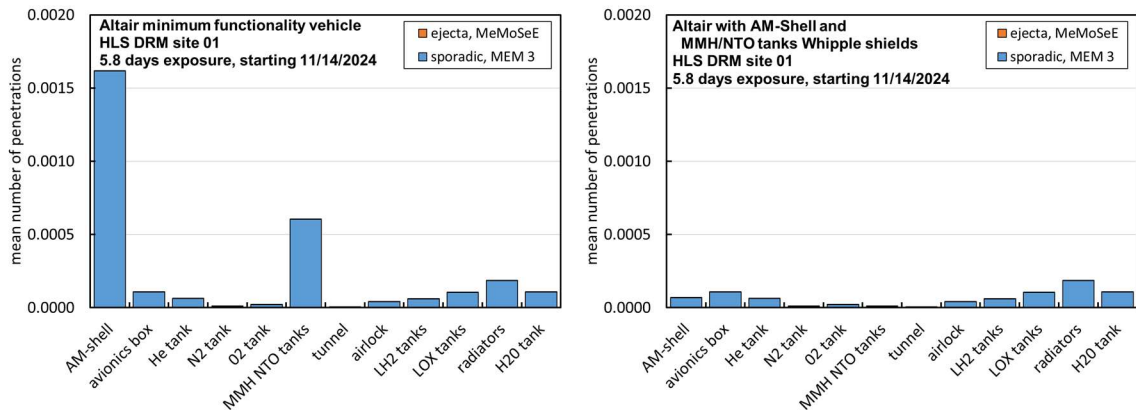


Figure 10.5-10. Number of failures by component, with and without Whipple shields, evaluated with the MeMoSeE lunar ejecta environment and the MEM 3 sporadic meteoroid environment

Table 10.5-1 lists the sum of the above results for reference.

Table 10.5-1 Summary of results with and without shields for two sets of environments.

| | | |
|--|---|---|
| Altair lunar lander configuration assessed | NASA SP-8013 lunar ejecta number of failures as a fraction of the total MEM r2 sporadic meteoroid and lunar ejecta number of failures | MeMoSeE lunar ejecta number of failures as a fraction of the total MEM 3 sporadic meteoroid and lunar ejecta number of failures |
|--|---|---|

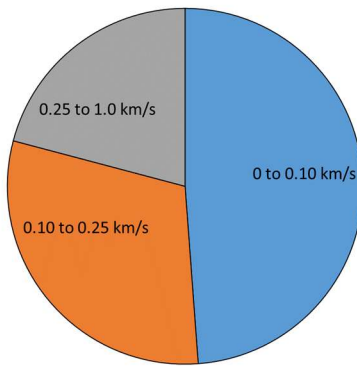
Restricted distribution to NESC and designated team members until approved by the NRB.

| | | |
|-------------------------------|-------|-------|
| Minimum functionality vehicle | 4.8% | 0.04% |
| With HVIT recommended shields | 17.5% | 0.14% |

Note that the MeMoSeE contribution to the Altair total ejecta and meteoroid impact risk is two orders of magnitude smaller than the NASA SP-8013 contribution to the risk. This is a combination of the larger MEM 3 sporadic meteoroid impact risk and the smaller MeMoSeE lunar ejecta impact risk.

The second anticipated feature of the MeMoSeE lunar ejecta environment (the first being the smaller number of penetrations of single wall components) was because the regolith particles are smaller than basalt crater ejecta particles the typical penetration would require a larger impact speed. The author modified Bumper to output the number of penetrations per environment speed bin. Figure 10.5-11 plots the results.

NASA SP-8013 Relative Number of Penetrations by Impact Speed Bin



MeMoSeE Relative Number of Penetrations by Impact Speed Bin

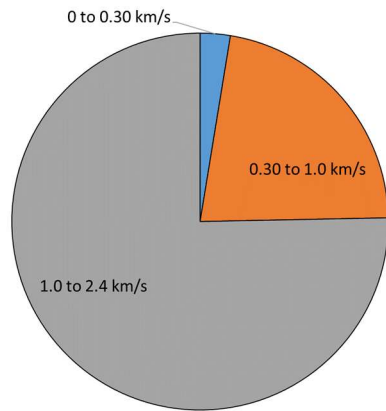


Figure 10.5-11. Relative number of penetrations per speed bin for the two ejecta environments.

NASA SP-8013 results in half of the penetrations occurring for speeds between 0 to 0.1 km/s and essentially none of the penetrations occurring for speeds larger than 1 km/s. However, MeMoSeE results in three quarters of the penetrations occurring for speeds between 1 to 2.4- km/s.

Restricted distribution to NESC and designated team members until approved by the NRB.

10.5.3 The Lunar Ejecta Penetration Risk and the HLS at the Artemis Base Camp

If the HLS makes longer stays on the lunar surface, then more meteoroid shielding is required. If the HLS design uses more Whipple shields to decrease the sporadic meteoroid penetration risk, then the lunar ejecta penetration risk becomes more important. Hence, the authors anticipate that the lunar ejecta environment is important to HLS designs for the Artemis Base Camp mission.

10.5.4 The xEMU Lunar Ejecta Penetration Risk

Though not discussed here, preliminary studies indicate that the Exploration Extravehicular Mobility Unit (xEMU) risk of penetration by lunar ejecta is nearly equal to the sporadic meteoroid penetration risk (using the Apollo lunar ejecta environment model). This is due to the limited effectiveness of the thermal-meteoroid garment as a Whipple shield due to the small thickness of the garment.

10.6 Number of MeMoSeE Speed Bins Required for Converged Calculations of Mean Number of Failures

The calculated number of spacecraft penetrations varies with the number of MeMoSeE impact speed bins. Currently, MeMoSeE uses three logarithmically spaced speed bins. The question arises whether three speed bins provide a converged answer, and if not, then is the non-converged answer an over-estimate of the risk or an under-estimate of the risk? If three bins are an overestimate of the risk and the increased risk is acceptable to the HLS program, then MeMoSeE is suitable for spacecraft design. If three bins are an underestimate of the risk, either then MeMoSeE needs more speed bins or the MeMoSeE developers need to create a factor that designers can apply to the MeMoSeE results to arrive at a conservative design.

Finding 21: The use of only three ejecta velocity bins overestimates penetration risk by a factor of 1.4. Three bins are conservative and adequate for an engineering model.

Finding 22: Ascending ejecta particles from nearby primary impacts can have speeds greater than escape velocity. This will contribute to the overall MMOD risk for the assessed asset.

Recommendation 19: Include high-velocity (i.e., \geq escape velocity) particle flux in the DSNE tables if ascending ejecta are added to the model.

A preliminary analysis of the time required to do a convergence study with MeMoSeE indicated that it was prohibitive. A MeMoSeE run takes 72 hours. If results with 2, 4, 6, ... 50 bins are desired then a total of 650 MeMoSeE runs are needed. Running 20 serial jobs on a workstation at a time results in a total wall clock time of 98 days.

Therefore, the authored opted to use the Zook ejecta environment to make the convergence study. (One may not use the NASA SP-8013 environment because it is a three speed-bin model developed from a fit to the published three bins output from the Zook model. However, one can use the Zook model to calculate the fluxes corresponding to any number of speed bins, which the author has done here.)

The author coded up the Zook model in MathCAD with the modification of using the coupling parameter relation for cumulative ejecta mass launched with speed v or larger. Figure 10.6-1 is a comparison of the Zook model (blue curve) ejecta mass relation and the coupling parameter relation (orange curve).

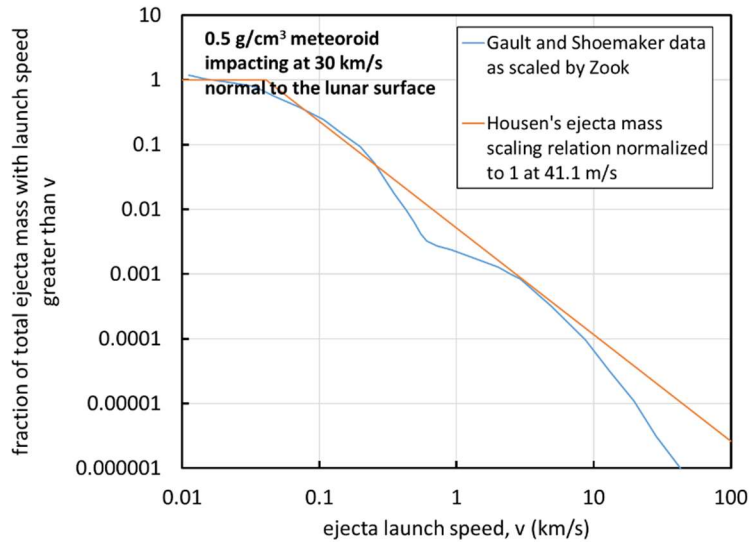


Figure 10.6-1. The Zook function $G(v)$ scaled to the sporadic meteoroid impact conditions assumed by Zook in his model compared with the function used in the author's MathCAD analysis.

The Zook model does not use the coupling parameter relation precisely. The coupling parameter relation uses cumulative ejecta mass $M(>v)$ normalized by meteoroid mass m , while the Zook model uses the cumulative ejecta mass $M(>v)$ normalized the excavated crater mass ρV (where ρ is the regolith density and V is the apparent crater volume). The Zook model ejecta mass relation and excavated crater mass relation do not use a consistent coupling parameter, so the author treated the excavated crater mass as a free parameter and adjusted the coefficient of the orange curve in Figure 11 until the author obtained good agreement with published Zook ejecta flux curves.

Figure 10.6-2 compares the published Zook flux curves (the solid lines) with the flux curves calculated by the author with his MathCAD implementation of the Zook model. The agreement while not exact, because of the different cumulative ejecta mass relations used, is acceptable.

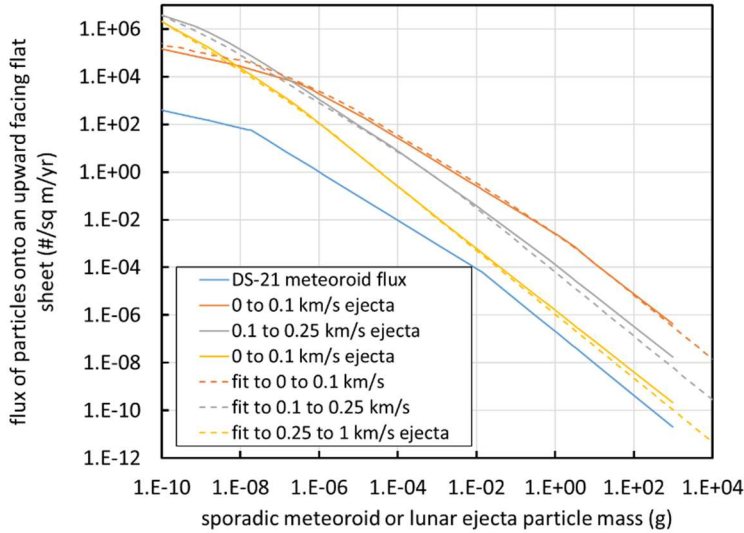


Figure 10.6-2. Comparison of published Zook ejecta flux curves and the author's MathCAD implementation of the Zook model.

With the ejecta flux equations in hand, the author then calculated the number of penetrations μ during exposure time Δt of a single sheet of 6061-T6 aluminum, 0.040-inches thick and surface area A , lying on the lunar surface pointing up. Though not specified in the Zook model, the author assumed a 45-degrees ejecta launch angle and hence a 45-degrees impact angle.

We start by first considering the mean number of impacts by particles with mass m for the i^{th} speed bin with speeds between v_i and v_{i+1} :

$$\mu_i = A\Delta t\{F(m, v_i) - F(m, v_{i+1})\}$$

where F is the Zook ejecta model flux and m is the ejecta particle mass.

Now the desired mean number of perforations is approximately the mean number of impacts of mass m filtered by the ballistic limit equation for critical diameter $d_c = B(v, \vartheta)$, where $m = \rho \pi/6 d_c^3$ and ρ is the mass density of the ejecta particles (about 3.1-g/cm³).

The ballistic limit thickness equation for a single sheet of aluminum is:

For $\rho_p/\rho_t < 1.5$

$$t = 9.43d_c^{19/18}BHN^{-0.25}\left(\frac{\rho_p}{\rho_t}\right)^{0.5}\left(\frac{V \cos \vartheta}{C_t}\right)^{2/3}$$

For $\rho_p/\rho_t \geq 1.5$

$$t = 9.43d_c^{19/18}BHN^{-0.25}\left(\frac{\rho_p}{\rho_t}\right)^{2/3}\left(\frac{V \cos \vartheta}{C_t}\right)^{2/3}$$

where

| | |
|-------------|--|
| BHN | = Brinell hardness number |
| C_t | = speed of sound in the target (km/s) |
| d_c | = critical projectile diameter (cm) |
| t | = target thickness (cm) |
| ρ_p | = projectile density (g/cm ³) |
| ρ_t | = target density (g/cm ³) |
| ϑ | = impact angle measured from target normal |
| V | = impact speed (km/s) |

This can be solved for the ballistic limit equation $d_c = B(v, \vartheta)$.

Therefore, the mean number of perforations is approximately

$$\mu_i = A\Delta t\{F(m_i, v_i) - F(m_i, v_{i+1})\}$$

$$m_i = \rho \frac{\pi}{6} \left[B \left(v_{avg,i}, \frac{\pi}{4} \right) \right]^3$$

Where m_i is the typical perforating ejecta mass for the speed bin computed with a weighted average impact speed. In what follows, linearly spaced speed bins are used with an average impact speed of

$$v_{avg,i} = \frac{v_i + v_{i+1}}{2}$$

And logarithmically spaced speed bins with a log average impact speed of

$$v_{avg,i} = 10^{\frac{\log v_i + \log v_{i+1}}{2}}$$

Figure 10.6-3 is a plot of the two sets of results. The x-axis is the number of speed bins used between 0.01-km/s and 1 km/s. The y-axis is the ratio or the result for $1 \leq n \leq 50$ bins divided by the result for 50 bins, the fully converged answer. The red curve is the plot of the linearly spaced speed bins results and the broken blue curve is the plot of the logarithmically spaced speed bins results.

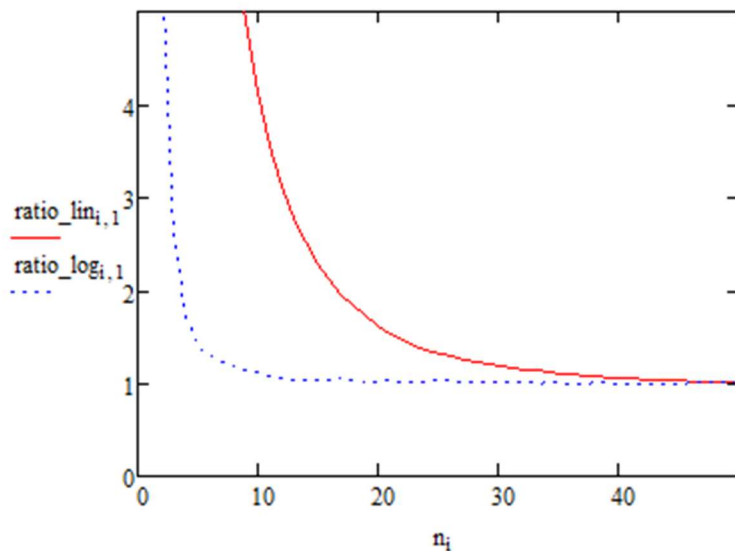


Figure 10.6-3. Ratio of convergence (μ_n/μ_{50}) as a function of speed bin spacing and number of speed bins

We conclude from Figure 10.6-3

1. MeMoSeE uses logarithmically spaced speed bins, thus the Bumper number of penetrations calculations will converge faster than if MeMoSeE used linearly spaced speed bins
2. MeMoSeE uses three speed bins and the three speed bin results are a factor of 1.43 overestimate of the penetration risk, hence the Bumper penetration risk estimates using MeMoSeE will lead to conservative spacecraft designs.

Table 10.6-1 lists the number of bins required for better than a factor of 1.43 convergence.

Table 10.6-1. Ratio of convergence as a function of speed bin spacing and number of speed bins

| Ratio of convergence, μ_n/μ_{50} | Number of linearly spaced speed bins | Number of logarithmically spaced speed bins |
|---|---|--|
| 1.10 | 36 | 8 |
| 1.05 | 42 | 11 |
| 1.01 | 48 | 39 |

11.0 Findings, Observations, and NESC Recommendations

[Note that this heading can be changed according to the assessment requirements (e.g., Findings and NESC Recommendations or Findings and Observations, or Observations and Findings).

Note that not all Findings or Observations require an NESC Recommendation, but if there are NESC Recommendations, then they must map back to one or more Findings and/or Observations.]

11.1 Findings

The following findings were identified by the assessment team during the course of this study:

Restricted distribution to NESC and designated team members until approved by the NRB.

Finding 1: The DSNE tables do provide the information necessary for Bumper MMOD risk assessments.

Finding 2: The NEO flux appears to be implemented incorrectly in the model. A meteoroid flux that is partially shielded by the Moon is rescaled using a NEO flux that contains no such shielding.

Finding 3: The model's assumed angles of incidence of NEO impactors with respect to the Moon's surface resembles the MEM high density population. However, these directions should more closely resemble the low-density meteoroid population in MEM than the high-density population.

Finding 4: The model adequately accounts for the LADEE ejecta particle size distribution measurements.

Finding 5: The magnitude of ejecta yield in the model reasonably matches LADEE data.

Finding 6: The model ejecta angular distribution does not reproduce LADEE measurements.

Finding 7: The shape of the model's ejecta speed distribution differs from the exponential distribution determined from LADEE observations.

Finding 8: The model focuses on particles ejected during the excavation phase of the impact process and does not account for jetted material expelled away from the impact site at low angles to the target's surface and high velocities during the contact/compression phase.

Finding 9: The resurfacing rate (~80,000 years) caused by secondary impacts modeled with MeMoSeE agrees with statistics derived from temporal observations collected by the LROC NAC.

Finding 10: While the derived resurfacing rate is consistent with LROC measurements of secondary surface changes, the stochastic clustering of distal ejecta is not considered in the current model. LROC temporal image pairs (before/after observations) reveal secondary surface disturbances that are significantly larger (1 to 30 m in diameter) than the secondary impacts modeled in MeMoSeE (<0.01 m). These observed secondary features are likely the result of the clustering of many secondary particles that impact the surface.

Finding 11: Monte Carlo results have been used to test the flux algorithms used in MeMoSeE.

Finding 12: The flux of ascending ejecta (i.e., striking the asset "from below") generated by primary impacts close to the asset can be of a similar order of magnitude as the flux of descending ejecta (i.e., striking the asset "from above") due to impacts farther away. However, the ascending population is not currently included in the model.

The detailed effect of this ascending component of the flux on an asset is dependent on the detailed shape of that asset.

Finding 13: The stochastic nature of the location of the primary impact flux, combined with the strong dependence of the flux on distance from the asset, mean that for any finite length of time, the actual number of secondaries impacting an asset may vary by several orders of magnitude from the mean value – much more than from standard Poisson sampling error. This stochastic nature of the flux appears to be the main driver in the uncertainty of the flux for any mission.

Finding 14: The ejecta flux can be non-uniform over different geographical regions of the Moon and at different times. Temporal variations are typically factors of 2 and variations with latitude/longitude are typically factors of 5, but closer to factors of 2 when averaged over local time. However, these variations are still small compared to stochastic variations.

Finding 15: By including NEO sizes that rarely impact the Moon, the model may be overconservative in computing the quantity of ejecta produced by these objects in a typical year.

Finding 16: Assuming the mass of the largest particle ejected by an impact cannot exceed the total ejected mass predicted by the Housen and Holsapple (2011) equations, then the model may produce estimates of the hazardous ejecta flux that are a factor of 3-4 too high.

Finding 17: The model uses a soil size distribution characteristic of a single submature soil.

Finding 18: Using the observed regolith particle size distribution instead of the average value used by the model results in an increase in ejecta flux by a factor of 1.6 to 4 for the sizes of most interest to the HLS design.

Finding 19: Ejecta mass scaling for impacts by NEOs 1 m to 1 km in diameter uses soil as the target material, but basalt is more appropriate because the impactor will push through the soil layer and contact the basalt layer below.

Finding 20: The relative HLS penetration risk from lunar ejecta compared to total penetration risk while on the lunar surface is dependent on spacecraft construction. The ratio of the lunar ejecta penetration risk to the total penetration risk can vary from less than a few percent up to half of the total risk while on the lunar surface.

Finding 21: The use of only three ejecta velocity bins overestimates penetration risk by a factor of 1.4. Three bins are conservative and adequate for an engineering model.

Finding 22: Ascending ejecta particles from nearby primary impacts can have speeds greater than escape velocity. This will contribute to the overall MMOD risk for the assessed asset.

11.2 Observations

Observation 1: The radius of the Moon used in MeMoSeE is 1737.1 km instead of the traditional 1737.4 km. The 1737.1 km value is also used by the model when calculating the escape velocity.

Observation 2: The model name "Meteoroid Model of Secondary Ejecta" does not accurately and unambiguously describe the environment modeled and the acronym (MeMoSeE, pronounced "mimosa") is difficult to type and unclear how to pronounce.

Observation 3: Both the model acronym and documentation use the term “secondary ejecta.” This term can be ambiguous, as it can be confused with other phenomena on the Moon.

Observation 4: With some code modifications, the model could help assess the distribution of secondaries around impact sites, particularly the distal ejecta identified in LROC images around newly formed impacts.

11.3 NESC Recommendations

Recommendation 1: Use the canonical value of 1737.4 km for the geometrically averaged lunar radius. [see Observation 1]

Recommendation 2: Consider changing the model name and acronym to those that emphasize accuracy and ease of use. For example, "Lunar Ejecta Engineering Model (LEEM)" would be clear, accurate, and simple to type and pronounce. [see Observations 2 and 3]

Recommendation 3: Use the terms “secondaries,” “secondary environment,” or “ejecta” in place of “secondary ejecta.” [see Observation 3]

Recommendation 4: The meteoroid-to-NEO flux scaling should be conducted using the meteoroid flux on a flat plate facing away from the lunar surface and the NEO flux on the lunar surface per unit surface area. [see Finding 2]

Recommendation 5: Consider replacing the NEO angular distribution with that of the low-density MEM population. [see Finding 3]

Recommendation 6: Incorporate LADEE ejecta angular distributions into the model. If the resulting assessed risks are significantly different, permanently incorporate the LADEE ejecta angular distributions into the model. [see Finding 6]

Recommendation 7: Incorporate LADEE ejecta speed distributions into the model. If the resulting assessed risks are significantly different, permanently incorporate the LADEE ejecta speed distributions into the model. [see Finding 7]

Recommendation 8: Incorporate jetted material expelled during the impact contact/compression phase into future versions of the model. [see Finding 8]

Recommendation 9: Consider modifying the model to account for the clustering of secondary particles impacting the surface. This should not affect the average flux of secondary particles, however the risk to a surface asset may increase if impacted by multiple, closer packed particles. [see Finding 10]

Recommendation 10: Use the Monte Carlo flux calculation results provided to verify model flux calculations. [see Finding 11]

Recommendation 11: Include in future versions of the model effects of ascending ejecta from primary impacts that occur very close to the asset. [see Finding 12]

Recommendation 12: Consider modifying the model to use Monte Carlo methods in addition to or in lieu of analytic methods to compute flux for future versions of the mode. This will allow the ability to compute the stochastic variability of the flux. [see Finding 13]

Recommendation 13: The model output should have a way of calculating and reporting the stochastic variability of the flux. This might be shown by identifying the mean, median, and extreme cases (such as a 95% confidence level for maximum flux). The corresponding DSNE tables will need some breakdowns in probability for use in PRA analyses. [see Finding 13]

Recommendation 14: Reconsider choosing what is the “average” location on the Moon vs choosing several example locations for the DSNE (e.g., at different longitudes or use 7-day intervals rather than average 19 years). The DSNE tables should include both nominal and worse-case scenarios. [see Finding 14]

Recommendation 15: Limit the maximum size of primary impactors that are computed to contribute to ejecta in the model. One practical way to limit maximum projectile size is to identify the size of impactor that has a 1% chance of hitting the Moon during a nominal mission time. For a 10-year lunar base mission, this corresponds to a mean time between impacts of 1000 years. Alternatively, a Monte Carlo analysis with the full range of possible sizes

might capture this effect without artificially limiting impactor size. [See Finding 15]

Recommendation 16: Consider placing an upper limit on the ejected particle size that is determined using conservation of energy and/or the ejecta mass. [see Finding 16]

Recommendation 17: Perform a sensitivity study varying the soil size distribution parameters over the range of measured soil size distributions of the Apollo soil samples. [see Findings 17 and 18]

Recommendation 18: For large impactors (i.e., NEOs), change the target material characteristics from soil to basalt. [see Finding 19]

Recommendation 19: Include high-velocity (i.e., \geq escape velocity) particle flux in the DSNE tables if ascending ejecta are added to the model. [see Findings 12 and 22]

12.0 Alternative Viewpoint(s)

There were no alternative viewpoints identified during the course of this assessment by the NESC team or the NRB quorum.

13.0 Other Deliverables

No unique hardware, software, or data packages, outside those contained in this report, were disseminated to other parties outside this assessment.

14.0 Lessons Learned

No lessons learned were identified by this assessment.

15.0 Recommendations for NASA Standards and Specifications

No recommendations for NASA standards and/or specifications were identified as a result of this assessment.

16.0 Definition of Terms

Finding A relevant factual conclusion and/or issue that is within the assessment scope and that the team has rigorously based on data from their independent analyses, tests, inspections, and/or reviews of technical documentation.

Observation A noteworthy fact, issue, and/or risk, which may not be directly within the assessment scope, but could generate a separate issue or concern if not addressed. Alternatively, an observation can be a positive acknowledgement of a Center/Program/Project/Organization's operational structure, tools, and/or support provided.

Restricted distribution to NESC and designated team members until approved by the NRB.

| | |
|----------------|---|
| Problem | The subject of the independent technical assessment. |
| Recommendation | A proposed measurable stakeholder action directly supported by specific Finding(s) and/or Observation(s) that will correct or mitigate an identified issue or risk. |

17.0 Acronyms and Nomenclature

| | |
|---------|--|
| ALaMO | Automated Lunar and Meteor Observatory |
| AM | Ascent Module |
| ARC | Ames Research Center |
| AU, au | astronomical unit |
| BLE | ballistic limit equation |
| CNEOS | Center for Near Earth Object Studies |
| DHRZ | Distal High Reflectance Zone |
| DLRZ | Distal Low Reflectance Zone |
| DM | Descent Module |
| DRM | design reference mission |
| DSNE | Design Specification for Natural Environments |
| ESD | Exploration Systems Development |
| GSFC | Goddard Space Flight Center |
| He | gaseous helium |
| HLS | Human Landing System |
| HVIT | Hypervelocity and Impact Technology group |
| H2O | water |
| JSC | Johnson Space Center |
| LADEE | Lunar Atmosphere Dust and Environment Explorer |
| LaRC | Langley Research Center |
| LDEX | Lunar Dust Experiment |
| LDEF | Long Duration Exposure Facility |
| LRO | Lunar Reconnaissance Orbiter |
| LM | Apollo Lunar Module |
| LH2 | liquid hydrogen |
| LOX | liquid oxygen |
| LROC | Lunar Reconnaissance Orbiter Camera |
| MEM | Meteoroid Engineering Model |
| MeMoSeE | Meteoroid Model of Secondary Ejecta |
| MMH/NTO | monomethylhydrazine and nitrogen tetroxide |
| MMOD | micrometeoroid and orbital debris |
| MSC | Manned Spacecraft Center |
| MSFC | Marshall Space Flight Center |
| NAC | Narrow Angle Camera |
| NEA | near Earth asteroid |
| NEO | near Earth object |
| NESC | NASA Engineering and Safety Center |
| N2 | gaseous nitrogen |
| ORDEM | Orbital Debris Engineering Model |
| O2 | gaseous oxygen |

Restricted distribution to NESC and designated team members until approved by the NRB.

| | |
|------|--|
| PHRZ | Proximal High Reflectance Zone |
| PLRZ | Proximal Low Reflectance Zone |
| SME | subject matter expert |
| WAC | Wide Angle Camera |
| xEMU | Exploration Extravehicular Mobility Unit |

18.0 References

- Bernardoni, Szalay, and Horanyi, 2019. Impact Ejecta Plumes at the Moon. *Geophysical Research Letters*, 46(2), 534–543. <https://doi.org/10.1029/2018GL079994>
- Blaauw, 2017. The mass index and mass of the Geminid meteoroid stream as determined with radar, optical and lunar impact data. *Planetary and Space Science*, 143, 83-88. <https://doi.org/10.1016/j.pss.2017.04.007>
- Borovička et al., 2010. Material properties of transition objects 3200 Phaethon and 2003 EH1. In: Icy Bodies of the Solar System, 218-222. <https://doi.org/10.1017/S174392131000178X>
- Brown et al., 2002. The flux of small near-Earth objects colliding with the Earth. *Nature*, 420:6913, 294-296. <https://doi.org/10.1038/nature01238>
- Carrier, 2003. Particle Size Distribution of Lunar Soil. *Journal of Geotechnical and Geoenvironmental Engineering*, 129:10, 956-959. [https://doi.org/10.1061/\(ASCE\)1090-0241\(2003\)129:10\(956\)](https://doi.org/10.1061/(ASCE)1090-0241(2003)129:10(956))
- DeStefano, 2020a. Lunar Meteoroid Ejecta Model. Internal presentation.
- DeStefano, 2020b. Lunar Impact Ejecta Benchmark and Models. Internal report.
- DeStefano, 2020c. Untitled document (proposed changes to the Design Specification for Natural Environments).
- Gault, Shoemaker and Moore, 1963. Spray Ejected from the Lunar Surface by Meteoroid Impact. NASA TN D-1767.
- Grün et al., 1985. Collisional balance of the meteoritic complex. *Icarus*, 62:2, 244-272. [https://doi.org/10.1016/0019-1035\(85\)90121-6](https://doi.org/10.1016/0019-1035(85)90121-6)
- Holsapple, 1993. The scaling of impact processes in planetary sciences. *Annual Reviews of Earth and Planetary Sciences*, 21, 333-373. <https://doi.org/10.1146/annurev.ea.21.050193.002001>
- Horanyi et al., 2015. A permanent, asymmetric dust cloud around the Moon. *Nature*, 522(7), 324-326. <http://doi.org/10.1038/nature14479>
- Housen and Holsapple, 2011. Ejecta from impact craters. *Icarus*, 211:1, 856-875. <https://doi.org/10.1016/j.icarus.2010.09.017>
- Krüger et al., 2003. Impact-generated dust clouds surrounding the Galilean moons. *Icarus*, 164(1), 170-187. [http://doi.org/10.1016/S0019-1035\(03\)00127-1](http://doi.org/10.1016/S0019-1035(03)00127-1)
- Melosh, H.J., 1989. Impact Cratering: A Geologic Process. Oxford University Press. ISBN: 978-0195104639
- Moorhead, 2020a. NASA Meteoroid Engineering Model (MEM) Version 3. NASA/TM—2020-220555.

- Moorhead, 2020b. Internal memo: OSMA/MEO/Lunar-001.
- Moorhead et al., 2017. A two-population sporadic meteoroid bulk density distribution and its implications for environment models. *Monthly Notices of the Royal Astronomical Society*, 472(4), 3833-3841. <https://doi.org/10.1093/mnras/stx2175>
- Moorhead et al., 2019. Meteor shower forecasting in near-Earth space. *Journal of Spacecraft and Rockets*, 56:5, 1531-1545. <https://doi.org/10.2514/1.A34416>
- Moorhead et al., 2020. NASA's Meteoroid Engineering Model 3 and its ability to replicate spacecraft impact rates. *Journal of Spacecraft and Rockets*, 57:1, 160-176. <https://doi.org/10.2514/1.A34561>
- Pokorný et al., 2019. Meteoroids at the Moon: Orbital Properties, Surface Vaporization, and Impact Ejecta Production. *Journal of Geophysical Research: Planets*, 124(3), 752-778. <http://doi.org/10.1029/2018JE005912>
- Roberts, B., 2019. Cross-Program Design Specification for Natural Environments (DSNE): Revision G. SLS-SPEC-159.
- Robinson et al., 2015. New crater on the Moon and a swarm of secondaries. *Icarus* 252, 229-235. <https://doi.org/10.1016/j.icarus.2015.01.019>
- Speyerer et al., 2016. Quantifying crater production and regolith overturn on the Moon with temporal imaging. *Nature* 538, 215–218. <https://doi.org/10.1038/nature19829>
- Suggs et al., 2014. The flux of kilogram-sized meteoroids from lunar impact monitoring. *Icarus*, 238, 23-36. <https://doi.org/10.1016/j.icarus.2014.04.032>
- Szalay and Horanyi, 2016. Lunar meteoritic gardening rate derived from in situ LADEE/LDEX measurements. *Geophysical Research Letters*, 43(1), 4893–4898. <http://doi.org/10.1002/2016GL069148>
- Szalay et al., 2018. Activity of the 2013 Geminid meteoroid stream at the Moon. *Monthly Notices of the Royal Astronomical Society*, 474:3, 4225-4231. <https://doi.org/10.1093/mnras/stx3007>
- Szalay et al., 2018. Dust Phenomena Relating to Airless Bodies. *Space Science Reviews*, 214(5), 1-47. <http://doi.org/10.1007/s11214-018-0527-0>
- Szalay et al., 2019. Impact Ejecta and Gardening in the Lunar Polar Regions. *Journal of Geophysical Research: Planets*, 124(1), 143–154. <http://doi.org/10.1029/2018JE005756>
- Vickery, 1993. The theory of jetting: application to the origin of tektites. *Icarus*, 105, 441-453. <https://doi.org/10.1006/icar.1993.1140>
- Whipple, 1947. Meteorites and Space Travel. *The Astronomical Journal*, 52, 131.
- Zook, 1967. The Problem of Secondary Ejecta Near the Lunar Surface. In: Transactions of the 1967 National Symposium on Saturn V/Apollo and Beyond, volume I, pages EN–8. American Astronautical Society.

1. Lunar Source Book. edited by Grant H. Heiken, David T. Vaniman, Bevan M. French, Cambridge University Press, 1991. The Lunar Source Book is also available at https://www.lpi.usra.edu/publications/books/lunar_sourcebook/, accessed on May 15, 2021.
2. Wikipedia. Grain Size. https://en.wikipedia.org/wiki/Grain_size, accessed on May 15, 2021.
3. McKay D. S., Fruland R. M., and Heiken G. H. (1974) Grain size and evolution of lunar soils. Proc. Lunar Sci. Conf. 5th, pp. 887–906.
4. (Carrier 2003)
5. K. A. Holsapple, K. R. Housen. Gravity or Strength? An Interpretation of the Deep Impact Experiment. paper no. 1068. Lunar and Planetary Science XXXVII (2006).
6. (Holsapple 1993)
7. K. A. Holsapple. Impact and Explosion Effects. <http://keith.aa.washington.edu/craterdata/scaling/index.htm>. accessed on May 15, 2021.
8. Bench Crater in Plato. <http://lroc.sese.asu.edu/posts/446>
9. Ivanov B. (2008) Size-Frequency Distribution Of Asteroids And Impact Craters: Estimates Of Impact Rate. In: Adushkin V., Nemchinov I. (eds) Catastrophic Events Caused by Cosmic Objects. Springer, Dordrecht. https://doi.org/10.1007/978-1-4020-6452-4_2
10. (Zook 1967)
11. Cour-Palais, B.G. Meteoroid Environment Model – 1969 [Near Earth to Lunar Surface]. National Aeronautics and Space Administration. Washington DC. Report NASA SP-8013. March 1969.
12. Eardley, C.J. and E.A. Lang. Lunar Module Analysis for Meteoroid Hazard, TIR 580-S-8034, General Electric Apollo Support Department, 2-Feb-68.
13. Bjorkman, M.D., and E.L. Christiansen. Altair LDAC-2 MM Impact Risk Assessment. National Aeronautics and Space Administration, Johnson Space Center. Houston, TX. Report JSC-65834. November 19, 2010.
14. (Whipple 1947)
15. Moorhead, A.V., H.M. Koehler and W.J. Cooke. NASA Meteoroid Engineering Model Release 2.0. National Aeronautics and Space Administration. Marshall Space Flight Center, Huntsville, AL. Report NASA/TM-2015-218214. October 1, 2015.
16. (Gault et al. 1963)
17. Coronado, A.R., M.N. Gibbins, M.A. Wright and P.H. Stern. Space Station Integrated Wall Design and Penetration Damage Control: Users Guide for Design Analysis Code BUMPER. National Aeronautics and Space Administration. Marshall Space Flight Center, Huntsville, AL. Report NASA CR-179169 and NTIS number N88-10070. July 1987.
18. Scott, S. Independent Technical Inspection of the BUMPER-II Micrometeoroid and Orbital Debris risk Assessment Tool. NASA Engineering and Safety Center. Report RP-05-66. April 8, 2005.
19. Presentation charts from Scott Craig (MSFC/EV42), Greg Price (Jacobs) and Laura Burke (GRC). HLS Design Reference Mission. Undated, but circa 9/21/2020.

Restricted distribution to NESC and designated team members until approved by the NRB.

20. Moorhead, A.V. Meteoroid Engineering Model (MEM) 3: NASA's Newest Meteoroid Model. First International Orbital Debris Conference. Sugarland, TX. Paper no. 6054. December 9, 2019.

Restricted distribution to NESC and designated team members until approved by the NRB.